NTNU

Norwegian University of
Science and Technology

Nanostructured PDMS surfaces with patterned wettability

Thor Christian Hobæk

Nanotechnology
Submission date: June 2011
Supervisor: Pawel Tadeusz Sikorski, IFY
Co-supervisor: Florian Mumm, IFY

Norwegian University of Science and Technology
Department of Physics

Declaration of independent work

I hereby declare that the work presented in this thesis has been performed independently and in accordance with the exam regulations of the Norwegian University of Science and Technology (NTNU).

Thor Christian Hobæk
Trondheim, 15 June 2011

Abstract

In this study, a surface with patterned wettability by means of surface structuring, rather than through modifying the surface chemistry, was developed. The device presented in this thesis was inspired by the Namib Desert Bettle, which collects water from the fog by having hydrophilic spots surrounded by hydrophobic wax-coated regions on its back. Besides water collection, controlling the wetting behaviour locally on the surface may find applications within droplet-based microfluidics, or fabrication of DNA, protein or cell microarrays.

Spatial wetting contrast was achieved through replica moulding of the elastomer polydimethylsiloxane (PDMS), using a copper and/or the epoxy-based SU-8 photoresist surface as a template. Different types of surface roughness was produced and characterized on polycrystalline copper, through etching, oxidation, electrodeposition, or a combination. Regions with no surface roughness was patterned on the template moulds through conventional UV-photolithography processing of SU-8. The PDMS replicas were then tested for the ability to capture water droplets selectively on the patterned spots.

Through characterization of the surface roughness by atomic force microscopy (AFM) and scanning electron microscopy (SEM), copper plates etched with a solution of $CuCl_2$ and HCl produced the highest amount of surface roughness, with longer etching times leading to increased surface roughness. To characterize the hydrophobicity, the contact angle was measured for droplets deposited on the rough PDMS surfaces. Through surface structuring, the contact angle was increased from $101.8 \pm 3.6°$ for a flat surface, to $154.7 \pm 5.3°$ for the PDMS surface with the highest roughness. The polarity of surface roughness was also found to play an important role in the wetting behaviour, with a higher number of peaks than valleys being preferable.

The fabricated PDMS surfaces showed spatial wetting contrast, as demonstrated in the cover photo. The device needs further optimization in terms of increasing the hydrophobicity of the rough regions, as well as changing the pattern geometries. However, the discoveries made in this study may be useful for further development and integration with droplet-moving mechanisms, for future lab-on-a-chip applications within medical diagnostics or chemical analysis.

Preface

This thesis is submitted as the final work required for the Master's degree (MSc) in Nanotechnology at the Norwegian University of Science and Technology (NTNU). The work has been carried out at the Department of Physics, at the Faculty of Natural Sciences and Technology, with Associate Professor Pawel Sikorski as main supervisor and Post-doctoral fellow Florian Mumm as co-supervisor.

The study was performed from January to June 2011. The topic is inspired by the work done during the Nanotechnology Specialization Project (TMM4550, 15 ECTS), supervised by Professor Christian Thaulow at the Department of Engineering Design and Materials, which was a broad literature study of functional surfaces found in Nature and their biomimetic potential. The work has largely been performed in the new cleanroom facilities of NTNU Nanolab.

I would like to take the opportunity to thank the people who have helped me during this last semester. First of all, thanks to Associate Professor Pawel Sikorski for being a devoted, helpful and motivating supervisor. Secondly, I want to thank Post-doctoral fellow and co-supervisor Florian Mumm, who has been of great help during the experimental work. Without his creative ideas and our fruitful discussions, I would not have come as far I did.

Also, thanks to my fellow master students Kai Beckwith and Sigmund Størset and Post-doctoral fellow David Barriet, with whom I have collaborated with, using the photolithography and the soft lithography area. Thanks to Senior Engineer Gjertrud Maurstad at the Biophysics lab for giving me training at the AFM, showing me the lab routines and generally being helpful in practical matters.

Thanks to all my friends I have get to know during the last five years, for making my time as a student in Trondheim unforgettable. Finally, last but not least, thanks to Linn for being supportive and always cheering on me, you are highly loved.

Thor Christian Hobæk
Trondheim, June 2011

Contents

List of Figures

List of Tables

Chapter 1

Introduction

For centuries, humans have used nature as a source of inspiration to develop new innovative designs, a process termed bio-inspiration or biomimetics. Leonardo da Vinci, and later the Wright brothers, used the flight behaviour of birds as an inspiration for developing flight by machines. A more recent example is the commercial fabric hook-and-loop fastener Velcro, invented in 1941 by the Swiss engineer Georges de Mestral [1]. After examining seeds that kept sticking to his clothes and his dog's fur under a microscope, he discovered that the hooks of the seeds attached to anything with a loop. He then designed two synthetic fabrics, one covered with hooks and the other covered with loops, which were able to bind reversibly.

Through millions of years of evolution, a wide range of clever and ingenious designs have been developed to solve various problems associated with life. Biological materials are often formed through self-assembly of elements locally available [2]. The spontaneous organization of molecular units into ordered, hierarchical structures, gives the materials extraordinary properties. The building blocks typically consists of weak materials, such as proteins or minerals, and not metals as often used for engineered materials. However, multi-functional biological materials exist in nature, a result of a hierarchical arrangement of structures from the nano-scale to the macro-scale [3]. Some interesting examples worth mentioning is the self-cleaning effect of the Lotus leaves [4, 5], the ability to walk on water by the water strider [6, 7], the water fern who manage to stay dry when submerged under water [8, 9] and the Tokay gecko that can adhere reversibly to a range of different surfaces, in a range of different conditions [10].

The motivation behind this project is to develop a biomimetic device inspired by the water collection of the Namib Desert Beetle (*Stenocara gracilipes*), with applications within a droplet-based microfluidic system. Creatures living in arid areas are challenged by the shortage of water. The Namib Desert Beetle overcome this obstacle by collecting water from the morning fog [11]. The size of the fog droplets is small, $1 - 40$ μm in diameter, so they are easily carried by the wind. To collect water, the beetle brings its back to a tilt by raising its hind legs,

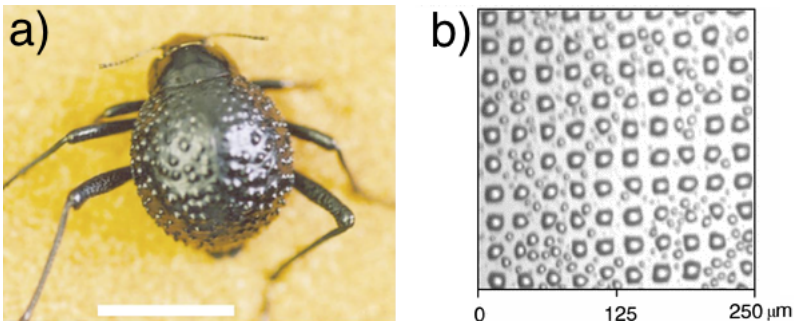

Figure 1.1: a) The Namib Desert Beetle has its back covered by alternating hydrophobic and hydrophilic regions (scale bar is 10 mm) [11]. b) Water vapour condense preferably in hydrophilic patterned regions on a hydrophobic background. The wetting contrast stems from selective UV-sensitive reactions using a photomask [12].

so that the humid air impacts the beetle's back. The surface structure of the beetle's back is bumpy, consisting of alternating wax-coated, hydrophobic areas and hydrophilic non-waxy regions at the peak of the bumps (see figure 1.1). The bumps are about 500 μm in diameter, separated by a distance of $500 - 1500$ μm. The hydrophilic regions have a smooth surface, whereas the hydrophobic regions have protuberances shaped as hemispheres with 10 μm in diameter, placed in an hexagonal array [11].

The hydrophilic regions act as seeding points where the water vapour condenses. During this process, droplets that are formed increase in size over time. Eventually, the droplets reach a critical size when the capillary forces attaching the droplet to the surface, are overcome by the sum of gravity and the force experienced by the wind. They then detach and start rolling over the hydrophobic areas towards the beetle's mouth, where they are consumed.

The main goal of this study was to produce surfaces with patterned wettability, mimicking the Namib Desert Beetle. Surfaces with patterned wettability may have potential within water-capturing devices, or within lab-on-a-chip applications, involving formation of precise volume drops or droplet manipulation of biological or chemicals samples and reagents [13], design of microchannels where liquid flow is constricted due to surface tension contrast [14], or within fabrication of DNA [15], protein or cell microarrays [16].

The wetting properties of a surface can be tuned through surface structuring, modifying the surface chemistry or a combination of both [17]. Previously, various methods for altering the surface wetting properties locally have been exploited, among them are selective deposition of hydrophilic polyelectrolytes on a superhydrophobic surface [18] or through photosensitive reactions using a photomask to change the surface chemistry of for instance plasma fluori-

nated polybutadiene films [12], sol-gel films deposited on alumina surfaces [19] or nanoporous polymer thin films [20]. All of these methods have produced significant contrast in water contact angle between the patterned and non-patterned regions on the surface. However, the fabrication process is either labour-intensive or require advanced equipment for the production of each surface. For applicable purposes, it would be advantageous with an inexpensive and rapid process, so that a large number of disposable devices could be produced. In addition, chemical modification of surfaces may degrade over time [17].

Surface structured polydimethylsiloxane (PDMS) surfaces is a promising strategy for wetting contrast. PDMS is an inherently hydrophobic material, with a water contact angle of about 105° [21]. As discussed later in section 2.1.3, introducing surface roughness of a hydrophobic material will increase the contact angle. PDMS is a polymer suitable for replicating a wide a range of template structures [22]. Superhydrophobic PDMS surfaces have previously been fabricated through replica moulding from the lotus leaf surface [23] or a microfabricated SU-8 resist pattern [24].

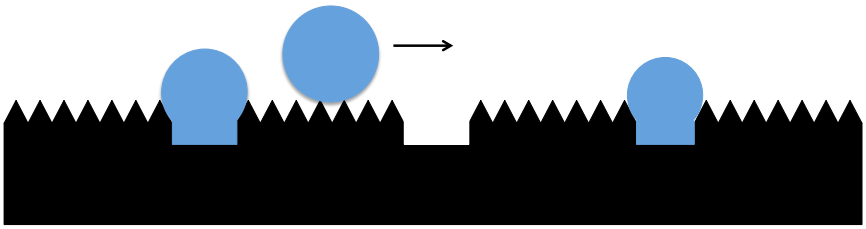

Figure 1.2: Schematic of the biomimetic device with patterned wettability, based on spatial differences in PDMS surface roughness. Ideally droplets deposited on the surface will only attach to the less hydrophobic, flat regions.

In this study, rough copper surfaces, prepared through etching, oxidation, electrodeposition or a combination according to previous work carried out by this research group [25, 26], have been used as template surfaces for replica. Rough PDMS surfaces have then either been made by directly replicating the copper surface, or from SU-8 moulds made as an intermediate fabrication step from the copper processing. Flat areas with a lower contact angle than the rough areas have been made by fabrication of SU-8 micropillars directly on rough copper surfaces or SU-8 moulds, using photolithography. A concept of the device is illustrated in figure 1.2. Ideally, droplets will roll of the rough surface and attach selectively to the flat regions. The captured droplets will then serve as anchored miniaturized reaction spots. The device could later be integrated with droplet movement systems, such as electrode-based electrowetting

or dielectrophoresis [27].

Chapter 2

Theory

Contents

In this section, an introduction to the relevant background theory necessary to understand the results and discussion is presented. First, the basic theory on wetting on flat and rough surfaces is presented. Then, some theory about surface roughness and methods to analyse surfaces are discussed. The basic theory on the underlying mechanisms that is responsible for creating roughness on copper through etching, oxidation and electrodepositon is covered. This is followed by a short introduction to photolithography and replica moulding with PDMS. Finally, the basics of the scanning electron microscope is presented.

2.1 Wetting

Wetting theory is describes the intermolecular interactions when a liquid is brought into contact with a solid surface. The degree of wetting is determined by the force balance between adhesive and cohesive forces. This theory is important in order to understand the mechanics behind surface physics involved in the examples discussed in the introduction. Terms like surface tension, surface energy, contact angles, contact angle hysteresis, hydrophobicity, hydrophilicity and the effect surface roughness has on the wetting properties will be discussed in this section.

2.1.1 Surface tension

Surface tension, represented by the symbol γ, has two equivalent definitions in physics, one definition is in terms of force, the other in terms of energy. The first definition is that surface tension is a force, which acts perpendicular and inward from a boundary of any surface or interface. This can be visualized by imagining a needle floating on the surface of water, see figure 2.1. The weight of the needle is balanced by a surface tension force given as

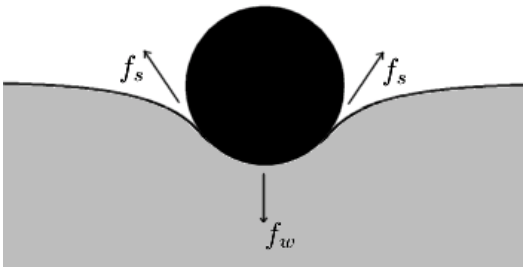

Figure 2.1: Cross-sectional diagram showing the balance of the gravitational and the surface tension force acting on the needle.

$$f_s = 2\gamma l \tag{2.1}$$

where l is the contact length of the water-needle interface (the factor of 2 is because the needle has two sides). The surface tension is therefore measured in force per unit length ($N\ m^{-1}$).

The other definition is thermodynamical in the terms of the work per unit area ($J\ m^{-2}$) required to produce a new surface, given by

$$\delta w = -\gamma dA \tag{2.2}$$

where a decrease in area A (negative dA) corresponds to the work w done by the system, whereas an increase in surface area (positive dA) requires work to be done on the system. For a reversible process at constant temperature and pressure, the work corresponds to the change in Gibbs free energy G [28]. Thus,

the thermodynamic definition of surface tension is given by the increment in Gibbs free energy per unit increment in area:

$$\gamma = \left(\frac{\partial G}{\partial A}\right)_{T,p} \tag{2.3}$$

The effect of surface tension is therefore to decrease the interface area between gas, solid or liquid, because thermodynamics requires any spontaneous process to be accompanied by a decrease in Gibbs free energy.

2.1.2 Wetting on smooth surfaces

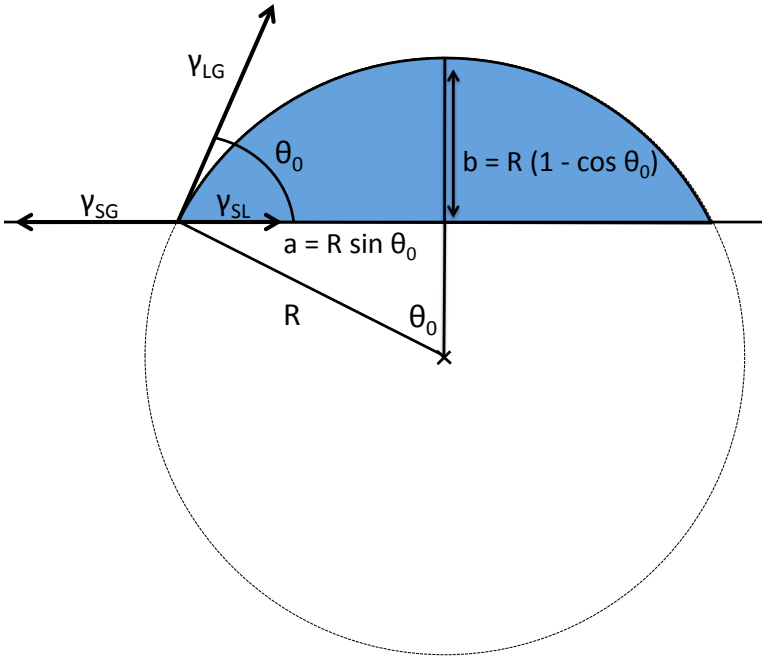

Figure 2.2: Illustration of the force balance involving surface tensions for a three-phase system in equilibrium when a droplet is placed on a flat solid substrate

The contact angle is defined as the angle at which a liquid/gas interface meets a solid interface (often called the triple line [29]). A droplet in figure 2.2, resting on a surface with a contact angle θ_0, is a portion of a sphere with radius R, cut off by the surface plane (spherical cap). The droplet have a volume $V = \frac{\pi b}{6}(3a^2 + b^2)$, which after insertion of the contact angle and sphere radios can be written as

$$V = \frac{\pi R^3}{3}(1 - \cos\theta_0)(2 + \cos\theta_0) \tag{2.4}$$

Furthermore, the droplet have a solid-liquid interface area $A_{SL} = \pi \left(R \sin\theta_0\right)^2$, and a liquid-gas surface area $A_{LG} = 2\pi R^2 \left(1 - \cos\theta_0\right)$. The Gibbs free energy of the droplet is expressed as

$$G = A_{LG}\gamma_{LG} + A_{SL}\left(\gamma_{SL} - \gamma_{SG}\right) \tag{2.5}$$

where γ_{SG}, γ_{SL} and γ_{LG} is the surface tension of the solid-gas, solid-liquid and liquid-gas interface respectively. Substituting the droplet volume and the interface areas into equation 2.5, yields

$$G = \left[\frac{9\pi V^2}{\left(1 - \cos\theta_0\right)\left(2 + \cos\theta_0\right)^2}\right]^{\frac{1}{3}} \left(2\gamma_{LG} - \left(\gamma_{SL} - \gamma_{SG}\right)\left(1 + \cos\theta_0\right)\right) \tag{2.6}$$

Assuming a constant volume of the droplet, the thermodynamic equilibrium can be found by derivation of equation 2.6 and setting it equal to zero:

$$\frac{dG}{d\theta_0} = \left[\frac{9\pi V^2}{\left(1 - \cos\theta_0\right)^4\left(2 + \cos\theta_0\right)^5}\right]^{\frac{1}{3}} 2\left(\left(\gamma_{SL} - \gamma_{SG}\right) - \gamma_{LG}\cos\theta_0\right)\sin\theta_0 = 0 \tag{2.7}$$

The condition for the equilibrium contact angle θ_0 is fulfilled when

$$\gamma_{SL} - \gamma_{SG} = \gamma_{LG}\cos\theta_0 \tag{2.8}$$

which after rearrangement gives the Young-Dupré equation) [28]:

$$\cos\theta_0 = \frac{\gamma_{SG} - \gamma_{SL}}{\gamma_{LG}} \tag{2.9}$$

This equation represents the force balance illustrated in figure 2.2 of adhesive and cohesive forces, which acts between the three different phases. Adhesive forces between a water droplet and a solid surface will cause the droplet to spread out, making as large contact area as possible. Cohesive forces will try to minimize the water-solid interface area. Shifting of this force balance will affect the contact angle and thus the degree of wetting. In terms of energy, it can be said that this relation express the ratio between the energy gained and energy required to form a unit area interface between solid, liquid and gas. If the surface tension of the solid-liquid interface is very high relative to the solid-gas interface, the droplet will reduce this interface area at the expense of increasing the liquid-gas interface area. If this is taken to the extreme, the solid-liquid

interface will be equal to zero. The droplet will then assume the shape of a perfect sphere ($\theta_0 = 180°$), since this is the only way it can minimize Gibb's free energy (a sphere has the lowest surface/volume ratio theoretically possible). On the other hand, if the solid-liquid surface tension is very low relative to the solid-gas interface, the opposite will happen; the droplet will spread out as much as possible on the solid surface ($\theta_0 = 0°$).

2.1.3 Wetting on rough surfaces

Introducing surface roughness to the system in figure 2.2 changes the equilibrium contact angle to θ. Due to the surface roughness, the liquid-solid interface area A_{SL} in equation 2.5 have increased by a factor r. The roughness factor r is defined as the ratio of the surface area in contact with the liquid droplet to the projected area as seen towards the horizontal plane. After insertion of the new interface area A_{SL} in equation 2.5, it can be seen that the equilibrium contact angle equals

$$\cos\theta = r\left(\frac{\gamma_{SG} - \gamma_{SL}}{\gamma_{LG}}\right) = r\cos\theta_0 \tag{2.10}$$

This relation was developed by Wenzel and is therefore appropriately called the Wenzel equation [30]. This relation shows that the contact angle θ of water on a rough surface is proportional to the contact angle of an ideally flat surface θ_0 described in equation 2.9.

The effect of introducing surface roughness by increasing r is demonstrated in figure 2.3. For an intrinsic hydrophobic surface, the hydrophobicity is increased, while for an intrinsic hydrophilic surface, the hydrophilicity is increased.

Later, Cassie [32] proved that this model is only true for a homogeneous liquid/solid interface. When air pockets form at the interface, the surface must be considered as heterogeneous. The heterogenous surface is composed of two phases. The interface area between the water droplet and the two phases are given by the fractional areas, f_1 of phase 1 and f_2 of phase 2 respectively, which sums are equal to 1. The contact angle θ of a hetero-

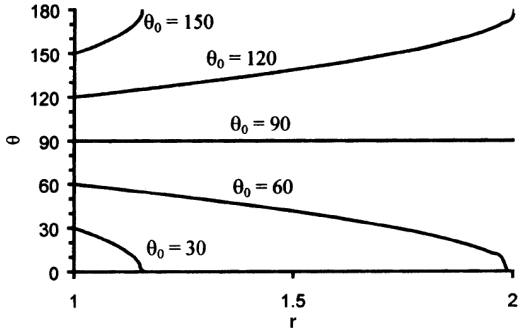

Figure 2.3: The Wenzel model illustrated for different smooth contact angles. Surface roughness amplifies hydrophobicity or hydrophilicity [31].

geneous rough surface surface is given
by the Cassie-Baxter equation

$$\cos\theta = f_1 \cos\theta_1 + f_2 \cos\theta_2 \tag{2.11}$$

where θ_1 and θ_2 are the contact angle between water and the two respective phases. When f_1 corresponds to the solid-liquid fraction ($f_1 = f_{SL}$, $\theta_1 = \theta_0$), and f_2 corresponds to the liquid-gas fraction ($f_2 = f_{LG} = 1 - f_{SL}$, $\theta_2 = 180°$), equation 2.11 reduces to

$$\cos\theta = -1 + (1 + r_f \cos\theta_0) f_{SL} \tag{2.12}$$

where r_f is the roughness factor of the wetted area. It is important to realize that when the solid is completely wetted, $r_f = r$ and $f_{SL} = 1$, and equation 2.12 reduces to the Wenzel model of a homogeneous surface. The difference between the Wenzel and Cassie-Baxter wetting states is illustrated in figure 2.4.

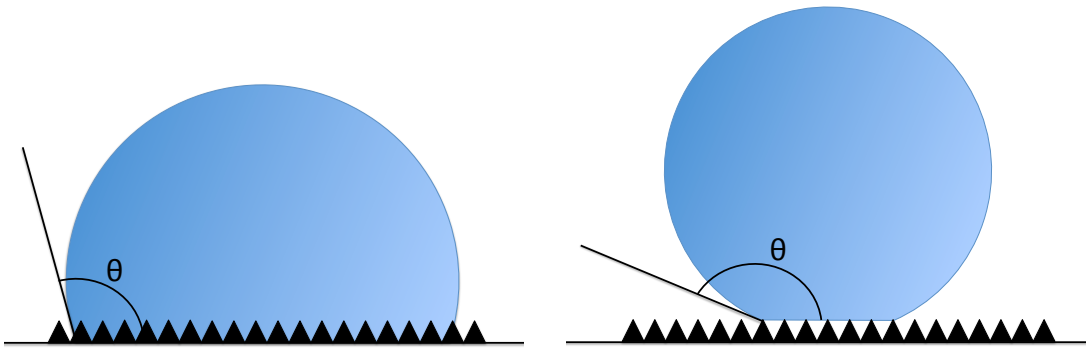

(a) Wenzel state (b) Cassie-Baxter state

Figure 2.4: Schematics of the different wetting states on rough surfaces. In a), the liquid-solid interface is homogeneous (Wenzel state), while in b), the interface is heterogeneous (Cassie-Baxter state)

Even though both states describe surface-enhanced hydrophobicity, the macroscopic behaviour of water droplets in the different states can be very different. Generally, surfaces following the Wenzel state tends to be "sticky", so that water adheres more strongly than for a similar flat surface [33]. Oppositely, surfaces following the Cassie-Baxter state tends to be "slippery", so that water droplets roll off more easily. For the Cassie-Baxter state, roll-off angles as low as 1°have been observed [34].

The "stickiness" of a surface can be described by measuring the contact angle hysteresis, which is the difference the between advancing contact angle θ_a and the

receding contact angle θ_r for droplet a rolling down a tilted surface, illustrated in figure 2.5. Related to this discussion, droplets in the Wenzel state generally have a high hysteresis, while droplets in the Cassie-Baxter state have a low hysteresis.

There are also cases where the wetting can be described as a combined Cassie-Baxter/Wenzel state, where the surface have a very high contact angle and water adheres strongly, which may be the case for surfaces with a high intrinsic contact angle hysteresis [17].

The definition of a superhydrophobic surfaces is not clear, as many reports use different terminology [17]. Some sources use a contact angle of 150°as the definition of a superhydrophobic surface, while others require the roll-off angle of a water droplet to be low, characteristic of the Cassie-Baxter state.

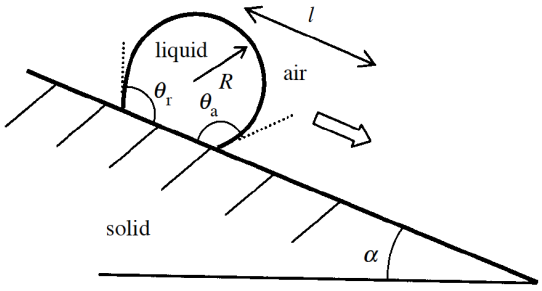

Figure 2.5: Schematics illustrating the advancing contact angle θ_a, the receding contact angle θ_r and the roll-off angle α for a droplet [35].

2.2 Surface analysis

As mentioned, surface textures affect the wetting behaviour of solid surfaces, in terms of increased surface area and increased hydrophobicity/hydrophilicity. Surfaces can be characterized qualitatively using optical or electron microscopy techniques. However, it may be useful to retrieve quantitative data of the surface roughness, in order to predict the wetting behaviour.

2.2.1 Surface roughness amplitude parameters

Surface roughness refers to height variations of the surface with respect to a reference plane, measured along a single line profile or parallell lines in a surface map. Engineering surfaces are often random, isotropic or anisotropic, Gaussian or non-Gaussian [36]. The two most common measures for the surface roughness are the arithmetic average R_a and the standard deviation σ, defined by the

surface height z, the scan length L, the horizontal mean line of the surface profile m and the root mean square roughness R_q as

$$R_a = \frac{1}{L}\int_0^L |z - m|\, dx \tag{2.13}$$

$$\sigma^2 = \frac{1}{L}\int_0^L (z - m)^2 dx = R_q^2 - m^2 \tag{2.14}$$

$$R_q^2 = \frac{1}{L}\int_0^L (z)^2 dx \tag{2.15}$$

and

$$m = \frac{1}{L}\int_0^L z dx \tag{2.16}$$

From σ and m, the probability density function of the height for a Gaussian surface can be described according to

$$p(z) = \frac{1}{\sqrt{2\pi}\sigma}\exp\left[-\frac{(z-m)^2}{2\sigma^2}\right] \tag{2.17}$$

Usually, the surface roughness data are corrected for tilt or curvature, and the mean line is subtracted from the raw data, so that $m = 0$. In this case, σ is reduced to the root-mean square R_q.

However, not all surfaces are Gaussian. To quantify non-Gaussian surfaces, two other statistical quantities used are the skewness (Sk) and kurtosis (K) given as

$$Sk = \frac{1}{\sigma^3 L}\int_0^L (z - m)^3 dx \tag{2.18}$$

and

$$K = \frac{1}{\sigma^4 L}\int_0^L (z - m)^4 dx \tag{2.19}$$

These two latter quantities describe the symmetry of the height distribution from the mean line of the surface. A Gaussian surface, which has a Gaussian height distribution, has zero skewness, which means that there are an equal number of peaks and valleys at a certain distance from the mean line [37]. Positive skewness means that there is a larger number of peaks than valleys, negative skewness means the number of valleys are larger than peaks. A Gaussian surface has a kurtosis of 3. If $K<3$, the surface has relatively few sharp peaks and valleys, compared to a surface with $K>3$. This means that the kurtosis will be

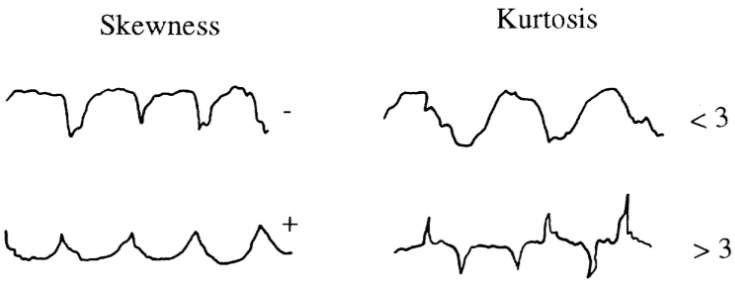

Figure 2.6: Line profiles for non-Gaussian surfaces with different skewness and kurtosis [37].

higher for a spiky surface than a bumpy surface. Line profiles of non-Gaussian surfaces with different skewness and kurtosis are illustrated in figure 2.6. Furthermore, the probability density functions of Gaussian and non-Gaussian surfaces are compared in figure 2.7.

2.2.2 Spatial analysis of surfaces

Roughness amplitude parameters discussed so far, such as the average roughness R_a, root mean square roughness R_q, skewness Sk and kurtosis K, gives useful surface characteristics. However, surface roughness can occur at different length scales, from the nano-scale to the macro-scale. When analysing multi-scale hierarchical surfaces, it is therefore useful to quantify them in terms of spatial functions. One of these is the autocorrelation function, $R(\tau)$, which is a measure of self-similarity of the line profile $z(x)$ shifted a distance τ:

$$R(\tau) = \lim_{L\to\infty} \frac{1}{L} \int_0^L z(x)z(x+\tau)dx \tag{2.20}$$

The normalized form of the autocorrelation function $C(\tau)$ is defined as

$$C(\tau) = \lim_{L\to\infty} \frac{1}{L\sigma^2} \int_0^L [z(x) - m]\,[z(x+\tau) - m]\,dx = \frac{[R(\tau) - m^2]}{\sigma^2} \tag{2.21}$$

Many engineering surfaces show an exponentially decaying autocorrelation function [36],

$$C(\tau) = \exp(-\frac{\tau}{\beta}) \tag{2.22}$$

where β is the distance at which the autocorrelation function falls to $1/e$. More often, the correlation length, β^*, is defined as the value of τ when $C(\tau)$

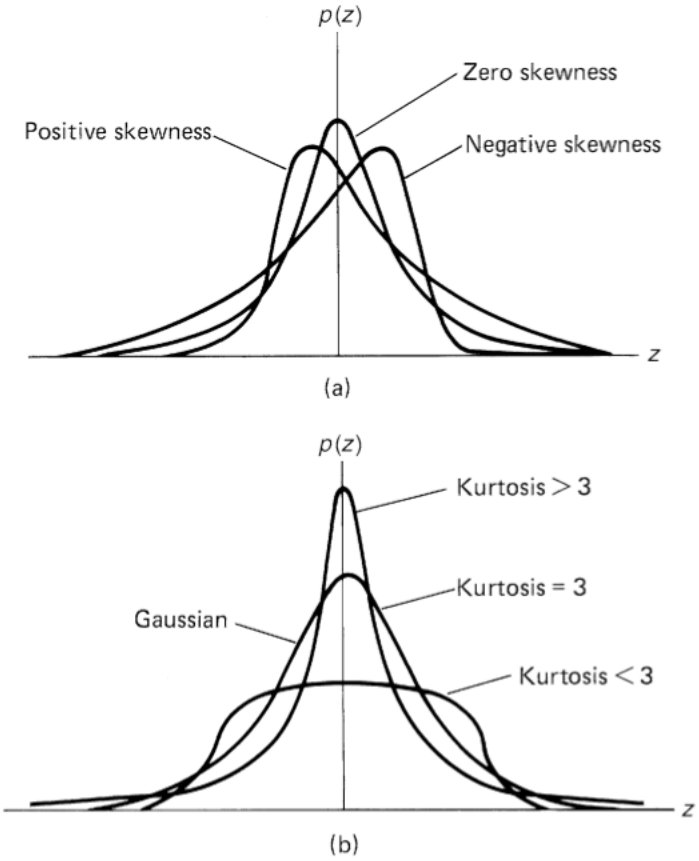

Figure 2.7: Probability density functions for surfaces with different skewness (Sk) a) and kurtosis (K) b) [38].

has decayed to 10% of its origininal value ($C(\beta^*) = 0.1$). Two points on a line profile separated by this distance are considered to be independent of each other. Thus, the correlation length can be viewed as a measure of randomness, with increasing surface randomness with decreasing β^*.

From the discussion of quantitative surface roughness parameters so far, only two parameters are necessary to characterize surfaces with a Gaussian height distribution and exponential autocorrelation, that is the standard deviation, σ, and the correlation length, β^* [36]. σ is the amplitude parameter describing the height of a typical roughness detail, while β^* is a parameter describing the length of that detail along the scanning direction [39]. To achieve superhydrophobic surfaces, a transition from the fully wetted Wenzel state to the composite wetting Cassie-Baxter state is necessary, as discussed in section 2.1.3. Nosonovsky et. al. [31] showed that the contact angle of a rough surface in the Wenzel state increased with increasing value of the ratio σ/β^*, and that this value is proportional to the average absolute value of the slope of surface features. Using this analysis as a guide for surface optimization, one should either increase the standard deviation, σ, or decrease the correlation length, β^*.

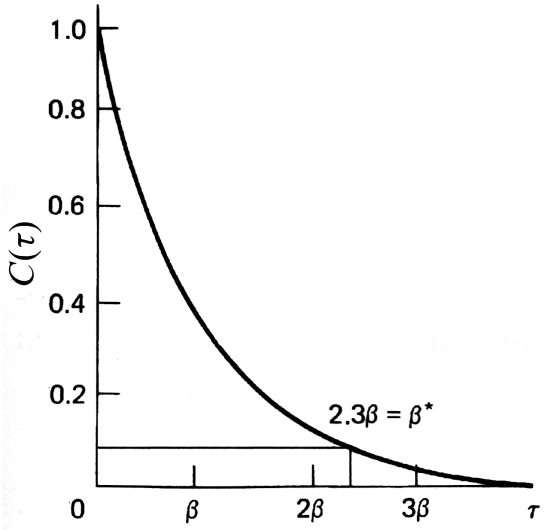

Figure 2.8: The exponentially decaying normalized autocorrelation function $C(\tau)$, with the indicated correlation length β^* [36].

2.3 Measuring surface roughness

Quantitative surface roughness measurements are useful to compare different surfaces, and to optimize the process of making superhydrophobic surfaces. Different techniques are available for this purpose, such as the mechanical stylus, atomic force microscopy, optical methods such as specular reflection, diffuse scattering or optical interference, and roughness information obtained from backscattered electron signals using a scanning electron microscope (SEM) [36].

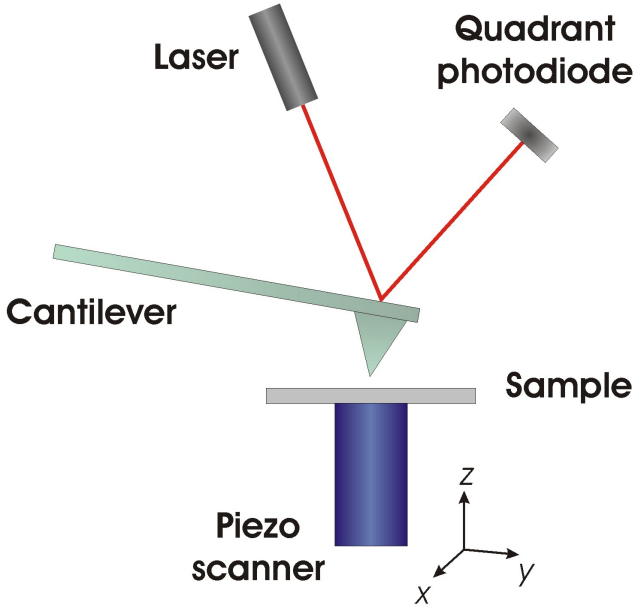

Figure 2.9: Schematic explaining the basic set-up of the atomic force microscopy (AFM), which includes the tip and cantilever, a photodiode detector system and a piezoelectric scanner[1].

2.3.1 Mechanical profilometer

The profilometer measures the surface roughness by recording the vertical displacement of a stylus diamond-tip, which is scanned in contact with the sample at a constant speed [36]. The stylus tip is loaded against the surface with a small force and is mechanically coupled to a linear variable differential transformer (LVDT) [40]. A constant applied force to the surface is ensured by a force coil mechanism. Surface deviations cause the stylus to displace vertically. The LVDT detector converts this displacement to an analogue signal, which is further converted to a digital signal. Coupled to the measurement head is an optical CCD-camera, which enables the user to position the desired features beneath the stylus. During scan, the sample stage is moved at a constant speed in the x-direction. After the desired scanning length has been achieved, the stylus automatically retracts from the sample. An advantage with the profilometer is that it is a relatively fast method for obtaining roughness information, and can support scan lengths of several millimetres [40]. However, for high-resolution roughness measurements at the nanoscale, the atomic force microscopy (AFM) is a much better suited instrument.

2.3.2 Atomic force microscopy

Atomic force microscopy (AFM) is a scanning probe microscopy (SPM) technique with similarities to the mechanical profilometer; it probes the surface with a small tip rather than acquiring an optical image [41]. However, the AFM is a tool with a far higher vertical and lateral resolution than the profilometer. It can be used to image surface features down to the atomic scale. In addition, AFM can be used to image virtually any kind of solid material, as opposed to scanning tunneling microscope (STM), another SPM instrument, which requires that the sample is conductive.

The main parts of the AFM are the tip, the tip holder constituting the cantilever and the detector system, the scanner and the feedback system. The tip and cantilever is usually made of silicon or silicon nitride, and comes in various geometries suitable for specific applications. The tip is conical and extremely sharp, with a radius of curvature down to 10 nm [36], and determines the lateral resolution of the surface image. Most AFMs are based on piezoelectric scanners, which deforms mechanically in response to an applied electric voltage. The most commonly used configuration, and the one used in this project, is the tube scanning system, which ensures sub-nanometer precision of the sample positioning in the x-, y- and z-direction. The detector system is based on a laser beam incident on the backside of the cantilever. The position of the reflected laser beam is recorded by a photodiode. The detector usually consists of four regions, which records the intensity of the reflected beam. In the equilibrium position of the cantilever, the intensity is equally distributed among the different regions. The cantilever bends up or down in response to interaction forces caused by height variations, or twists due to lateral forces, caused by friction. This results in a beam shift and a difference in the signal intensity between the different regions. The electronic feedback system are used to adjust the vertical position of the scanner in response to a shift in the intensity, so that the position of the laser beam remains at the center of the detector. The vertical movement of the scanner is then directly translated into height variations at the sample surface.

The AFM operates by measuring the intermolecular forces between the tip and surface. Depending on the sample or imaging conditions, the forces measured could be van der Waals forces, capillary forces, chemical bonding or electrostatic forces. The London dispersion force, the force between two induced

[1] http://www.few.vu.nl/ wroos/AFM-schematics.html

dipoles, is an important contribution to the van der Waals force because it is always present [42]. The magnitude of the van der Waals interaction forces depend on the tip-sample separation distance, and can be modelled according to the Lennard-Jones potential between two interacting atoms

$$\Psi = 4\varepsilon \left\{ \left(\frac{\sigma}{r}\right)^{12} - \left(\frac{\sigma}{r}\right)^{6} \right\} \tag{2.23}$$

where r is the inter-atomic separation distance, ε is the magnitude of the energy-minimum potential and σ is the separation distance where the potential is equal to zero. The r^{-12} term is the repulsive term, while the r^{-6} term is the attractive term. The attractive term is dominant at large separation distances. As r decrease, the magnitude of both components increase. The global potential minimum occurs at the equilibrium distance $r_0 = 2^{\frac{1}{6}}\sigma$. Bringing r closer to zero, leads to a rapid increase in repulsive force. In contact mode (also called static mode), the scanning is often operated by maintaining a constant force at the equilibrium distance, where the tip is in contact with the surface. When the tip-sample separation distance increase or decrease from this value due to height variations, the cantilever is deflected since it experience an increase in attractive or repulsive forces. To translate the cantilever deflection to the repulsive force acting on the tip as it moves closer to the surface than r_0, requires knowledge of the cantilever stiffness, measured in terms of the spring constant k [Nm^{-1}]. The repulsive force F is then approximated by Hook's law, by assuming that the cantilever is a harmonic oscillator:

$$F = -kx \tag{2.24}$$

The AFM can also be operated in dynamic mode, which includes tapping mode and non-contact mode. In tapping mode, the cantilever is forced to oscillate at a larger distance from the surface than in contact mode, at a frequency close to its resonance frequency while scanning over the surface. Tapping the surface reduce the problem of deforming the sample associated with contact mode, because the tip is in contact with the surface for only a small fraction of the oscillating period.

The vertical movement of a cantilever with forced sinusoidal oscillations can be described by a second order differential equation:

$$m\frac{d^2z}{dt^2} + \gamma\frac{dz}{dt} + kz = F_0 \sin\omega t \tag{2.25}$$

where m is the effective mass of the tip-cantilever system, γ a damping coefficient, k the spring constant and $F_0 \sin \omega t$ the oscillating driving force. After some rearrangements, the equation can be written as:

$$\frac{d^2z}{dt^2} + \frac{\omega_0}{Q}\frac{dz}{dt} + \omega_0^2 z = \frac{F_0}{m}\sin \omega t \tag{2.26}$$

where $\omega_0 = \sqrt{\frac{k}{m}}$ is the driving frequency that results in a maximum amplitude, called the resonance frequency, and $Q = \frac{m\omega_0}{\gamma}$ is the quality-factor, which is a measure of the bandwith of the resonance peak. The vertical movement has a steady-state solution of the form

$$z = A \sin(\omega t + \phi) \tag{2.27}$$

where A is the oscillating amplitude and ϕ is the phase lag of the oscillations relative to driver, which could be written as:

$$A = \frac{F_0/m}{\left[\left(\omega_0^2 - \omega^2\right)^2 + \left(\omega\omega_0/Q\right)^2\right]^{1/2}} \tag{2.28}$$

and

$$\tan(\phi) = \frac{\omega\omega_0/Q}{\omega_0^2 - \omega^2} \tag{2.29}$$

The frequency-dependence of these functions are illustrated in figure 2.10. In dynamic mode, the driving frequency is chosen to be close to the resonance frequency. In this area, the frequency dependence on the amplitude and phase lag is strong. When the cantilever is interacting with the sample surface, a force term $F_{int}(z)$ is inserted into the right hand side of equation 2.25. The introduction of an external force in the equation leads to a new steady-state solution, and thus a change in the resonance frequency and phase, if the driving force is kept constant. The magnitude and polarity of the interaction force depends on the tip-sample separation distance as previously discussed. When the tip is scanned across the sample, height variations lead to changes in the oscillating amplitude or phase. When the cantilever is run in frequency modulation mode, the oscillating amplitude is kept constant by the feedback loop, which moves the sample stage up or down. A surface map is then generated based on changes in the oscillating frequency. In the amplitude modulation mode, the opposite is true; the frequency is kept constant and changes in amplitude are detected.

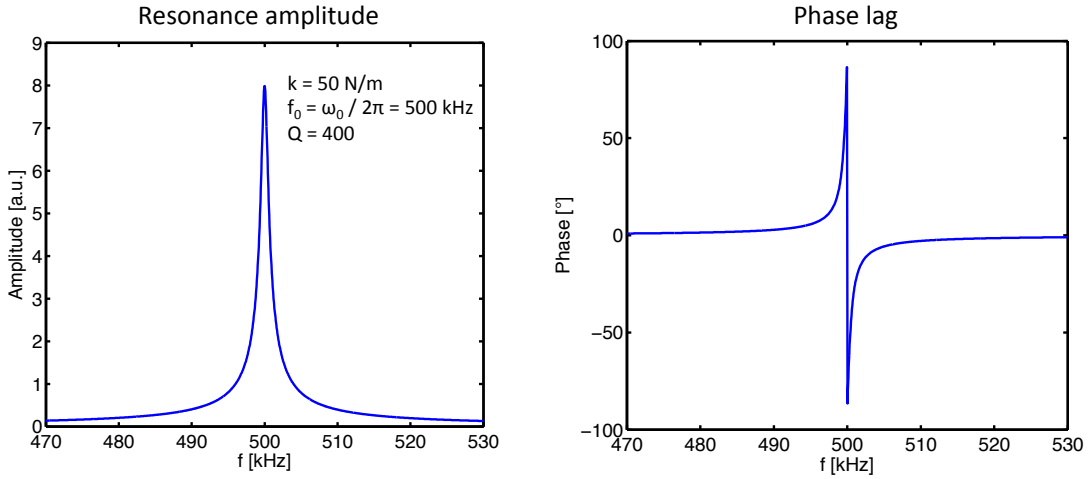

Figure 2.10: The oscillating amplitude and phase lag as a function of the cantilever driving frequency for a harmonic oscillator, with representative values of the cantilever spring constant k, resonance frequency f_0 and quality-factor Q.

Non-contact mode is the third operating mode. It is also based on forced oscillations of the tip, but the tip-sample distance is larger than for tapping-mode. Because of this, the tip-sample interaction forces are of a very small magnitude, which is difficult to detect. Thus, the resolution is poor compared to contact and tapping mode. It is therefore only used to image soft and elastic samples.

Contact mode is able to give atomic resolution for some samples, however it can deform features on the sample due to high loading forces or insufficient response time of the feedback system. This is a particular problem for biological samples, as they are soft. Thus, AFM scanning is usually run in tapping mode for these kinds of samples.

Since the AFM operates at length scales down to the sub-nanometer regime, it is particular vulnerable to various sources of noise, such as mechanical vibrations, electronic noise or thermal fluctuations. Usually, cantilevers with a low spring constant is used in contact mode to achieve atomic resolution, since an elastic cantilever will have a large deflection in response to small changes in the tip-sample interaction force. In dynamic mode however, cantilevers with a high spring constant is often desirable. One reason is to minimize the sensitivity to noise generated by mechanical vibrations. This is also reduced by placing the AFM instrument on a vibration-dampened table. In addition, the sensitivity of thermal noise induced by Brownian motions are reduced by using a high spring constant. Thirdly, such kind of cantilevers also respond less to long-range van der Waals forces from the surface, which may sometimes cause the oscillating

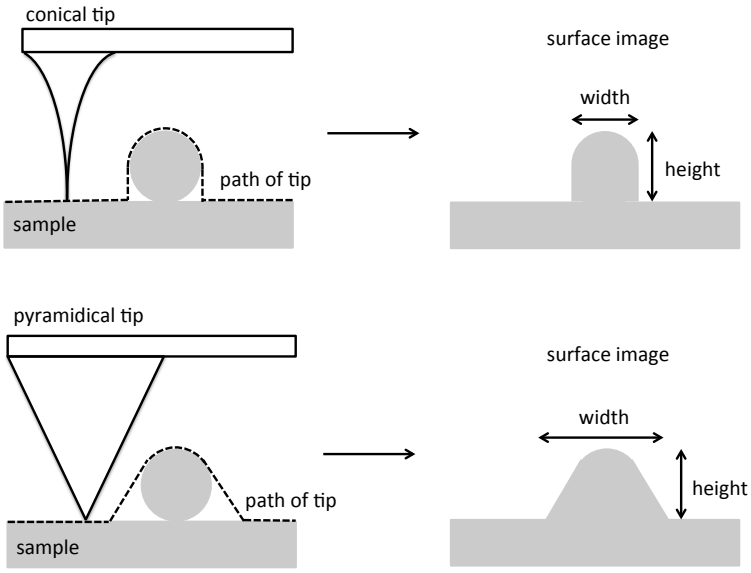

Figure 2.11: Illustration of tip convolution, an image artefact limiting the lateral resolution of AFM. An atomically sharp tip will image the real dimensions of surface features. However, when less sharp tips are used, the measured lateral width will be larger than the real width as illustrated. The measured height is not affected by tip convolution.

tip to "snap" into contact with the sample, leading to imaging artefacts [42].

The lateral resolution of features that can be imaged are limited by the tip geometry, a phenomenon called tip convolution. This phenomenon is illustrated in figure 2.11. Features with steep side-walls, such as sharp protrusions or deep and narrow valleys, are difficult to image, as the geometry of the tip is often too large. Scanning of nanoscale surface features usually lead to exaggerated measurements of the lateral dimensions, due to the relatively large size of the tip, as shown in the figure. However, the measured vertical height of the object is not affected by tip convolution. The sharpness of the tip is usually specified as the radius of curvature. The radius of curvature increase over time, due to mechanical wear or deposition of sample material on the tip. Extremely sharp tips can be made by attaching carbon nanotubes (CNTs) at the end of conventional silicon cantilever tips [43].

Although AFM is superior to the profilometer when it comes to resolution, the x-, y- and z-range it can cover in one scan is limited. Additionally it is a relatively slow method. Thus, AFM is most suitable for measuring the nanometer-scale surface roughness, while the profilometer is useful to give a rapid evaluation of the microscale roughness.

2.4 Copper processing

2.4.1 Copper etching

Cupric chloride etchants are widely used in the industry, for instance in the production of printed circuit boards, due to its high etch rate and easy regeneration [44]. Cupric chloride attacks the uncoated copper surface and forms copper(I) ions:

$$CuCl_2 + Cu \longrightarrow 2CuCl$$

and

$$\underset{\text{cupric}}{Cu^{2+}} + \underset{\text{metal}}{Cu^0} \longrightarrow \underset{\text{cuprous}}{2Cu^+}$$

CuCl is insoluble in water [45], and forms a slightly green layer that covers the metallic copper surface, so that any further etching stops. However, HCl reacts with CuCl to form $CuCl_2$, so if the hydrochloric acid is added to the etchant solution, the etching continues:

$$CuCl_2 + 2HCl + Cu \longrightarrow 2CuCl + 2HCl$$

The Cu^+ ions in the solution also form other strong complexes with chloride, mostly $[CuCl_2]^-$ and $[CuCl_3]^{2-}$ [46], but also $[CuCl_4]^{3-}$ [25]. Cu^{2+} ions may also form complexes with chloride, though they are weaker, in the form of $[CuCl]^+$.

After use, the waste $CuCl_2$ etchant can be regenerated to be usable again by adding an oxidative agent, for instance hydrogen peroxide, H_2O_2:

$$2CuCl + H_2O_2 + 2HCl \longrightarrow 2CuCl_2 + 2H_2O$$

This is an environmental advantage, as it minimizes or eliminates environmental pollution during and after the etching process, in addition to reducing operational costs [44].

2.4.2 Copper oxidation

Oxidation of copper at temperatures around 500° C leads to growth of CuO nanowires [47]. Thus, it produce a different surface roughness than what can be obtained by etching alone. The oxidation occurs in two steps and forms a

layered structure [48]. First, a red coloured layer of Cu_2O forms directly on the Cu surface

$$4Cu + O_2 \longrightarrow 2Cu_2O$$

Through the second step of oxidation, a black coloured layer of CuO forms through a slow reaction with Cu_2O:

$$2Cu_2O + O_2 \longrightarrow 4CuO$$

The actual growth mechanisms is currently under debate. One proposed mechanism explains the growth by grain-boundary diffusion of copper ions through the Cu_2O layer. Most copper ions tend to reach the top surface at the same spots, which acts as nucleation points for continuous growth of the CuO nanowires [49].

2.4.3 Copper electrodeposition

Electrodeposition is an alternative method of introducing roughness on copper plates [25]. Electrodeposition is a process where metal ions in a solution is moved to coat an electrode in the presence of an applied electric field [50]. In the case of copper electrodeposition, an anode and a cathode, both made of copper, are placed in a sulfate bath and coupled to an external supply of direct current (DC). The electric current oxidize the copper on the surface of the anode to Cu^{2+} by losing two electrons. At the cathode, the Cu^{2+} in the solution are reduced to metallic copper by gaining two electrons.

This process results in a flat, thin layer of metal copper deposited on a copper plate. However, if electrodeposition is carried out using a high potential, the reduction of Cu^{2+} to metallic copper competes with electrolysis of water, producing hydrogen bubbles at the cathode:

$$2H^+ + 2e^- \longrightarrow H_2$$

The formation of bubbles acts as a temporary template, where Cu is electrodeposited within the interstitial spaces between the hydrogen bubbles, to form a macroporous film of Cu nanoparticles [51, 52] Copper is not deposited where there is a hydrogen bubble, because there are no copper ions available.

2.5 Photolithography

Photolithography is a conventional technology of patterning within micro-fabrication, and has been the workhorse of semiconductor industry since its invention in 1959 [53]. The process procedure involves selective exposure of a thin film of resist on the substrate, through a mask pattern typically made by deposition of an opaque chromium layer on quartz-glass. Features smaller than 45 nm can be produced by photolithography, using an ultraviolet light with a 193 nm wavelength and replacing the air gap between the lens and substrate with a liquid (immersion lithography), which improves the optical resolution by increasing the refractive index [54]. Photolithography typically contains eight steps. First, the substrate to be patterned is cleaned of contaminants and dehydrated to improve adhesion. Then, a layer of a liquid photo-active polymer (resist) is applied on the substrate surface through spin-coating, where the thickness of the resist layer is controlled by the rotation speed. To further enhance adhesion between the resist and the substrate, and to evaporate solvent in the resist, the wafer is soft baked on a hot plate.

Before exposure, the wafer is placed under a mask-aligner to control the position of the pattern on the substrate. Photolithography can be divided into categories depending on the radiation source used; UV, electron-beam or X-ray. The resolution of the pattern is limited by the wavelength of the source. UV-lithography (i-line, 365 nm) is the traditional light source, although DUV (193 nm), e-beam and X-ray lithography (sub-nanometer wavelengths) are able to produce controlled structures with finer resolution. For a negative resist, such as SU-8, exposure leads to the generation of a photoacid, which acts as a catalyst in a cross-linking reaction between the long molecular chains of the polymer resist. For positive resists, the opposite is true; the exposed areas is softened and rendered soluble. The exposure step is very important as this is the step where the wafer is actually patterned. The required exposure dose, given as J m^{-2}, has to be optimized for each application, and depends on what type of resist is used and the film thickness. Different mask-aligner systems has been developed over time, from the first contact aligners, where the substrate is placed in direct contact with the mask and exposure is performed in one step, to the more modern step-and-scan system, where the mask is projected onto the substrate through a lens, and exposure is a multi-step process where the mask pattern is stepped to the next area in a scanning motion. This permits smaller patterns, as the mask pattern is demagnified onto the substrate.

Following exposure, the resist is baked once more on a hot plate, called post-exposure bake (PEB). For negative resists, heating above the glass transition temperature of the polymer catalyse the cross-linking reaction in the exposed areas, which is very slow at ambient temperatures. Furthermore, it improves the mechanical stability of the cross-linked polymer. The soluble resist is then removed in a developing step, where a liquid chemical developer is applied. During development, one will often start to see the formation of a pattern. For optimum stabilization of the resist structure, a final baking step is performed at the end, called hard bake. This is especially important in cases where the resist should remain on the substrate as a part of the final device, or when a large temperature-tolerance is needed. The final step of photolithography involves characterizion by optical microscopy, SEM or AFM for the smallest structures. If the pattern is not satisfactory, the resist can often be removed by a solvent and the process repeated from step 1. Depending on the application, the resist pattern is used as a mask for selective etching or ion implantation of the exposed substrate material.

2.6 Replica moulding

Although photolithography is the dominant technology of microfabrication, it has several disadvantages. The resolution is limited by optical diffraction, the process requires complex facilites and technologies, it is expensive, cannot easily be applied to non-planar surfaces and it provides very little control of the surface chemistry of the patterned regions. Therefore, a technology called "soft lithography" based on patterned elastomers as masks, stamps or molds, was developed to complement the requirements in microfabrication, which photolithography can't provide [22]. Some of the existing soft lithography techniques are microcontact printing (μCP) [55], replica molding (REM) [56], microtransfer molding (μTM) [57], micromolding in capillaries (MIMIC) [58] and solvent-assisted micromolding (SAMIM) [59].

Replica moulding is a method where three-dimensional topologies are replicated using an elastomer, such as the silicone polydimethylsiloxane (PDMS), constituting of repeating $SiO(CH_3)_2$ units, see figure 2.12. The resolution of the replica is determined by the resolution of the template pattern, and the wetting of the mould. Complex structures of the master mould can be copied multiple times with nanometer resolution, making replica moulding a relatively inexpensive and simple method. In addition, it does not require advanced laboratory

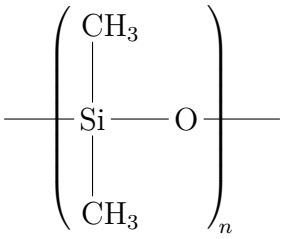

Figure 2.12: Chemical formula of the polydimethylsiloxane (PDMS) monomers.

equipment.

The process steps are summarized in figure 2.13 [60]. First, the liquid prepolymer of PDMS is made by mixing a monomer with a curing agent, often in a 10 to 1 weight ratio. During mixing, a lot of air is trapped as bubbles in the mixture. Air bubbles in the silicone are removed by degassing the mixture in a vacuum desiccator until it is clear and transparent. Then, the liquid mixture is simply dispensed over the template. The silicone can be quite viscous, so the substrate may have to be tilted to facilitate spreading. The PDMS is then cured by applying heat. Required curing time depends on the temperature, ranging from more than 24 hours at 40°C to about 15 min at 140° C [60]. Curing of the prepolymer into solid state PDMS leads to volume shrinkage with respect to the mould, due to buildup of internal stresses [61]. Higher curing temperatures lead to increased shrinkage of the PDMS (3 vol% at 140° C), and thus a more mechanically stiff replica. Finally, the PDMS is simply pealed off the template with a pair of tweezers. The resulting replica can be bonded to glass to make it more rigid or to seal off the surface when fabricating microchannels. Bonding of PDMS to glass is done by exposing both surfaces to oxygen plasma. This treatment forms silanol surface groups by replacing the methyl groups (CH_3) of PDMS with hydroxyl groups (OH). Placing both surfaces in conformal contact leads to covalent Si−O−Si bonds after loss of a water molecule [62]. This bond is stronger than the inter-chain bonding strength of the PDMS, leaving the two surfaces practically inseparable.

To reduce adhesion and thus make separation of the cured PDMS from the mould possible, the surface energy of the template is often reduced by applying hydrophobic self-assembled monolayers (SAM). SAMs are functionalized, long-chain organic molecules that forms spontaneously on surfaces through chemisorption and self-organization [22]. Most of the SAMs are thiols with an -SH end group, which binds to substrates such as gold (Au), silver (Ag), copper (Cu) or palladium (Pd). One such molecule is the fluoroorganothiol based SAM 1H,1H,2H,2H-perfluorodecanethiol (F_8H_2SH), which is reported to have a water

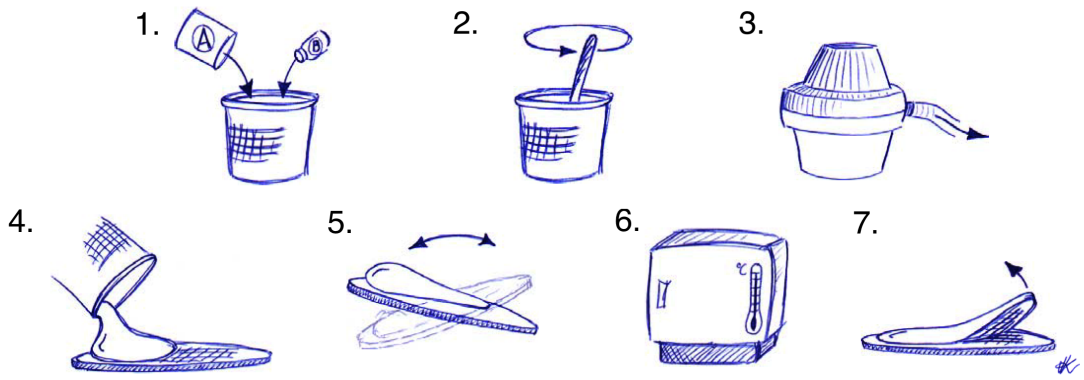

Figure 2.13: Process steps in replica moulding of a template, using PDMS. Adapted from [60]

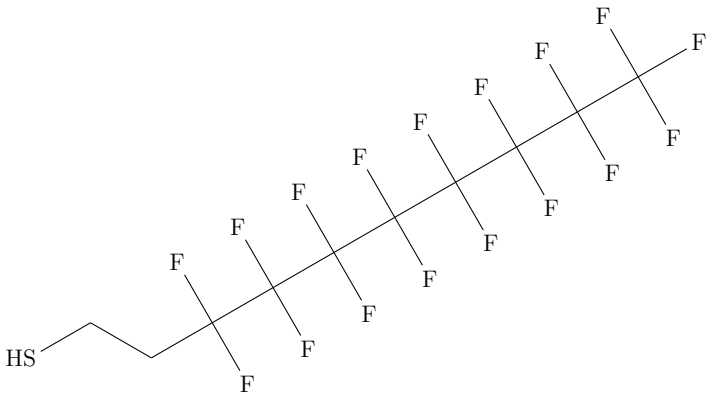

Figure 2.14: Structure formula of perfluordecanethiol

contact angle of 116 ± 3° [63]. The structure formula of F_8H_2SH is shown in figure 2.14.

2.7 Scanning electron microscopy

Scanning electron microscopy (SEM) is a widely used instrument in nearly all branches of science and engineering [41]. As the name implies, it uses electrons to form an image of the sample. The microscope provide the observer with images that closely resembles how our brain perceives the three dimensions of the real world. The basic setup of the SEM is illustrated in figure 2.15. Electrons are generated from an electron gun, either by applying heat or a high voltage, and accelerated in an electric field. The strength of the electric field determines the kinetic energy of the electrons hitting the sample. Magnetic coils placed down the beam column focus the electrons into a beam, analogous to the focusing of light in an optical microscope. The big difference is however that while light is focused by refraction, electrons are focused by the force they experience

in the presence of a magnetic field, termed the Lorentz force [64]. The force component is perpendicular to the direction of velocity and the magnetic field, so the electrons are drawn closer to the beam axis. The electrons are focused through an aperture and hit the sample as a small beam spot. Magnetic scanning coils are placed further down the beam column to move the beam spot over the surface in a scanning motion.

Electrons scatter when they hit the sample atoms, both elastically and inelastically (with energy loss). It is the signal from the inelastic scattering, that produce secondary electrons, which is the most widely used imaging mode. In addition, scattering produce high-energy backscattered electrons, X-rays and auger electrons, which are used to obtain information about the chemical composition of the samples. Secondary electrons are, as the name implies, new electrons generated by the inelastic interactions from incident electrons. They have a low energy (<50 eV), and thus they originate within a few nanometers from the surface [65]. The secondary electrons are collected by a scintillator-photomultiplier detector system, which use an electric field to attract the low-energy electrons. The brightness of the signal depends on the number of electrons reaching the detector. Electrons hitting steep surfaces or edges will have a shorter escape distance than others, as illustrated in figure 2.16. Thus, these areas will appear bright and gives the three-dimensional appearance of the SEM images.

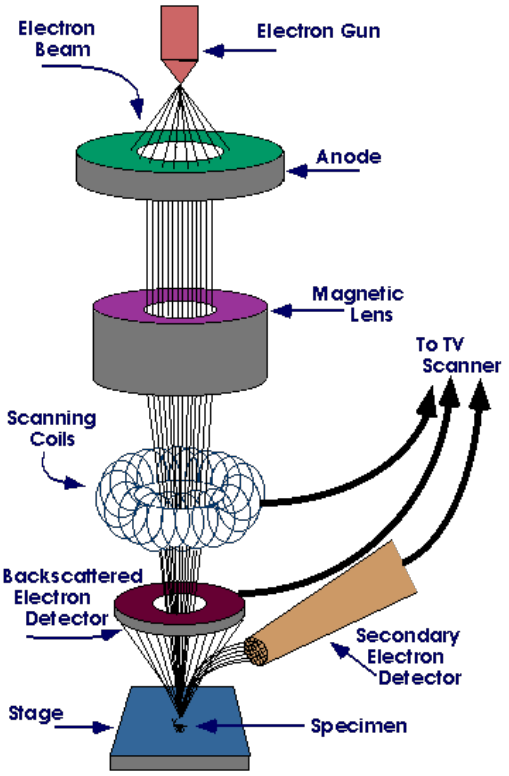

Figure 2.15: Schematic of the scanning electron microscope setup[2]

Backscattered electrons are electrons with high energy that scatters back towards the incident beam, and originates from a larger sample volume than the secondary electrons (down to about 1 μm). The detector is often placed inside the beam column. The intensity of backscattering depends on the atomic

[2]http://www.purdue.edu/rem/rs/sem.htm

weight of the sample atoms. Heavier atoms lead to more backscattering than light atoms. Thus, the backscattered signal gives contrast from different atomic elements in the sample. The elemental composition of the sample can also be obtained quantitatively through the detection of characteristic X-rays, excited by the electrons interacting with sample electrons. The X-ray signal can be analyzed either by its intensity as a function of energy (energy-dispersive spectroscopy (EDS)), or as a function of their wavelength (wavelength-dispersive spectroscopy (WDS)).

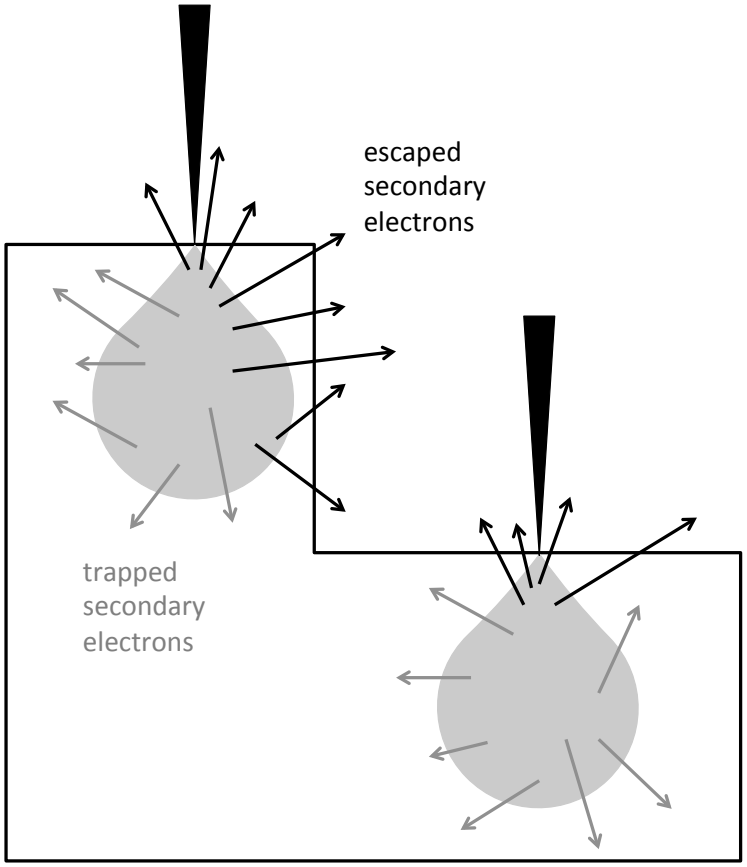

Figure 2.16: Secondary electrons are generated by inelastic scattering of the electron beam within a balloon-shaped volume in the sample. Only the electrons generated close to the surface are able to escape. When the electron beams hits features with a sharp edge, a large signal is collected since many electrons are generated closer to the surface. Thus, edges and peaks on the surface appear brighter than other features, which gives samples a three-dimensional appearance.

Chapter 3

Materials and methods

Contents

In this section, a detailed description of the experimental procedures will be given. Figure 3.1 is a simplified schematic of the fabrication process of the final PDMS surface. First, roughness is produced on the Cu surface by etching, oxidation, electrodeposition or a combination. Then, the liquid photoresist SU-8 is spun on the Cu surface and exposed. The device is left in a copper etchant until all Cu has completely dissolved. By photolithography, pillars of SU-8 are fabricated on top of the negative SU-8 replica. Finally, a positive PDMS replica is made by replica moulding of the SU-8 stamp. An overview of how most of the samples are fabricated is presented in table 3.1.

3.1 Copper processing

Different kinds of copper processing methods were tested to examine the effect on roughness; copper etching with or without using SU-8 as an etching mask, oxidation, electrodeposition or a combination.

For copper etching, a solution was made by using a mixture of copper(II) chloride dihydrate ($CuCl_2 \cdot 2\,H_2O$ from Merck Chemicals), 37 % hydrochloric acid (HCl from Sigma-Aldrich) and de-ionized water, with an approximate wt%

ratio of 20, 20 and 60 of the constituents respectively. In initial experiments, 30x30x0.8 mm polycrystalline copper plates (Polymetaal, The Netherlands) were etched with the same etching solution, so that the concentration of the different chemical compounds changed during its use. After the etching of a few samples, the solution changed colour from green to dark green or dark brown. The solution was regenerated by adding HCl and H_2O_2 until the initial green colour was obtained.

The etching process was standardized by moving from using an etchant solution with unknown concentrations, to one with known concentrations, each sample was etched with 20 mL of fresh solution containing 20 wt% HCl, 20 wt% $CuCl_2$ and 60 wt% DI-water. After etching was terminated, the solution was treated as waste. Later, the effect on the roughness using different concentrations of HCl and $CuCl_2 \cdot 2\,H_2O$, and the effect of etching time, ranging from 1 minute to 2 hours, were examined. For the samples to be able to fit onto the AFM sample holder, the copper plates were cut into smaller pieces with dimensions of 7x7 mm. The copper plates used for SU-8 and PDMS processing were also standardized to be 20x20x0.8 mm, so that the replicas would fit onto a standard microscope glass slide. After etching, the samples were rinsed with DI-water and dried with a N_2 pressure gun. To remove the insoluble layer of CuCl on the surface, all samples were cleaned in 37 % HCl for 6 minutes in an ultrasonic bath. The samples were then rinsed with DI-water again and dried.

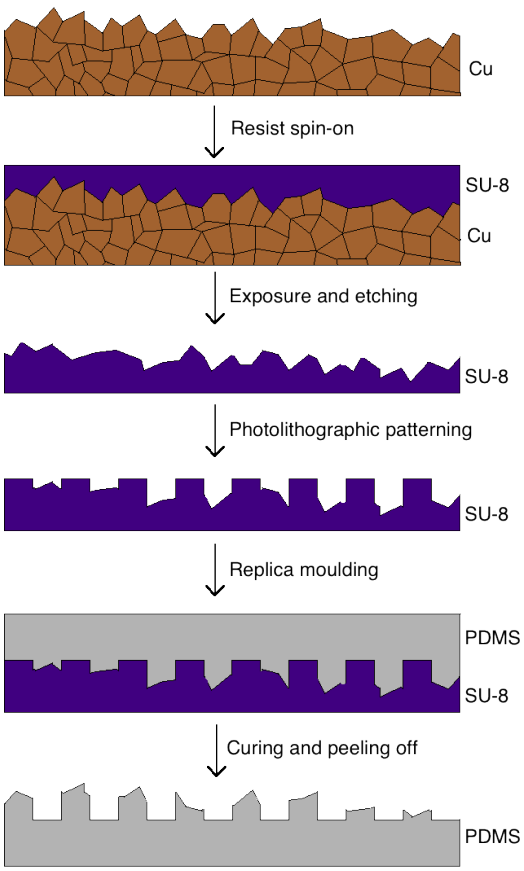

Figure 3.1: Simplified schematic of the fabrication procedure of making PDMS surfaces with patterned wettability through replica moulding with copper and SU-8.

A different type of roughness were made by oxidizing etched copper surfaces in a convection oven at 500° C. Oxidation times ranged from 10 to 30 minutes.

After oxidation, the copper plates were cooled in air. The cooling rate was controlled by placing a glass lid immediately over the sample.

Electrodeposition was performed by using a copper plate, etched or unetched, as the cathode, and a thin copper foil as the anode. Both electrodes were immersed in a solution of 228 g L^{-1} (1,4 M) $CuSO_4$ and 21 g L^{-1} (0,2 M) H_2SO_4. A constant voltage of 12,5 V were used deposit copper and produce hydrogen bubbles at the cathode surface. After electrodeposition, the plates were rinsed with DI-water and dried with pressurized air.

3.2 SU-8 processing

For photolithographic patterning, the negative photoresist Nano^{TM} SU-8 2, SU-8 5 and SU-8 2100 from MicroChem Corp [66] was used, with a glass-transition temperature, T_g, of 55° C. The resist consists of three components; an epoxy called EPON SU-8 (from Shell Chemical), a solvent, which is either cyclopentanone (for SU-8 2100) or gamma butyrolactate (for SU-8 2 and SU-8 5), and a photoacid generator (triaryl sulfonium salt) [67]. It has a maximum absorption of light with wavelength of 365 nm. The viscosity of SU-8 2 and SU-8 5 is 45 and 290 cSt respectively. When applied by spin-coating, the difference in viscosity gives different final resist thickness. SU-8 2100 has a viscosity of 45000 cSt and was used to produce resist layers with a final thickness of $100 - 250$ μm. For resists with required thickness $2 - 15$ μm, SU-8 2 and SU-8 5 was used, while for intermediate thickness requirements, a solution of SU-8 2100 thinned by an amount of 1/4 was used, which gives a final thickness of about 60 μm when spun at 1000 rpm.

For replication of the processed copper surfaces, a thick and mechanically stable layer of SU-8 was required. Thus, SU-8 2100 was used for this purpose. The resist was applied to the copper substrate by spin-coating for 60 s, using a final speed of 1000 rpm and a ramping speed of 100 rpm/s. A final thickness of approximately 250 μm was achieved according to the standard process guidelines given by the fabricant [66]. To improve wetting of the rough copper surfaces of SU-8, the resist was degassed in a desiccator after resist spin-on, to remove any trapped air bubbles. For degassing, the sample was moved to another lab. Because the resist will cross-link when exposed to UV-light, the desiccator was carefully covered with aluminium foil while under transport, since the room lighting emit some radiation with wavelengths in the UV-range.

The soft bake was performed on a hot plate in two temperature steps; first

at 65° C for 5 minutes, then for at least 60 minutes of 95° C. The two-step baking process was recommended in the standard process guidelines to reduce mechanical strain in the resist. To produce a replica moulded surface in SU-8, the resist were flood exposed for 120 seconds without any mask, to ensure that cross-linking occurred throughout the whole film. Exposure was carried out using a MJB3 Manual Mask Alginer from SUSS MicroTec, which used a mercury arc lamp to emit UV light with an intensity peak at a 365 nm wavelength (i-line), which coincides with the absorption peak of the SU-8 photoresist. Finally, the film was baked after exposure (post-exposure bake) in two steps: 5 minutes at 65° C and 6 0 minutes at 95° C. To reveal the SU-8 replica surface, the copper substrates were then added to a 250 ml etchant solution, as described earlier, to dissolve the copper adhering to the SU-8. After all the copper was dissolved in the etchant, a process that lasted from about 12 hours to several days depending on the degree of agitation, the SU-8 replica could be obtained from the solution with a pair of tweezers. SU-8 was then glued onto a regular microscope glass slide with a two-component epoxy compound, with the replicated surface facing up, to improve the mechanical stability necessary for PDMS replication.

To make flat regions in the PDMS replicas, SU-8 pillars were fabricated on either the copper templates or the SU-8 negative replicas. The depth of the wells were kept as shallow as possible, to demonstrate that the water capturing effect arose from the wetting behaviour and not as a consequence of the pattern geometries. In addition, it was assumed that water would not wet deep PDMS wells due to its intrinsic properties. Experiments were also performed to replace PDMS wells in favour of PDMS pillars in the final replicas. This pattern required a negative mask, so that the whole surface was exposed except where the wells in SU-8 would be positioned. Finally a mask giving 25 μm square pillars separated by 75 μm were used to fabricate an SU-8 etch mask for enhanced micro-scale roughness of the copper templates. Both a conventional photolithography mask with opaque chromium deposited on quartz glass, and a PDMS mask with a chromium pattern was used (developed in collaboration with fellow master student Kai Beckwith). The advantage with using a PDMS mask was conformal contact between the mask and resist to reduce reflections during exposure.

To reduce adhesion between SU-8 and PDMS, the surface energy of the SU-8 had to be lowered. This was achieved by first sputter coating the cured SU-8 with a 5 nm layer of gold, followed by incubation in a 1 mM solution of perfluorodecanethiol in ethanol for 15 min. After incubation, the surface was

cleaned with 96 % ethanol for 15 min. The low surface energy was verified by depositing a small water droplet and observing a large contact angle.

3.3 PDMS replication

For replication, Sylgard® 184 Silicone Elastomer Kit, a two part PDMS from Dow Corning Corp., was used. The base and curing agent compound were mixed in a 10:1 wt% ratio. Curing of PDMS was performed at different temperatures in an convection oven, ranging from 22° C to 120° C, to examine the effect on surface roughness. To standardize the fabrication process and ensure reproducibility, a 3 mm deep mould being able to fit a standard microscope glass slide, was machined in polymethyl methacrylate (PMMA). After degassing the prepolymer, the SU-8 template was laid in the mould with the negative replica side facing upwards, and the mixture poured over until it had completely filled the mould (see figure A.6).

To covalently bind PDMS to a glass slide, the surface of the glass and the flat backside of the PDMS was treated with oxygen plasma for 12 seconds, using a power of 50 W in a 50 % oxygen environment with the Femto plasma cleaner from Diener electronic, before bringing the two surfaces in conformal contact and placing them in a convection-oven for 15 minutes at 80° C.

3.4 Profilometer characterization

The samples were characterized with a Veeco Dektak 150 profilometer, located in NTNU Nanolab. The profilometer was used to characterize the large-scale roughness of etched copper templates, as well as the height, width and thickness of the resist layers on the copper substrates. The radius of curvature of the stylus radius tip is 12.5 μm. A load force equal to 3 mg was applied to the substrate while scanning. The line scans were plotted in Matlab to quantify the surface topography.

3.5 AFM characterization

Measurements of the surface roughness of etched copper plates were performed with a Veeco Instruments Inc. MultiMode™ AFM, placed on a vibration-damped table. The AFM was operated using the NanoScope Software Version 5. All samples were scanned in tapping mode with tube scanners, using E-scanner for small

Table 3.1: An overview of some of the fabricated samples. Samples replicated with both SU-8 and PDMS are positive replicas (similar to copper template), while those replicated without using SU-8 as an intermediate step are negative replicas (inverted surface from template).
* Samples etched with unknown concentrations of etchants
** Samples etched with a 5 wt% $CuCl_2$ and 5 wt% HCl solution
*** Samples etched using an SU-8 etching mask

Name	Etched	Oxidized	Electro-deposited	Patterned	Replica	Figure
Stamp 2	1 min*	✗	✗	✗	✗	
Stamp 3	5 min*	✗	✗	✗	✗	
Stamp 4	30 min*	✗	✗	✗	✗	
Stamp 5	10 min*	✗	✗	✓	PDMS	4.2, 4.18
Stamp 6	20 min*	✗	✗	✗	PDMS	
Stamp 7	30 min*	✗	✗	✗	SU-8	4.8
Stamp 9	30 min*	15 min	✗	✗	SU-8 → PDMS	4.6a, 4.10a
Stamp 11	30 min*	30 min	✗	✗	SU-8 → PDMS	4.5, 4.6b, 4.10b, 4.15
Stamp 13	90 min*	30 min	✗	✗	SU-8 → PDMS	
Stamp 14	120 min	✗	✗	✗	PDMS	
Stamp 15	30 min	✗	✗	✗	✗	
Cu_2	✗	✗	✓	✗	SU-8 → PDMS	
Cu_3	30 min	✗	✓	✗	SU-8 → PDMS	
Cu_4	✗	10 min	✓	✗	SU-8 → PDMS	
Cu_5	15 min**	✗	✓	✓	SU-8 → PDMS	
Cu_6	15 min**	✗	✓	✓	SU-8 → PDMS	
Cu_7	15 min**	✗	✓	✓	SU-8 → PDMS	
Cu_8	30 min***	✗	✗	✓	SU-8 → PDMS	
Cu_9	30 min	✗	✓	✓	SU-8 → PDMS	4.7, 4.11a, 4.16
Cu_10	10 min*	✗	✗	✓	PDMS	4.19, A.8, A.9
Cu_11	30 min*	✗	✗	✗	✗	
Cu_16	30 min*	✗	✗	✓	PDMS	4.14, 4.20, 4.20
Cu_17	60 min *	✗	✗	✓	PDMS	4.9
Cu_18	60 min*	✗	✗	✓	PDMS	

scan areas (lateral range 10x10 μm and vertical range 2.5 μm) and J-scanner for large scan areas (lateral range 125x125 μm and vertical range 5 μm). The surfaces were probed with Nanosensors ^{TM} PointProbe $^{®}$ Plus rectangular silicon cantilevers (dimensions 4x30x125 μm, spring konstant $k = 42$ N m^{-1}) designed for tapping mode AFM. The tip radius of curvature, which limits the lateral resolution of the measurements, is guaranteed to be less than 10 nm from the producer [68]. Line scan rates of 0.5 Hz for were used for small-area scans,while larger scan areas required a scan rate of 0.25 Hz. Surface maps were created by collecting 512 line profiles, with 512 measurement points along each line, producing 512x512 pixel images.

Raw measurement data were further treated using the Gwyddion Software Version 2.22 [69] on a Mac OS X Version 10.6.7 platform. All images were software corrected for "scars", an error in the Z-directional movement of the piezo-scanner, which leads to sharp edges in the image. The samples were also corrected for tilt and curvature, to center the mean line of the line profiles around zero. After error corrections, the surfaces were analysed according to the parameters discussed in section 2.2. These parameters were then plotted in Matlab for comparison of different samples.

3.6 SEM characterization

Electron microscopy characterization of the surfaces was performed with a Hitachi TM3000 tabletop microscope, located in NTNU Nanolab. Images were acquired using an acceleration voltage of 15 kV. Samples were glued on sample holders with carbon tape. To obtain qualitative information of the surface roughness, a tilt of 24° was used, as this gives a three-dimensional appearance (see section 2.7). For the experiments using patterned SU-8 square pillars as an etching mask, a tilt close to 90° was used to examine the etching process of copper pillars. For copper-samples, no pre-treatment were necessary. PDMS and SU-8 are however non-conductive and were sputter coated with a 5-10 nm thick layer of gold prior to characterization to reduce charging.

3.7 Contact angle measurement

Contact angle between de-ionized water and the fabricated PDMS surfaces were characterized using the sessile drop method and a KSV Instruments CAM 200 contact-angle meter, located at the Department of Chemical Engineering. Im-

ages of static droplets deposited on the surface from a low height were captured by a CCD camera, and the contact angle evaluated in the CAM2008 computer software using sphere fitting. Five measurements were made for each sample.

3.8 Testing of droplet capturing ability

Different methods were used to test the ability to trap water droplets at the patterned regions. One method involved spraying a mist of de-ionized water at the sample, from a distance of about 20 cm and tilting the sample to an angle close to 90° to facilitate the roll-off of water droplets hitting the rough regions. Another method involved immersing the PDMS slabs in water, then slowly bringing it out and place it in an optical microscope, to observe whether water was captured in the fabricated wells or not. The same experiment was also performed with pouring over ethanol to lower the surface tension, before immersing the sample in water. This was done in order to wet the PDMS wells, as they readily trapped small pockets of air. A third method used, involved "washing" the samples with water from a wash bottle, bringing the sample to a tilt of about 45°. Then, the samples were inspected by a reflective optical microscope to determine whether water was captured or not.

Chapter 4

Results

Contents

In this chapter, the main results obtained during the project are presented. The first section presents the fabrication of rough copper templates using the different methods of etching, oxidation, electrodeposition or a combination. This is followed by a section on the replica moulding and photolithography processing of SU-8, and a section presenting the replica moulding of the final PDMS surfaces. Finally, the results from the wetting behaviour and testing of the water-capturing functionality are shown. Additional results, such as raw data, examples of how the data have been analysed and additional information that is of less importance, but may be of interest, are presented in the appendix at the end of this report.

4.1 Fabrication of copper templates

4.1.1 Copper etching

Table 4.1: Calculated values of the average roughness R_a, the root mean square roughness R_q, the skewness Sk and kurtosis K of polycrystalline copper plates etched with different etching times. The table shows the average value μ and standard deviation σ of the measurements for each parameter. The raw data was obtained by using a profilometer with a scan length of 500 μm.

	R_a [nm]		R_q [nm]		Sk		K	
Etching time	μ	σ	μ	σ	μ	σ	μ	σ
1 min	168	29	208	30	0.269	0.213	2.78	0.58
5 min	785	112	977	133	-0.099	0.288	2.83	0.27
10 min	1055	100	1336	139	-0.255	0.273	3.09	0.30
20 min	1412	231	1817	289	0.592	0.495	3.49	1.02
30 min	1883	407	2385	554	0.442	0.287	3.05	0.53
60 min	1900	564	2392	689	0.348	0.447	3.17	0.63

Initial etching experiments were carried out on 30x30 mm polycrystalline copper plates, with varying etching times ranging from 1 to 60 minutes. The change in surface roughness could be observed by simply observing the appearance of the copper through visual inspection. Unetched and polished copper was very reflective, while the etched copper scattered much of the incident light, looking similar to a fine sand paper. Another initial indication that etching produced a high surface roughness, was the wetting behaviour of water on the templates. When small water droplets were deposited on the copper substrates,they quickly spread out to wet the surface completely. Also, when the copper substrates were rinsed with water after etching, it took a while to dry the surface by using a pressurized N_2 gun, since water that was displaced to the edges of the substrate, readily wetted the surface again after the pressure was turned off. Since copper is hydrophilic, the large increase in hydrophilicity from a smooth surface suggested that a high amount of surface roughness was produced.

The roughness was characterized with a profilometer, and raw data from these measurements were used to calculate the average values and standard deviation of the roughness parameters discussed in section 2.2.1. The results are summarized in table 4.1. For the average roughness R_a and root mean square roughness R_q, the trend is clear: It increase consistently with increasing etching time. However, the standard deviation and thus the uncertainty also increase. It appears that the surface roughness could have been saturated after

30 minutes, as the increase in roughness when moving from 30 minutes to 60 minutes is well within a standard deviation.

The trend is not so clear for the skewness; it is negative when etching for 5 and 10 minutes, while it is positive in all other instances. As discussed in the theory section, a positive skewness means that the surface height distributions are slightly shifted toward negative z-values, which again means that there are slightly more peaks than valleys at the surfaces. All values are very close to zero within one standard deviation. Due to the relatively large standard deviation, there are considerable uncertainty in the average values.

The kurtosis seem to increase with increasing amount of etching until about 20 minutes, then it drops to values around 3, characteristic of a Gaussian surface, which most engineering surfaces follows. Following the theoretical discussion on kurtosis, the samples with a high kurtosis have a relatively high number of sharp peaks, compared to the samples with low kurtosis.

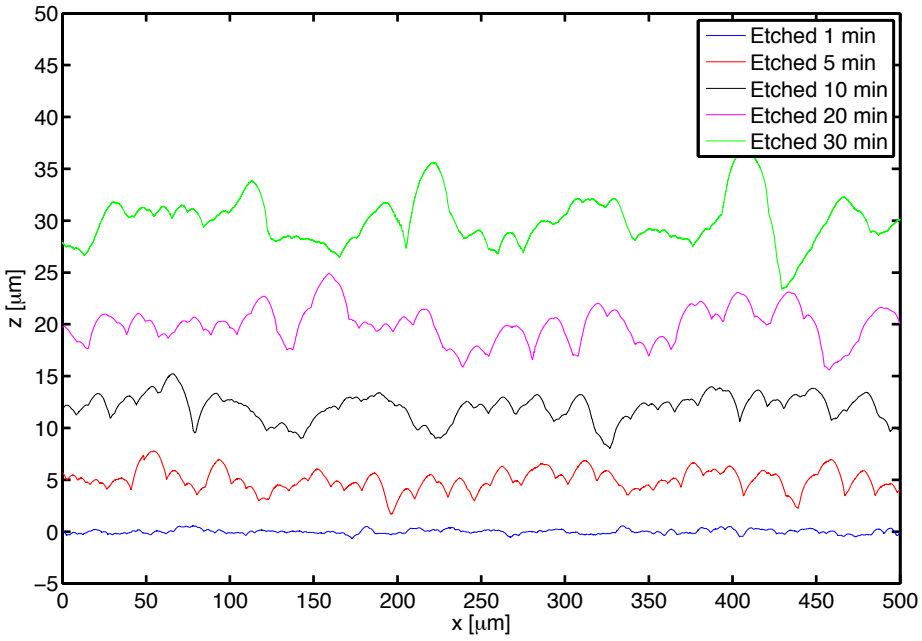

Figure 4.1: Representative line profiles for different etching times plotted in Matlab. The profiles are drawn to scale and offset at the vertical axis for graphical representation. The diagram shows increasing roughness with increased etching time.

To illustrate the increase of surface roughness with increasing etching time, some characteristic line profiles for the different samples have been plotted in figure 4.1. The profiles are drawn to scale and offset at the vertical axis for a better graphical representation. One could qualitatively see that the peaks and valleys become increasingly higher and deeper, and that the maximum and minimum values from the mean line of the line profiles increase with increasing

etching time.

To complement the roughness measurements of the profilometer with qualitative information about the surface texture, the samples were examined with a scanning electron microscope (SEM). Figure 4.2 shows roughness on both the micro-scale (a) and the nano-scale (b) for a copper surface etched for 10 minutes (stamp 5). The etching reveals the grain structures of copper, textures with steep and sharp edges. Roughness is superimposed on the grain structures, showing a step-like appearance. Very few "smooth" features can be found in the image.

4.1.1.1 Effect on etchant concentration

To examine the roughness quantitatively with AFM, it was decided to standardize the etching procedure and use a known concentration of the different etchant compounds. Therefore, a new procedure with using a fresh solution of the copper etchant for each sample was commenced. The new experiments started by using a solution containing 20 wt % $CuCl_2$ and 20 wt % HCl. Several samples were etched with different wt % ratios of the two chemicals, and characterized by performing 100x100 μm AFM surface scans in tapping mode. From these measurements, the height distribution and autocorrelation function were calculated and plotted in figure 4.3a and figure 4.3b respectively.

From figure 4.3a, it could be seen that the samples etched with a low concentration of HCl and $CuCl_2$ (red and blue curve) have the broadest height distribution (highest value of the standard deviation σ). Increasing the amount of HCl from 10 wt % to 30 wt % seem to decrease σ, leading to sharper peaks. The effect of increasing the amount of $CuCl_2$ is not so clear from the plot however. For instance, σ is higher when etching with 10 wt% than 20 wt%, keeping the amount of HCl constant, but lower when etching with 30 wt%, which is the most narrow distribution of all the samples.

The normalized autocorrelation functions shows that most of the samples in figure 4.3b have an exponential decay. The two samples with the lowest concentration of HCl and $CuCl_2$ have the highest value of the autocorrelation length β^*, the distance where the autocorrelation function falls to 10 % of its initial value. It is difficult to see any trends when increasing the concentration of HCl from 10 wt% to 30 wt%, keeping the amount of $CuCl_2$ constant at 20 wt%. The value of β^* is decreased when going from 10 wt% to 20 wt%, but is increased again from 20 wt% to 30 wt%. Increasing the amount of $CuCl_2$ from 10 wt% to 20 wt%, keeping the amount of HCl constant at 20 wt%, decreases

(a)

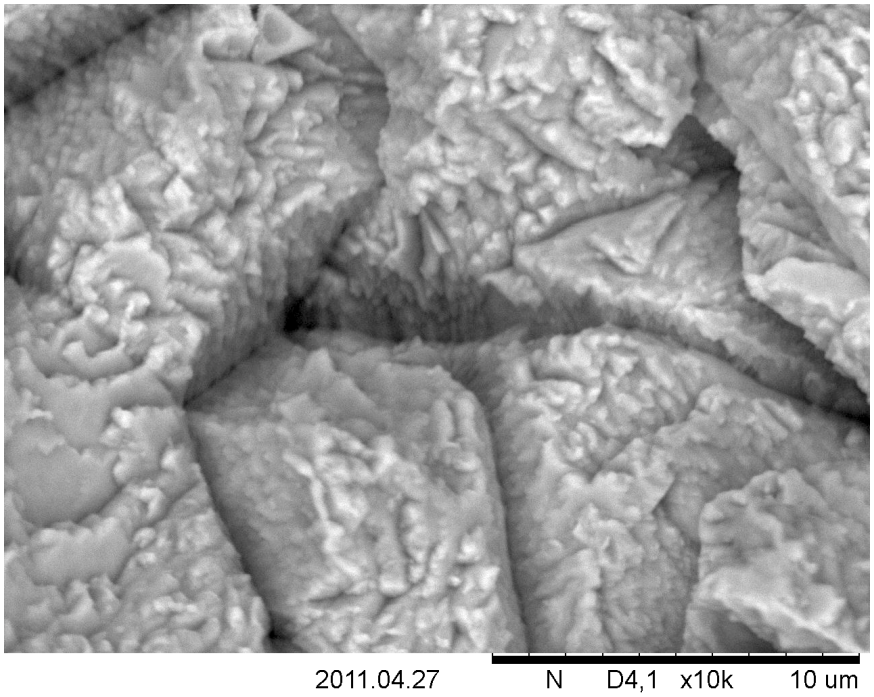

(b)

Figure 4.2: Stamp 5: Polycrystalline Cu plate etched for 10 minutes. Images obtained by SEM using a 15kV acceleration voltage.

β^* from 6.0 μm to 4.8 μm. The value is then further decreased to 3.5 μm when increasing the concentration from 20 wt% to 30 wt%.

Table 4.2: Calculated values of the average roughness R_a, the root mean square roughness R_q, the skewness Sk and kurtosis K of polycrystalline copper plates etched with different concentration of HCl. The presented values are averages of 512 AFM line scans, using a scan length of 100 μm.

HCl [wt %]	$CuCl_2$ [wt %]	R_a [nm]	R_q [nm]	Sk	K
10	20	130	167	0.192	0.61
20	20	100	126	-0.020	0.43
30	20	89	112	0.428	0.27

Table 4.2 shows the same roughness parameters as in table 4.1, only for samples etched with a various amount of HCl. The roughness parameters are averages of 512 AFM line scans for each sample. It can be seen that both R_a and R_q decrease with increasing amount of HCl. This is also true for the kurtosis. There is no clear correlation between the concentration and skewness.

Table 4.3 shows similar parameters, only that the concentration of $CuCl_2$ was changed instead. For these measurements, both R_a and R_q decrease with increasing concentration of $CuCl_2$, similar to what happened when increasing the amount of HCl. A result worth mentioning is that two different samples presented in the two former tables, etched with the same concentration (20 wt % HCl and 20 wt % $CuCl_2$), have different roughness parameters. This shows that there are some uncertainties from sample to sample, when etching is carried out under the same conditions.

Table 4.3: Calculated values of the average roughness R_a, the root mean square roughness R_q, the skewness Sk and kurtosis K of polycrystalline copper plates etched with different concentration of $CuCl_2$. The presented values are averages of 512 AFM line scans, using a scan length of 100 μm.

HCl [wt %]	$CuCl_2$ [wt %]	R_a [nm]	R_q [nm]	Sk	K
20	10	135	174	0.729	1.24
20	20	80	102	0.248	0.496
20	30	61	77	0.341	0.941

Table 4.4 shows the roughness parameters when using lower amounts of HCl and $CuCl_2$. R_a and R_q are higher for these samples than for samples presented in the two former tables. The same trend can also be seen here; the roughness and kurtosis decrease with increasing concentration of etchant.

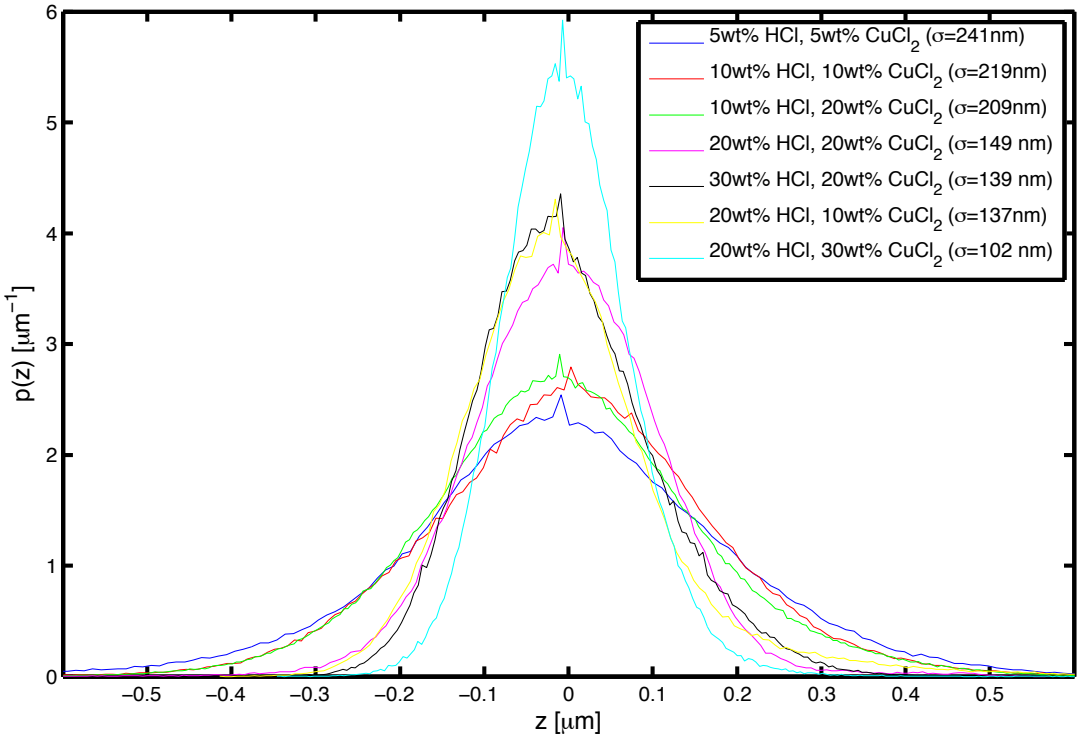

(a) Normalized height distribution

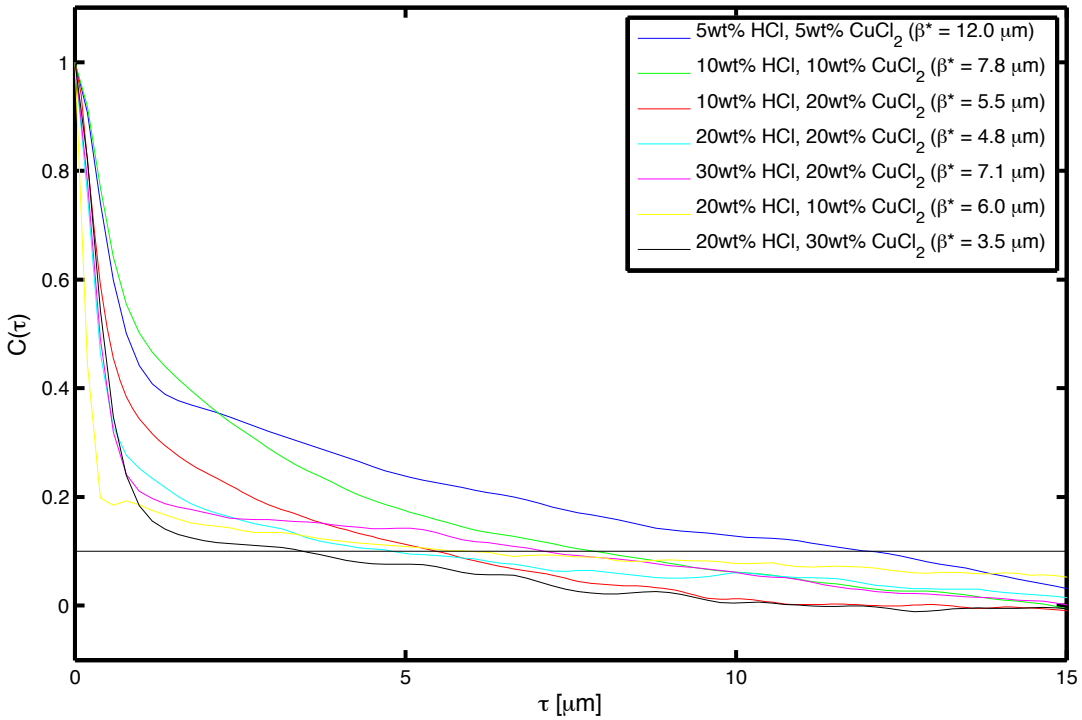

(b) Normalized autocorrelation function

Figure 4.3: The normalized height distributions and autocorrelation functions plotted for copper plates etched for 15 min with varying concentration of HCl and $CuCl_2$. The data was obtained from 100x100 μm AFM scans. The standard deviation σ of the height distribution for different samples were calculated by fitting to a Gaussian function. The correlation length β^* of the samples were obtained by calculating the intersect with the 10% decay value (black horizontal line).

Table 4.4: Calculated values of the average roughness R_a, the root mean square roughness R_q, the skewness Sk and kurtosis K of polycrystalline copper plates etched with low concentrations of HCl and $CuCl_2$. The presented values are averages of 512 AFM line scans, using a scan length of 100 μm.

HCl [wt %]	$CuCl_2$ [wt %]	R_a [nm]	R_q [nm]	Sk	K
5	5	153	201	-0.173	1.24
10	10	131	169	-0.015	0.69

4.1.1.2 Effect on etching time

Table 4.5: Calculated values of the average roughness R_a, the root mean square roughness R_q, the skewness Sk and kurtosis K of polycrystalline copper plates etched with a different amount of time. The presented values are averages of 512 AFM line scans, using a scan length of 100 μm.

Time [min]	R_a [nm]	R_q [nm]	Sk	K
0	48	66	1.220	1.87
1	38	51	1.540	9.70
2	73	92	0.673	0.66
5	73	92	0.860	1.97
10	77	99	0.164	0.93
15	100	126	-0.020	0.43
30	60	77	0.454	0.85
60	79	105	0.776	2.21
120	84	106	0.409	0.53

Since the etch rate depends on the concentration of HCl and $CuCl_2$, the effect of etching time was examined in a similar way as in the previous section, holding the concentration of HCl and $CuCl_2$ constant at 20 wt%. The calculated height distribution is shown in figure 4.4a, for an unetched copper sample and samples etched from 1 minute to 120 minutes. The unetched copper surface have the most narrow distribution followed by the sample etched for 1 minute. The width is almost the same for the samples etched for 2, 5, 10 and 60 minutes, although the two former have a distribution shifted towards negative z-values (positive skew). The samples etched for 15 and 120 minutes have the two highest values of σ, which means that these distributions are the broadest.

The calculated autocorrelation functions are shown in figure 4.4b. The results are difficult interpret, as there are no apparent correlation between the etching time and the correlation length β^*. The shortest correlation length is found for

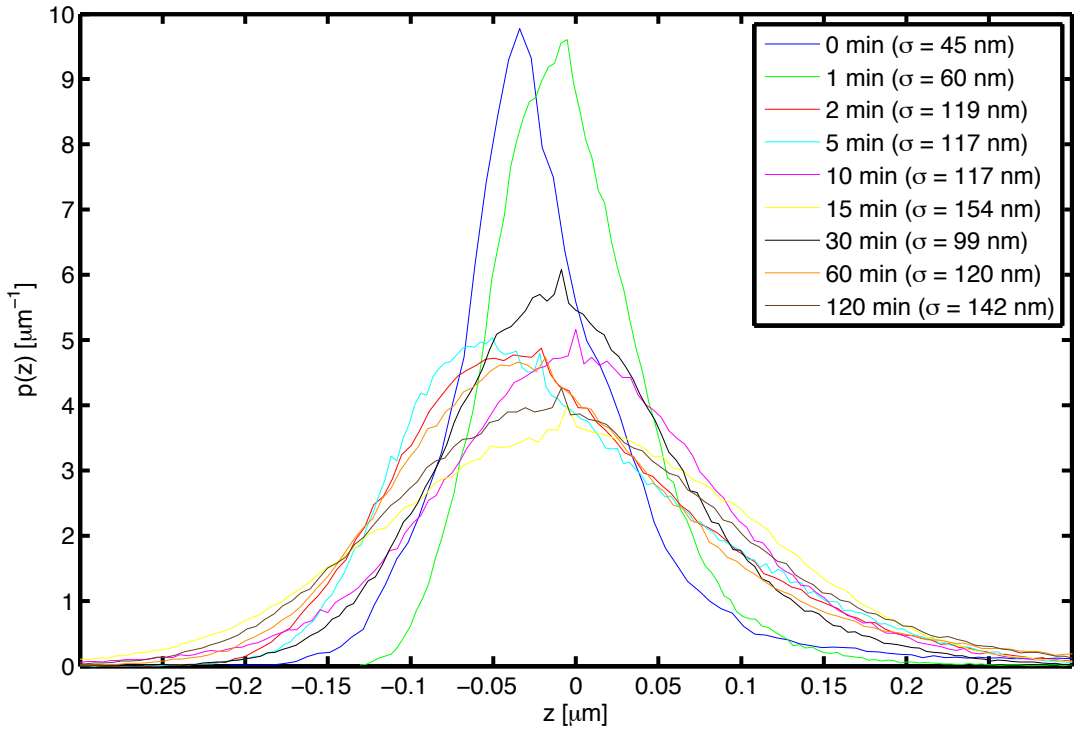

(a) Normalized height distribution

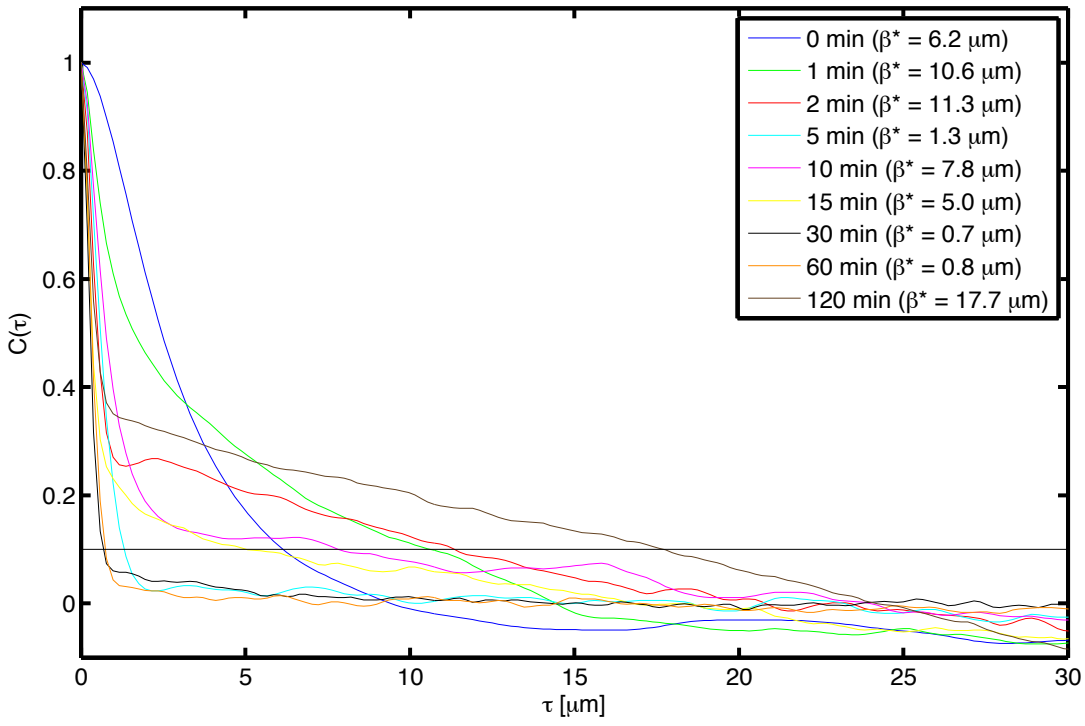

(b) Normalized autocorrelation function

Figure 4.4: The normalized autocorrelation function for Cu etched for different amount of time, using a solution of 20 wt % HCl and 20 wt % $CuCl_2$. The data was obtained from 100x100 μm AFM scans. The standard deviation σ of the height distribution for different samples were calculated by fitting to a Gaussian function. The correlation length β^* of the samples were obtained by calculating the intersect with the 10% decay value (black horizontal line).

the two samples etched for 30 and 60 minutes ($\beta^* = 0.7\ \mu$m and $\beta^* = 0.8\ \mu$m respectively). The highest correlation length is found for the sample etched for 120 minute ($\beta^* = 17.7\ \mu$m).

Table 4.5 shows the amplitude roughness parameters for the samples etched with different amount of time. The first sample have not been etched at all. It shows that there are some roughness present, although very low, even though the sample looks completely flat by visual inspection. Etching for only 1 minute lead to a very high kurtosis and a high positive skewness, while the roughness is slightly decreased from that of unetched copper. The roughness seems to increase up to a 15 minute etching time, where it is saturated, since longer etching times does not show any clear trends, and the variations are not significantly large. It is also difficult to see any correlation between etching for more than 2 minutes and the value of the skewness and kurtosis.

4.1.2 Copper oxidation

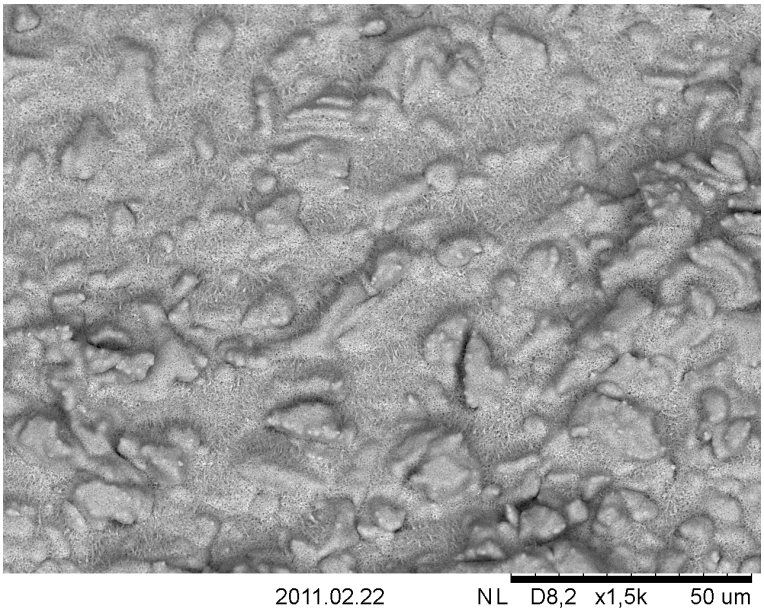

Figure 4.5: Microscale roughness of CuO after 30 minutes of oxidation.

Oxidation of etched copper plates was carried out by heating the samples at 500° C in a convection oven. Oxidizing for less than 10 minutes lead to the formation of a red Cu_2O surface layer. Further oxidation lead to the formation of a black surface layer of CuO. The CuO surface layer was fragile and easily flaked off, for instance when the samples were handled with tweezers. The flaking of the oxide layer became especially pronounced when the samples were oxidized

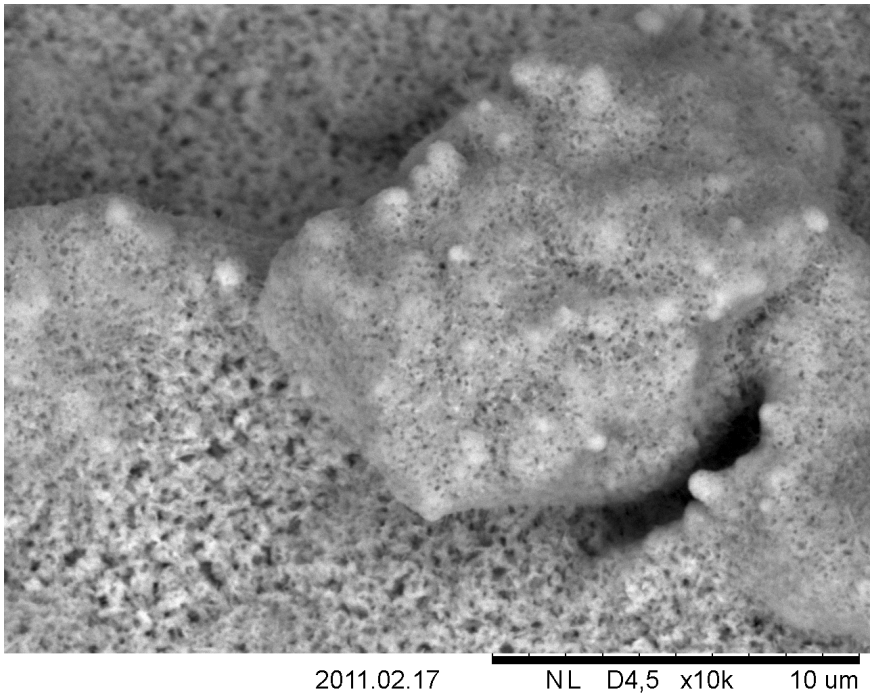

(a) Stamp 9: CuO after oxidation for 15 min at 500° C

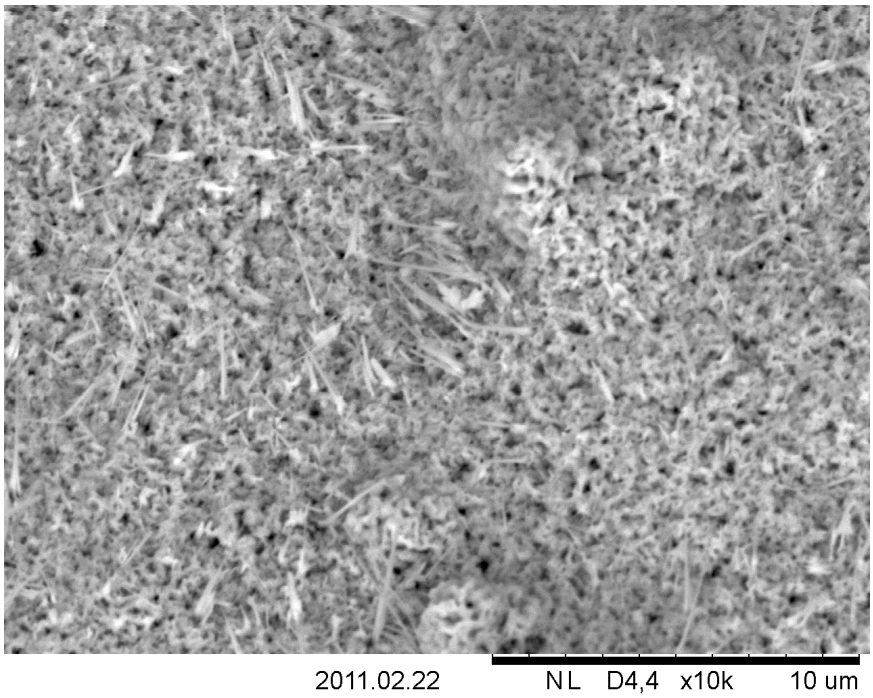

(b) Stamp 11: CuO after oxidation for 30 min at 500° C.

Figure 4.6: Stamp 9 and 11 were polycrystalline copper plates etched for 30 minutes before oxidized for 15 and 30 minutes respectively. Stamp 11 shows CuO nanowire growth, while this is not present in stamp 9. Images obtained by SEM using a 15kV acceleration voltage.

for a larger amount of time. The degree of flaking was difficult to control, but was minimized by handling the samples as carefully as possible.

Figure 4.5 shows the micro-roughness of a copper sample oxidized for 30 minutes. The porous CuO layer produce another type of surface roughness than the etched copper. It appears that the growth of the CuO surface layer leads to a lower micro-roughness relative to before oxidation. It appears that the growth of CuO are most pronounced in the valleys of the etched copper, as they are filled to a large degree. Only the highest asperities protrude through the oxide layer. The asperities are also oxidized and appear "softer" than before oxidation.

Figure 4.6 shows oxidized samples on a smaller length scale. The sample in a) were oxidized for 15 minutes, and shows the porosity of the oxide layer. In this image, the lower lying surface appears to be more porous with a higher surface roughness than the asperity surface. The sample shown in b) was oxidized for 30 minutes. A similar porosity as in a) can be seen. However, the longer oxidation time has lead to the growth of CuO nanowires with varying size, up to a few μm in length. From the image, they seem to grow outward perpendicular to the orientation of the nucleation point.

The surface roughness parameters of the CuO samples were not measured by AFM. Due to the problem of tip convolution discussed in section 2.3.2, the AFM would not be able to image high-aspect ratio structure such as the CuO nanowires. Thus, the change in surface roughness by introducing CuO nanowires can only be discussed qualitatively.

4.1.3 Copper electrodeposition

Figure 4.7 shows electrodeposited Cu on Cu pre-etched for 30 minutes. Because of the formation of hydrogen bubbles at the copper surface, the electrodeposition forms a porous network of connected sub-micrometer particles. Some of the structures look like vertical poles, where copper particles have been electrodeposited on top of each other, with smaller copper particles deposited on the sidewalls. From the image, it appears that the copper particles have a smooth surface, so that the surface have a low roughness on the smaller scale. Electrodeposition was also carried out on unetched copper plates, where the copper deposited preferably along edges, such as scars on the surface.

The electrodeposition was conducted at a constant voltage. After the power source was turned on while the cathode and anode was immersed in the electrolyte, the current quickly dropped to zero, due to the passivation of the copper

anode. The larger the surface area of the copper anode was, the longer the electrodeposition lasted.

As with the CuO surfaces, AFM was not used to measure the surface roughness quantitatively, due to the tip convolution as discussed earlier.

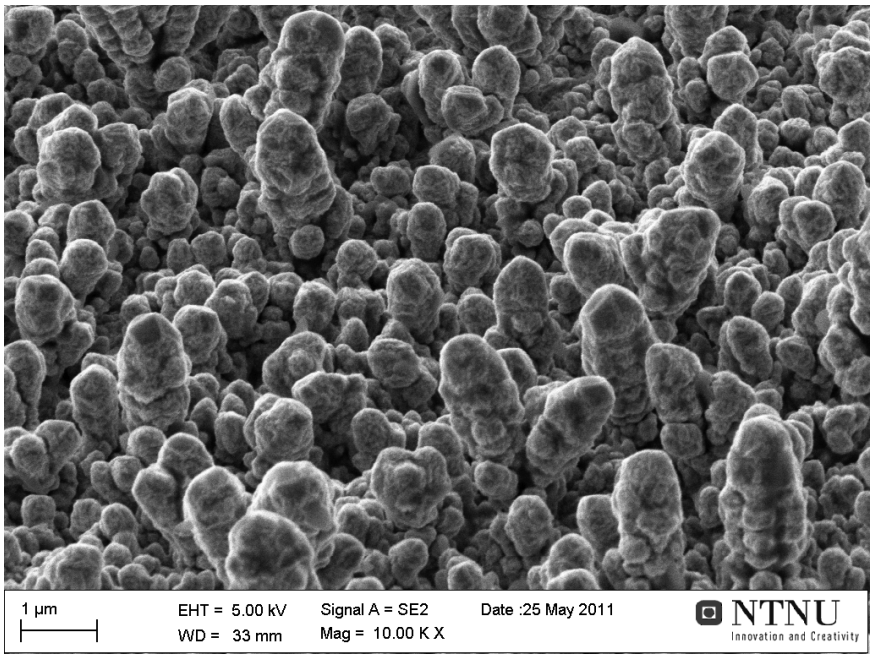

Figure 4.7: Electrodeposited Cu on pre-etched Cu surface. Because of the formation of hydrogen bubbles at the copper surface, the electrodeposited copper forms a porous network.

4.2 SU-8 processing

In this section, the results of the SU-8 replica moulding process of the rough copper surface will be presented, as well as the results from the photolithographic patterning of SU-8 on copper templates to define wells in PDMS replicas or to act as an etch mask for enhanced roughness of the copper substrates.

When applied on rough copper templates, it was noticed that the SU-8 did not wet the surface readily as water. This was especially true for the most viscous type of SU-8 (SU-8 2100), which was required to produce sufficient thickness for the replicated resist to be handled with tweezers after dissolving the copper template. Therefore, spreading of the resist over the copper surface was assisted by using a pair of cocktail sticks to smear out the SU-8 before spin-on. Due to the poor wetting, and the way the resist was deposited on the copper surface, air might have been trapped at the copper-resist interface. To reduce this problem, the samples made later on in the project were degassed using a desiccator after

spinning. After a few minutes, bubbles started to appear at the surface of the SU-8 film.

After the copper was dissolved in the etchant, the negative SU-8 replica was revealed. The time required to dissolve all the copper ranged from 12 hours to several days depending on the amount of agitation. The resulting SU-8 replicas had an initial thickness of about 250 μm. However, the SU-8 2100 photoresist became gradually more viscous during the project, resulting in an almost solidified resist at the end of the period, which meant that the final resist thickness of the replicas increased.

The thin SU-8 pieces were quite brittle, and in initial experiments, some of the replicas easily shattered into smaller pieces when handled with tweezers. To improve the mechanical stability, the SU-8 was initially glued onto a piece of a plastic Petri dish. Due to the high temperatures used in the soft and post-exposure baking steps (95° C), the plastic partially melted and deformed, which lead to a non-planar SU-8 replica surface. The SU-8 replicas were instead glued onto glass slides, which could tolerate the baking temperatures.

4.2.1 SU-8 replicas of etched copper

Figure 4.8 shows a piece of SU-8 2100, which is a negative replica of Cu etched for 30 minutes with the used solution (stamp 7). One can see structures following that shown in figure 4.2b, with an inverse grainy structure. However, some features especially in the middle lower part of the image appears to have a very low surface roughness.

Due to the fact that the maximum height difference between the lowest and highest feature was observed to be above 10 μm for the most rough copper templates, it was not possible to get an even resist surface by spin-on, without using the SU-8 2100 resist with thickness above 100 μm. It was observed that during soft-bake, some of the roughness were smoothened out due to polymer flow above the glass transition temperature of SU-8 ($T_g \sim 55°$ C).

A problem that occurred while replicating with SU-8, was wrinkling at the top surface, caused by internal stress in the SU-8 resist. This problem occurred during the post-exposure baking step, when the temperature reached about 45° C. Due to the high amount of stress, the unexposed SU-8 resist was mechanically deformed, which could be seen by visual inspection as small dots "popping" out from the resist surface. After development and etching of the copper, the SU-8 was examined by SEM, shown in figure 4.9. The significantly

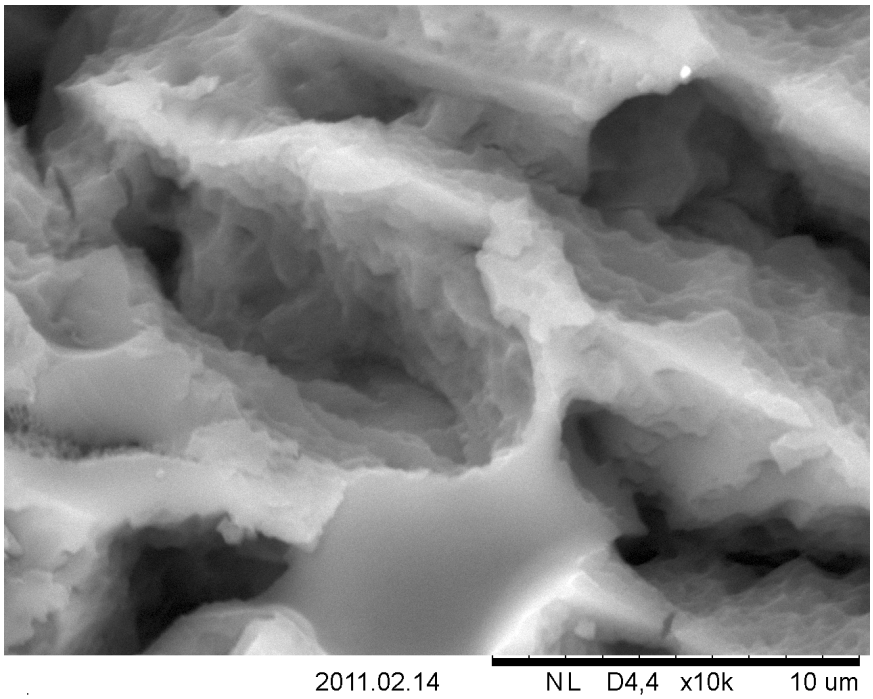

Figure 4.8: SU-8 negative replica of Cu etched for 30 minutes.

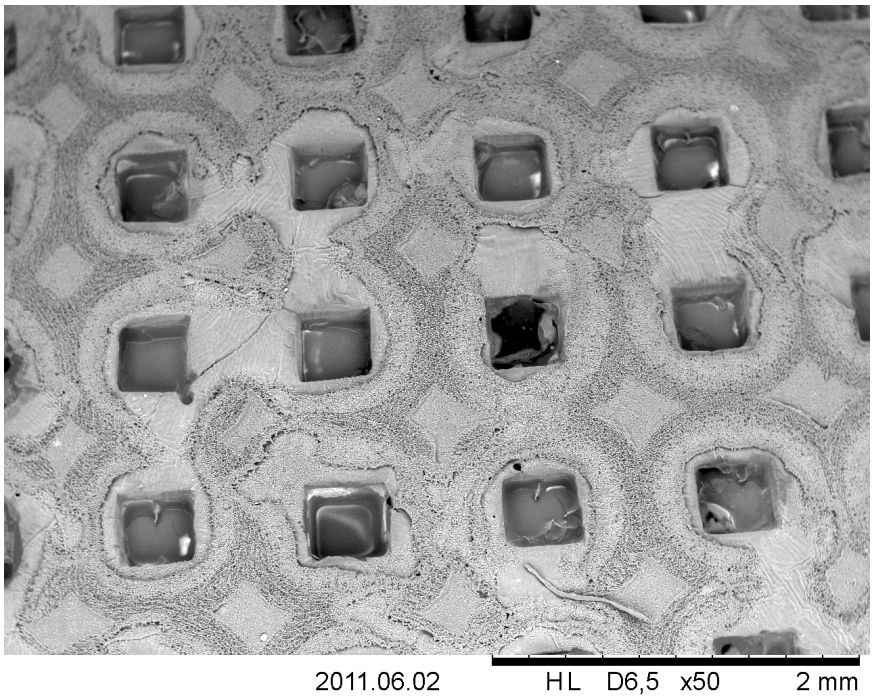

Figure 4.9: The SEM image shows the SU-8 replica from etched copper (Cu_17) with patterned wells. The image shows "rings" around the wells, where the surface roughness of SU-8 is significantly lower than the surrounding regions.

lower roughness around the patterned wells suggest that the internal stress cause the resist to detach from the rough copper surface. A similar effect is observed between the patterned wells, where the resist also may have detached.

4.2.2 SU-8 replicas of oxidized copper

As mentioned earlier, the CuO layer grown on the surface of metallic copper frequently flaked odd due to low adhesion. Since the most viscous type of SU-8 was used to replicate the CuO surface, it had to be spread over the surface mechanically. As the SU-8 was almost solidified, the lateral forces applied on the thin oxide layer caused it to flake off, destroying large parts of the template surface. Often, only small areas of the CuO was still intact after SU-8 was applied. Figure 4.10a and 4.10b shows SU-8 negative replicas of copper first etched and then oxidized for 15 and 30 minutes respectively. From the images, it appears that replicating Cu oxidized for 30 minutes leads to a higher small-scale roughness than the copper oxidized for 15 minutes. However, the large scale roughness is reduced relative to that of etched copper surfaces, as was also seen in figure 4.6. The Cu nanowires in figure 4.6b does not seem to have been replicated, although it would have been difficult to observe due to their small size and the fact that the surface polarity is inverted, which would have led to narrow, straight pores in the resist.

4.2.3 SU-8 replicas of electrodeposited copper

Figure 4.11 shows the SU-8 negative replica of electrodeposited Cu on Cu etched for 30 minutes. The surface structures on the two replicates surfaces are very different. The image in a) shows small dimples on the surface, resulting from the spherical shape of the electrodeposited Cu colloid particles. In b) however, the SU-8 have replicated parts of the porous network seen in figure 4.7, suggesting that the SU-8 is able to partially wet the copper surface and replicate high aspect-ratio structures. As seen in the latter image, the micro-scale roughness is increased. However, the replication of these kind of structrures was very inhomogeneous. In addition, there is a very low amount of nano-scale surface roughness on the replicated surfaces.

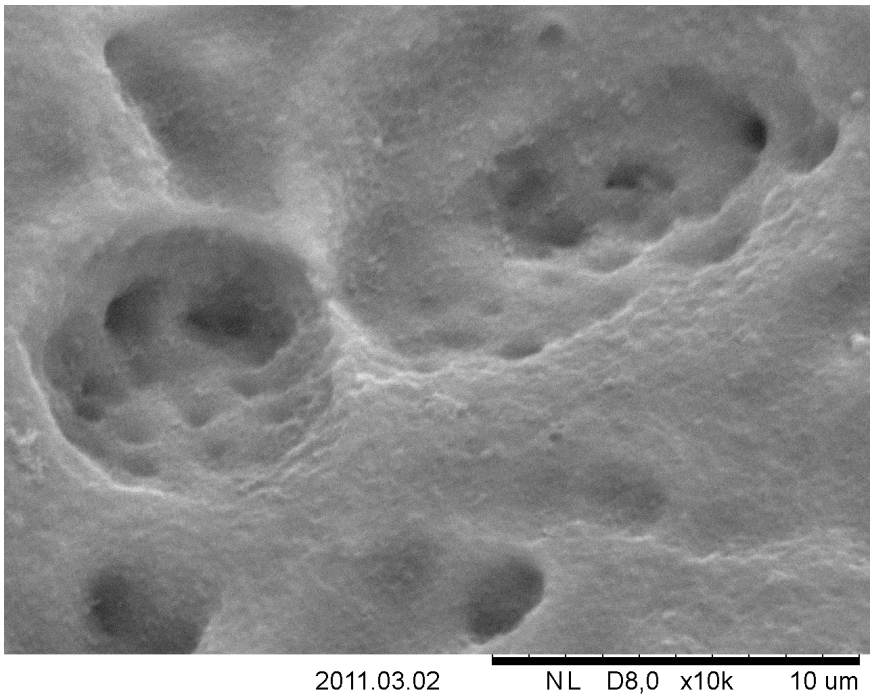

(a) SU-8 replica of CuO oxidized for 15 min (stamp 9)

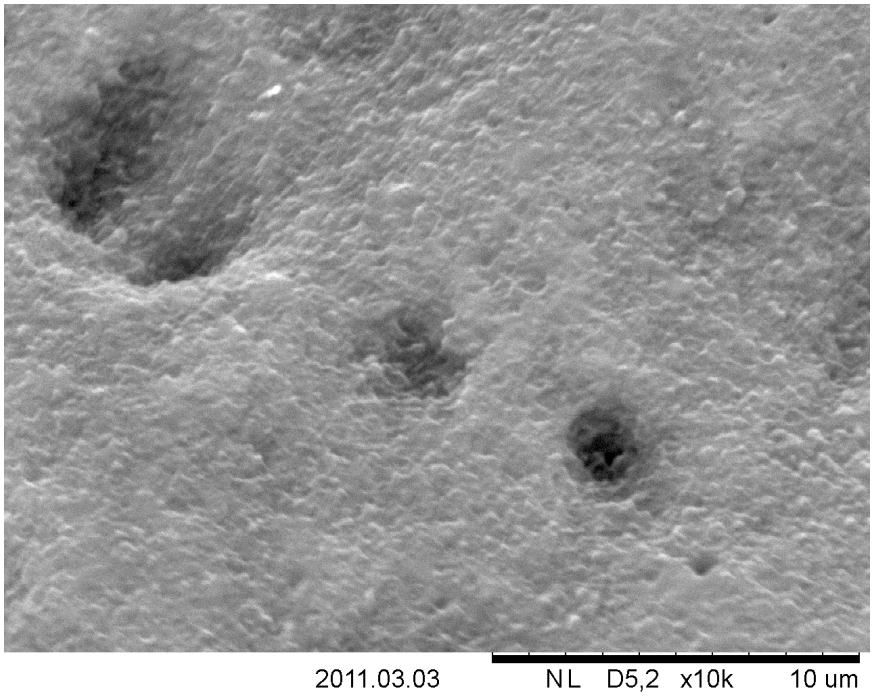

(b) SU-8 replica of CuO oxidized for 30 min (stamp 11)

Figure 4.10: SU-8 negative replicas of CuO oxidized for a) 15 min and b) 30min. Images obtained by SEM using a 15kV acceleration voltage.

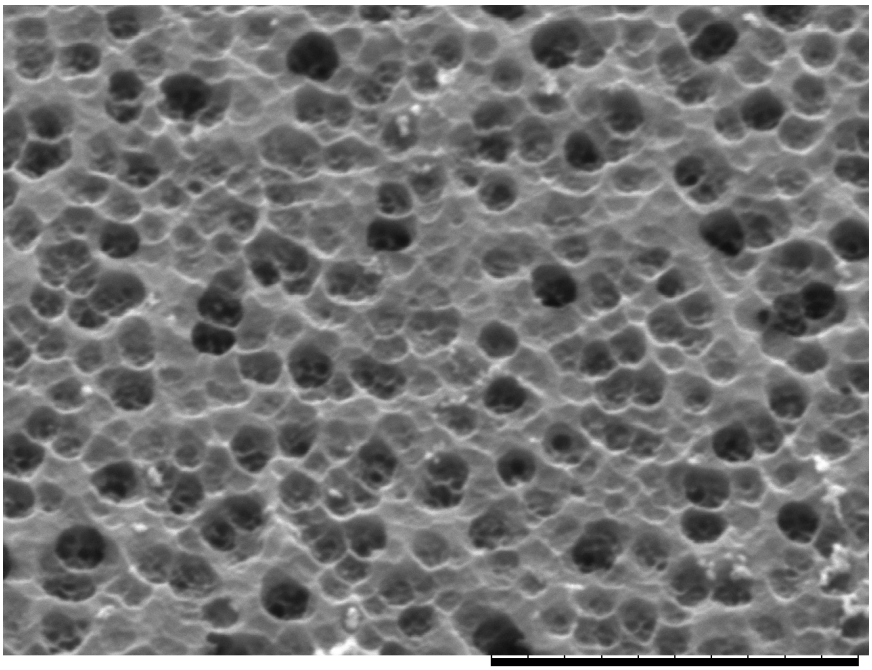

(a) Sample Cu_9

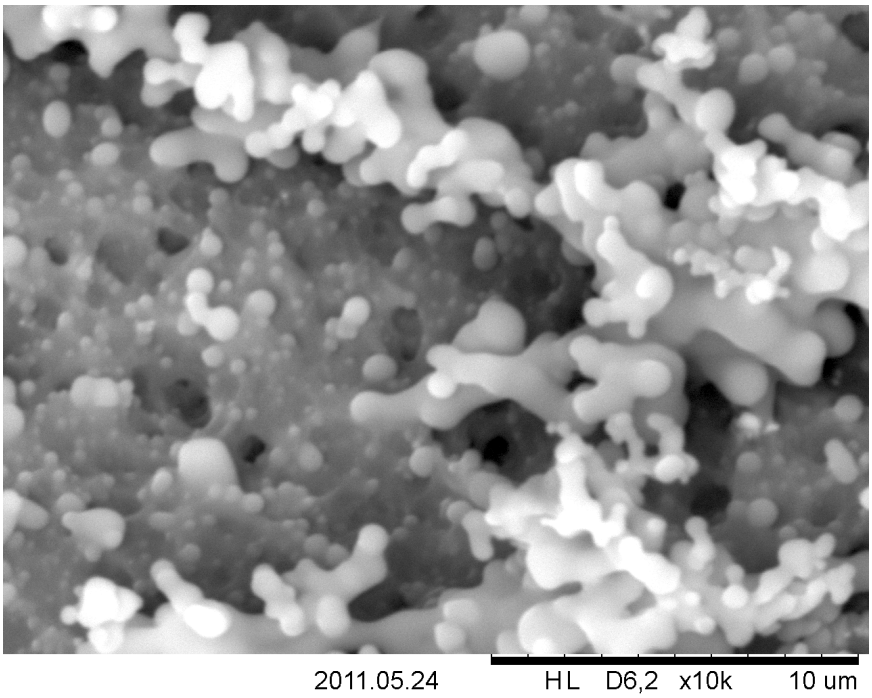

(b) Sample Cu_6

Figure 4.11: SU-8 negative replicas of electrodeposited copper on etched copper plates. In a) the inverse surface of the electrodeposited copper particles can be seen. In b), it can be seen that SU-8 resist flows into the porous network of the electrodeposited copper. The photoresist was degassed in a desiccator before soft baking.

4.2.4 SU-8 etching mask

Micro-roughness was in some experiments introduced by using photolithography to define an etch mask of SU-8. The masked areas were protected from the etchant, resulting in a height difference between the patterned and non-patterned regions. Initially, the resist started to flake off after 2 minutes of etching. To improve the adhesion between the SU-8 and Cu surface, the samples were therefore pre-etched for 2 minutes before applying the resist, to increase the interface area. This reduced the flaking, and etching times up to 8 minutes could be used with the majority of SU-8 pattern still intact on the surface. Figure 4.12 shows the resist and Cu surface after etching. The black dots are resist still remaining on the surface. It is possible to see the areas where the resist had flaked off, due to the height difference on the surface. Using ImageJ, the sidelengths of the squared SU-8 pillars were measured to be about 28 μm, while the inter-pillar distance was measured to be about 73 μm.

Figure 4.12b shows a near 90° tilted view of the etched Cu pillars. It also shows the under-etch below the resist, caused by the isotropic etching behaviour of the etchant (in an isotropic material, the etch rate is the same for all directions). The width of the two closest copper pillars was measured to be about 16 μm. The pillar height was quantified by a profilometer, shown in figure 4.13. The resist on the left pillar had recently broke off when the profilometer stylus ran into it during an earlier scan. The pillar height was measured to be 6.5 μm, while the right pillar, had a height of about 8.5 μm. This correlates well with the expected resist thickness of about 2 μm. Since the resist flaked off at different times, some pillars were exposed to the etchant more than others. Therefore, most of the etched Cu pillars are expected to have heights lower than the measured value.

4.3 PDMS replica moulding

The first replica moulding experiments with PDMS were carried out without lowering the surface energy of the copper samples. Due to this, it was impossible to separate the replica from the template without breaking the PDMS piece. By functionalizing the copper with perfluorodecanethiol, this problem was solved. One of the replicated PDMS surfaces are shown in figure A.7, bonded to a microscopic glass slide.

PDMS was initially cured at different temperatures, ranging from room tem-

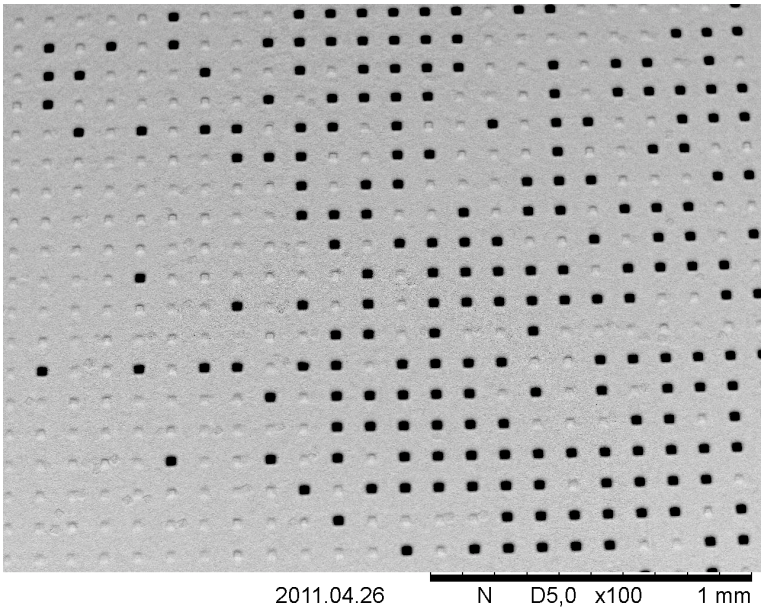

(a)

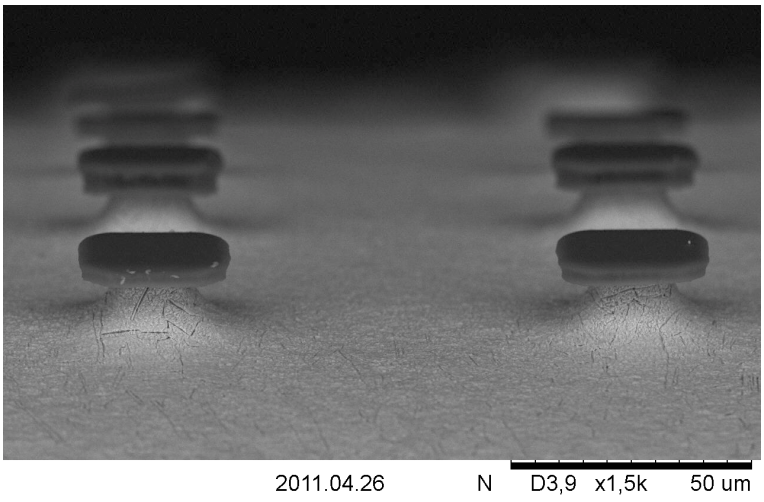

(b)

Figure 4.12: Cu surfaces with SU-8 patterned resist as etching mask. The surface was pre-etched for 2 min before patterning, then etched for 8 min afterwards. a) Some of the SU-8 pillars (dark spots) were removed due to the etching. b) Using a tilt near 90, the degree of under-etch is illustrated. Images obtained by SEM using a 15kV acceleration voltage.

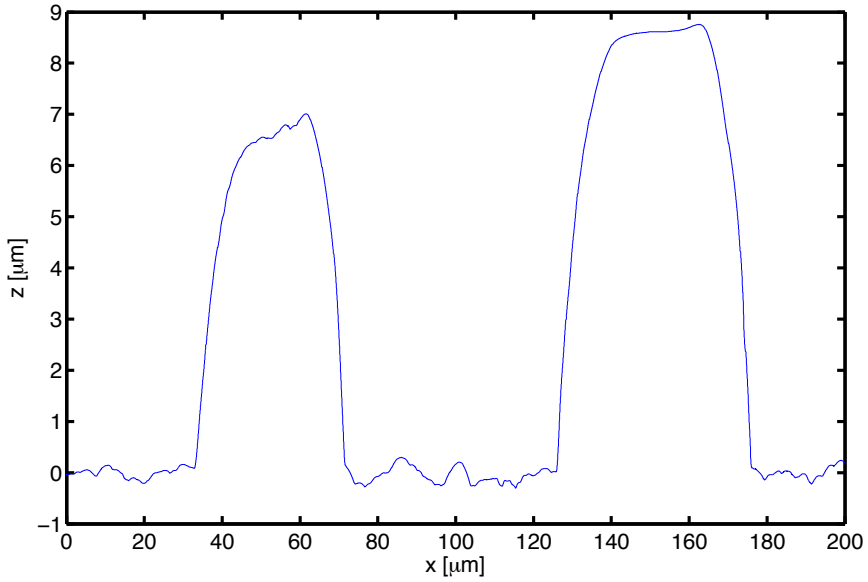

Figure 4.13: Profilometer scan of etched Cu pillars with and without SU-8 layer. The right pillar have a SU-8 layer remaninig after etching, while the SU-8 on the left pillar had just been removed when etching was stopped.

perature, requiring curing time of 2 days, to curing at 100° C, which only required 1 hour. Curing was also performed at 60° C and 80° C. The samples replicated at different temperatures, using the same template, were examined by AFM. PDMS is a quite "sticky" material, so imaging with the AFM tip lead to image artefacts. One of the most serious problems were the strong adhesion of the tip towards the surface, which lead to excessive tip contact and releasing problems during tapping mode. In addition, accumulation of PDMS on the tip lead to an increase in tip radius of curvature and the "double tip" effect, where the same features are imaged twice, both by the real tip and the material adhering to it. However, no real difference could be seen in the surface roughness for curing at different temperatures. The only observable effect was lower curing time and a lower elasticity of the PDMS samples when using high temperatures, as expected. Curing times between 60 and 80° C was chosen to save time, as well as to retain a certain elasticity, which would be beneficial when peeling of the replicas from the SU-8 templates.

It was observed that after replica moulding of the templates with SU-8 pillars, air bubbles were trapped at the pillar locations. These would lead to irregularly shaped wells in the PDMS, as the bubbles created an extra cavity. The problem was solved by placing the template in a desiccator after pouring over the prepolymer, but before curing.

A common problem encountered when imaging PDMS in the SEM was drift

of the samples, making it difficult to obtain good images at high resolutions. Drifting was partially caused by surface charging, since PDMS is non-conductive. Also, it is a soft material, so the surface features could be more sensitive to heating by the electron beam, than other types of samples. Charging was reduced by increasing the thickness of the sputtered gold layer from 5 to 10 nm.

4.3.1 Replica moulding of etched copper

Figure 4.14 shows the positive replica of Cu_16, which was etched for 30 minutes, similar to the template shown in figure 4.2. The surface texture show some similarities to that of the template, with the respect to the 'step-like' features and the grain structures. However, the PDMS seems to be more smooth, the edges are not so sharp as for the template structure.

4.3.2 Replica moulding of oxidized copper

Figure 4.15 shows a positive PDMS replica of a Cu sample oxidized for 30 minutes (stamp 11). It somehow resembles the texture of the template shown in figure 4.6b, where pores in the original CuO template have been replicated as dimples in PDMS. However, the high-aspect ratio structures such as the CuO nanowires are not present on the replica surface.

4.3.3 Replica moulding of electrodeposited copper

The surface roughness of the PDMS positive replica from electrodeposited copper (Cu_9) is shown in figure 4.16. Initially, it was challenging to get good replicates. For the first replicas, only small bumps were observed on the surface, so the total surface roughness was quite low. By increasing the time duration for the degassing of the prepolymer deposited on the SU-8 mold to 1 hour, and increasing the curing temperature from 80° C to 120° C, much better replicas were obtained. In figure 4.16, one can see a surface texture similar to that of electrodeposited copper. However, the roughness is lower than for the copper template, as only the very top layer of the copper particles are replicated, and not the underlying porous network.

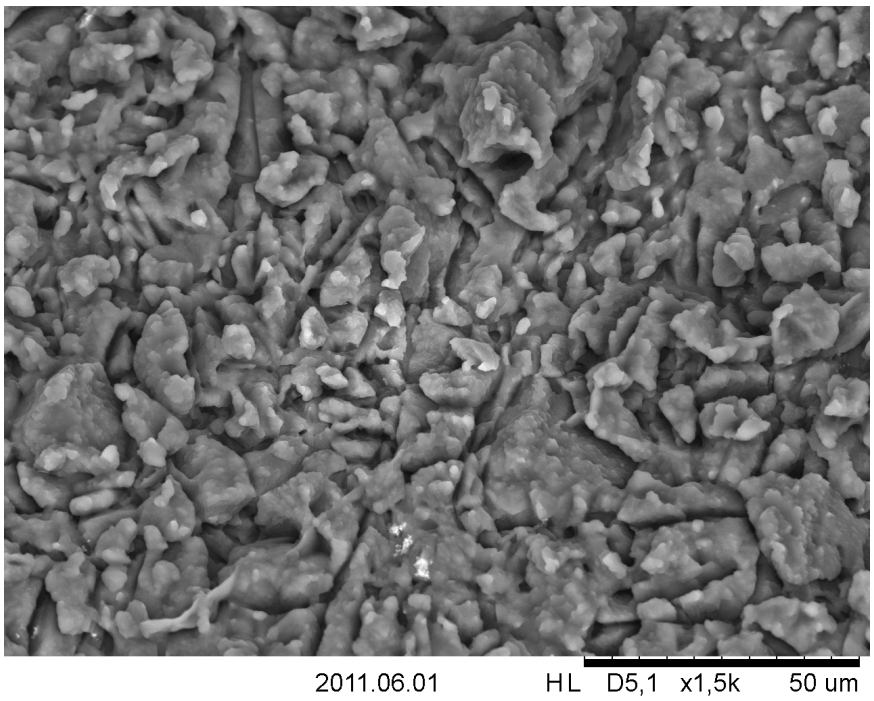

(a)

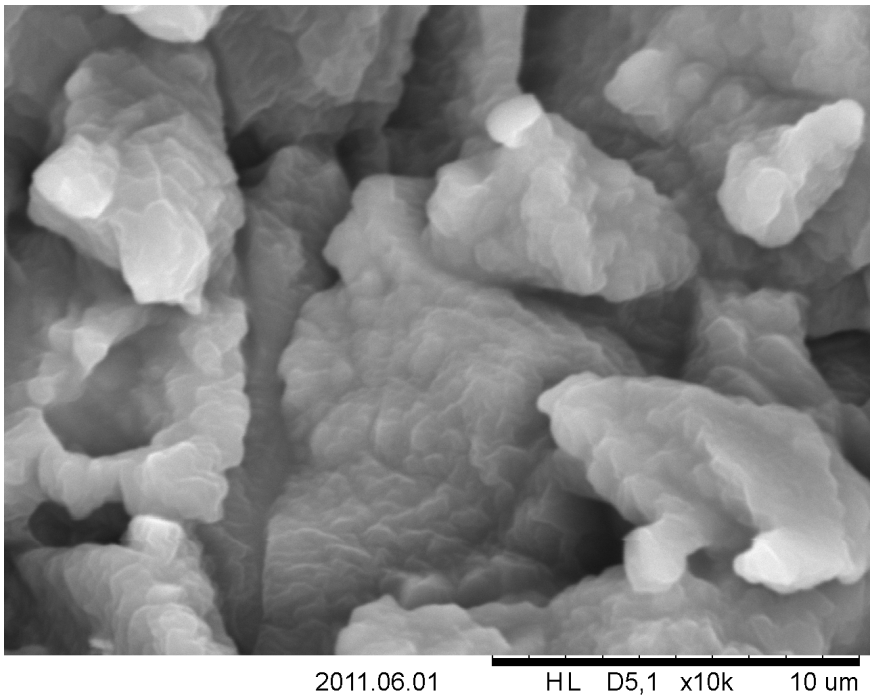

(b)

Figure 4.14: PDMS positive replica of an etched copper plate

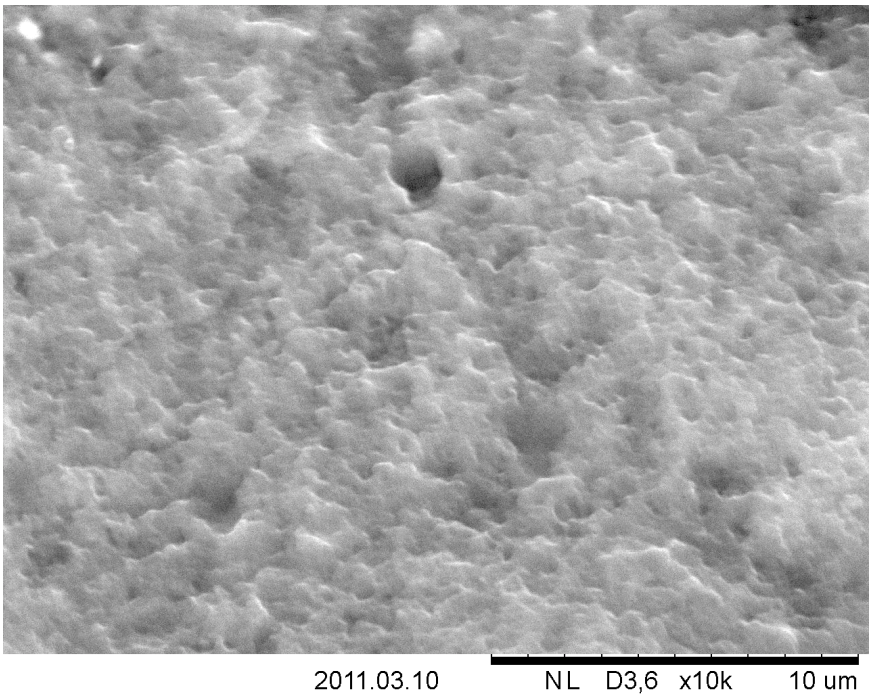

Figure 4.15: PDMS positive replica of Cu oxidized for 30 minutes

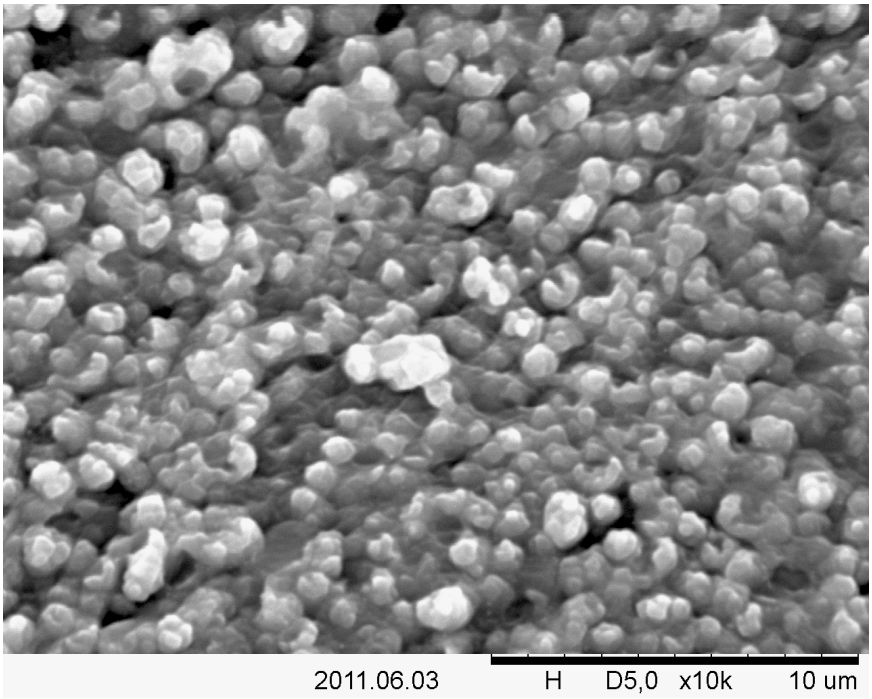

Figure 4.16: PDMS positive replica of electrodeposited copper on etched copper

4.4 Functionality of device

4.4.1 Contact angle measurements

Figure 4.17 shows a deposited droplet on a) flat PDMS with an average contact angle of 101.8 ± 3.4°, and b) the positive PDMS replica shown in figure 4.14, with an average contact angle of 154.7 ± 5.3°. The measured contact angle for the different samples are summarized in table 4.6, together with the roughness parameters from some of the corresponding copper templates. The results clearly shows that the contact angle is increased by introducing surface roughness, as expected from the theoretical discussion.

For the sample with the highest contact angle (Cu_16), droplets with a volume of 7 μ L carefully deposited on the surface were unstable and rolled off the surface when tilting the sample to an angle of about 30°. It was also observed that the droplets adhered more strongly to the pipette tip than the PDMS surface. For the samples with lower contact angle, the deposited water droplets tended to stick very well. Even when the samples were tilted to a high degree or turned upside down, the droplets didn't roll off the surface. The water repellency depended on the volume of the deposited droplets; droplets with a high volume tended to roll off more easily than droplets with a small volume.

(a) Flat PDMS surface (b) Rough PDMS surface (stamp 5)

Figure 4.17: Contact angle measurements shows an increase of the contact angle for flat PDMS (θ = 101.8 ± 3.4) to rough PDMS (θ = 154.7 ± 5.3), replicated from copper etched for 60 minutes (Cu_16). The droplets have a volume of 7.0 μL for all measurements

Table 4.6: Contact angle measurements of replicated PDMS surfaces and the measured roughness parameters from some of the copper templates.
* Etched with 20 wt % $CuCl_2$ and 20 wt % HCl

Nr.	Sample	$\theta[^\circ]$	R_q [nm]	Sk	K
1	Flat	101.8 ± 3.6			
2	Etched 10 min	150.6 ± 3.8	1336	-0.255	3.09
3	Etched 20 min	137.5 ± 5.4	1817	0.592	3.49
4	Etched 60 min	154.7 ± 5.3	2392	0.348	3.17
5	Etched 120 min*	134.3 ± 4.3	106	0.409	0.53
6	Etched 10 min + oxidized 15 min	103.8 ± 10.1			
7	Etched 90 min + oxidized 30 min	130.5 ± 7.6			
8	Electrodeposited	103.8 ± 1.8			
9	Etched 30 min* + electrodeposited	116.4 ± 5.1			
10	Oxidized 10 min + electrodeposited	122.2 ± 6.0			

4.4.2 Droplet capturing

Different methods were applied to test the water-capturing ability of the PDMS surfaces, as described in section 3.8. A superhydrophobic copper template with SU-8 pillars functionalized with perfluorodecanethiol, was used as a reference of the water capturing ability.

Spraying a mist of water on the copper template resulted in most of the water rolling off the surface, however the SU-8 pillars were covered with water droplets sticking to them, as shown in figure 4.18. There are also a few smaller droplets that sticks to the unpatterned regions.

The same experiment was also carried out for one of the SU-8 negative replicas (Cu_10) from etched copper. The SU-8 surface had been sputter coated with a 5 nm layer of gold, as well as incubated with perfluorodecanethiol to render it hydrophobic. Similar results were obtained for this sample as for the copper template, as shown in figure A.9.

The replica moulded PDMS surfaces tested with this method was not able to capture water as selectively as the two former examples. Spraying water once caused small droplets to deposit both in the rough and patterned areas. Spraying once more caused the smaller droplets to coalesce into larger ones. The size of the merged droplets tended to be larger than the size of the patterned areas. Thus, they often spanned between two or more holes and thereby wetted

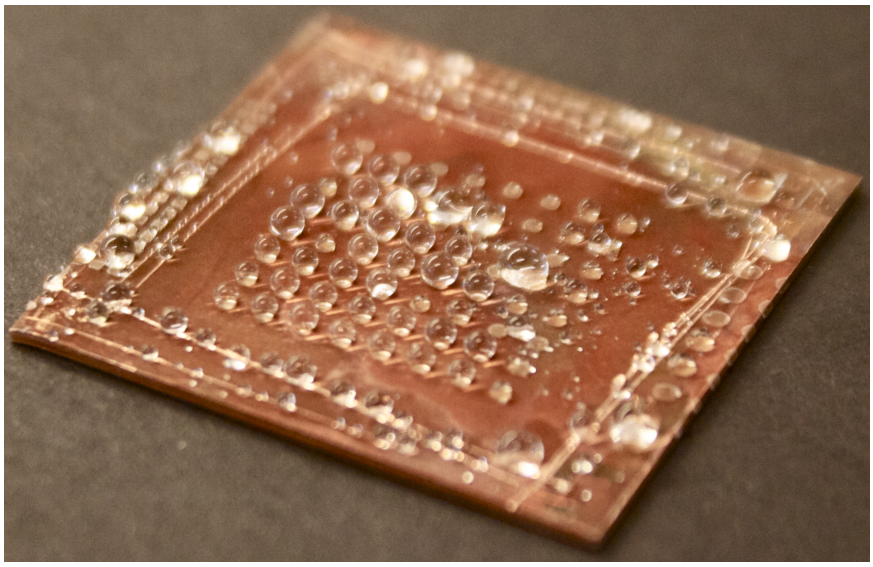

Figure 4.18: Photograph showing the capturing of water on an etched copper surface patterned with SU-8 pillars. Most of the droplets are sticking to the SU-8.

the rough areas in between. These experiments were performed several times without much selective water capturing.

The second method involved placing the surface upside down above evaporating water in a glass container. Through this method, very small droplets were condensed on the surface. As time passed, the small droplets grew and coalesced as more water condensed. On the copper template, the small droplets were deposited everywhere, and as they became bigger, they were randomly distributed independently of the surface pattern. Thus, this method was discarded as a suitable test method.

PDMS replicas were also immersed in water, and then slowly brought back out, to observe if water droplets attached to the flat wells and rolled off the rough regions. However, it was observed that while immersed under water, air bubbles were trapped in the PDMS wells. The wells were therefore not wetted by water using this method. To avoid trapping of air and facilitate wetting of the wells, ethanol was deposited on the surface immediately before immersion to lower the surface tension. As expected, the whole surface was wetted through this method. Unfortunately, rough regions were not de-wetted after pulling the PDMS sample out of the water. Thus, this method could not be used to capture droplets.

Another method involved dispensing water from a washing bottle, so that a water jet hit the surface, which was tilted to an angle of about 45°. The high angle was used to facilitate droplet roll-off at the hydrophobic regions. Figure 4.19

illustrates the water capturing before and after dispensing. Figure 4.19a taken before water is added, shows an empty PDMS well (sample Cu_10). The bright area shows a high reflective signal from the underlying glass slide, since PDMS is inherently transparent. In the surrounding areas, the roughness of PDMS cause scattering of incident light, even though it is transparent, and thus appear darker. Figure 4.19b taken after water dispensing, shows a completely wetted well.

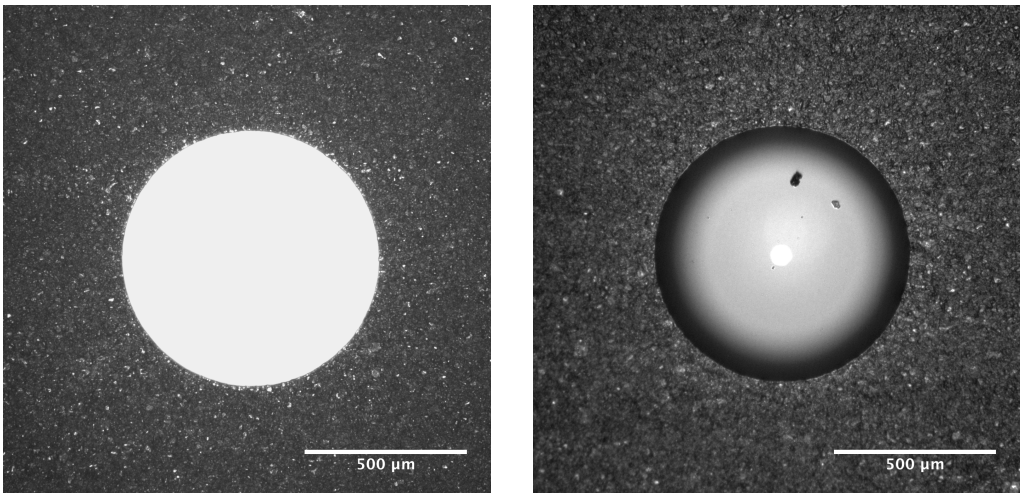

(a) PDMS well with no droplet (b) PDMS well with captured droplet

Figure 4.19: Capturing of water droplets demonstrated by observation through a reflective optical microscope (Sample Cu_10). In a), an empty PDMS well is imaged as the bright circle, while in b), a water droplet covers the PDMS well completely. The diameter of the wells were measured to be about 782 μm.

Not all the PDMS wells were wetted however. Some water droplets were bridging across two or more wells, and others were stuck in small regions of the rough areas. This is shown in figure A.8 in section A.5.

Finally, to demonstrate the wetting contrast between the rough surface and the flat PDMS wells, droplets were carefully deposited on the surface with a pipette. For flat PDMS, it was observed that water deposited through this method tended to stick very well to the area where it was deposited. For the most hydrophobic rough PDMS surfaces however, the droplets would not attach to the surface as they sticked better to the pipette tip. As the droplets at the end of the pipette tips was put in contact with the PDMS surface, it immediately adhered to the flat PDMS wells, even if the droplets were not deposited exactly at the well positions. Droplets with various volumes were tried. Initially, droplets with a volume of 10 μL were deposited, however they were highly unstable due to their large size, and small vibrations caused them to deform and come in

contact with other wells. Additionally, they were so large that droplets could not be deposited at two neighbouring wells, since the separation distance was smaller than the droplet diameter. An optimal volume of 2 μL was found after several trials. The result of depositing droplets through this method is shown in figure 4.20. A solution of a blue colour dye was used instead of water to make it easier to differentiate between the droplets and the PDMS surface (as both are transparent) There was no obvious difference in the wetting behaviour between the dye solution and de-ionized water. As can be seen from the image, most droplets have a large contact angle and their diameter exceed the diameter of the wells. Some droplets with a volume of 2 μL were not able to be deposited on the wells, as they adhered better to the pipette tip. This was solved by increasing the droplet volume. Thus, the droplet size distribution in the image is not homogeneous. The deposited droplets adhered strongly to the patterned regions; even tilting the sample to 90° or turning the sample upside down did not move the droplets, as shown in figure A.10.

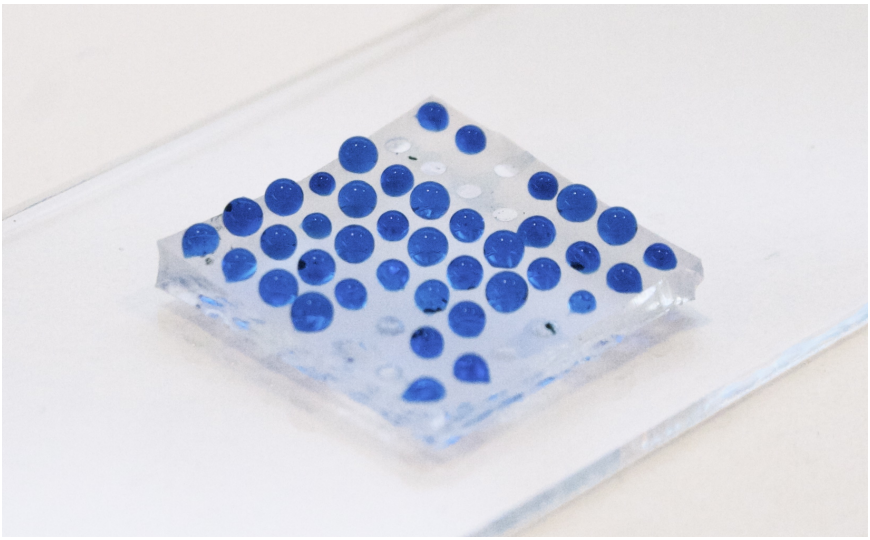

Figure 4.20: Photograph illustrating the difference in wetting contrast between the rough PDMS regions and the patterned PDMS wells. The deposited droplets wetted the surface strongly in favour of the flat wells than the rough surrounding region.

Chapter 5

Discussion

Contents

5.1 Fabrication of copper templates

5.1.1 Etching

From the results presented so far, it can be seen that the methods of etching, oxidation and electrodeposition produce quite different surface roughness. Etching produces large height variations on the surface, as illustrated in figure 4.1. Polycrystalline metals consist of grains of atoms with different crystallographic orientation. The chemical reactivity of atoms in some single-phase metals depend on the crystallographic orientation [70]. Thus, in a polycrystalline material, the rate of etching varies from grain to grain. This produces surface roughness on the scale of the grain size in the material. In addition, the etchant will produce roughness on the surface of the grain itself. Thus, the etching of the polycrystalline copper produces two-scale surface roughness of the copper templates. The roughness becomes larger with increased etching time as was

illustrated in figure 4.1. Etching for 30 minutes produces a maximum height difference from the mean line of typically 5 μm, although values as high as 10 μm were observed.

From the experiments with varying the concentrations of HCl and $CuCl_2$ and etching time, it can be seen that the roughness is significantly lower than the initial results for the samples etched with the used solution. The highest value of R_q from these measurements is 153 nm, for a sample etched with a 5 wt % HCl and 5 wt % $CuCl_2$ solution for 15 minutes. This value is close to what was measured for a sample etched for 1 minute with the used solution (R_q = 208 nm), but far from the sample etched for 60 minutes (R_q = 2392 nm). While the kurtosis of these samples fluctuated around a value of 3, the samples etched with known concentration had a kurtosis value mostly lower than 1.

There are large uncertainties in the measured values of the correlation length β^*. The length was originally defined for exponential decaying autocorrelation functions [36]. Looking at figure 4.3b and figure 4.4b, the estimated autocorrelation functions from the AFM measurements does not follow an exponentially decaying function perfectly. Some of the curves decay exponentially to about 40 % of the initial value, where they transform into a linearly decaying part. Other curves start a delayed exponential decay, shifted some distance away from the y-axis. Since the curves have different forms, it is difficult to define a parameter that describes the decaying sufficiently. For instance, if the correlation length was chosen as $C(\beta) = 1/e$ instead, the order of samples from highest to lowest correlation length would have been different.

Similarly, the standard deviation σ of the height distributions shown in figure 4.3a and figure 4.4a were calculated from fitting the curves to a Gaussian function. The raw data and the Gaussian fit curves for samples etched for a different amount of time, is shown in figure A.2 and A.3 in the appendix. However, not all of the curves are symmetrical and therefore don't follow the Gaussian distribution. Especially the samples that show a large deviation from a zero skewness in table 4.2, 4.3, 4.4 and 4.5 are non-symmetrical. Also, samples showing a large deviation from a kurtosis value of 3 can be considered non-Gaussian, meaning that the surfaces are not completely random.

The difference in the roughness results could be due to the different measurement methods used. A large difference between AFM and the profilometer is the spatial resolution, which is much higher for the AFM because of the sharp tip used. The radius of curvature of the AFM tip is 10 nm according to the manufacturer, while it is 12.5 μm for the profilometer. It is therefore not ex-

pected that the profilometer will be able to resolve small surface features due to tip convolution of the large probe, as discussed in section 2.3.2. The sharper the tip, the more closely it will be able to follow the surface texture. Poon et al [71] simulated line profiles for tips with different radius of curvature from an original AFM profile, and showed that increasing the tip size decreased the value of the measured RMS roughness R_q and increased the correlation length β^*, due to tip convolution. Thus, a surface scanned with a sharper tip would appear to be more rough, as expected. Based on this, the surface roughness should have been higher for the AFM measurements than those measured by the profilometer, if all other parameters were held constant. However, the results show that the oppposite is true; the AFM data show a lower roughness than the profilometer. Thus, the different results cannot be explained by using different instruments for obtaining the surface data.

Another parameter that could affect the roughness is the scan length used. Bhushan [36] showed that the value of R_q increased with increasing scan size before it was saturated at scan lengths above 10 μm. For the profilometer, the scan length was 500 μm, while it was 100 μm for AFM. Therefore, this should not affect the measurements either.

However, there may be roughness occurring at the nanoscale for the samples etched with a known concentration, supported by figure 4.12b. Thus, it may be that the large scan length used is not able to detect the small-scale roughness sufficiently. To compare the roughness at this scale against the samples etched with the used etchant, one should use a smaller scan length, for instance 5 μm.

Based on the discussion so far, the large difference in roughness can not be explained by possible artefacts from the measurements. For the samples to fit onto an AFM sample holder, the copper plates had to be cut by the workshop into smaller pieces. Since the roughness depends on the grain structure of copper, and grain structures could be altered by mechanical deformation or heating, there is a possibility that the grain structures were changed by the mechanical processing. However, the initial results were later reproduced using a used copper etchant on the smaller plate dimensions, refer to table A.7 and A.8.

It is therefore likely that the etchant solution is responsible for the change in roughness. Since the etching rate increase with increasing concentration [44], both the etching time and the concentration of the constituents had to be examined independently. Looking at the results in figure 4.4 and table 4.5, it appears that the RMS roughness R_q increases with time until it is saturated after 15

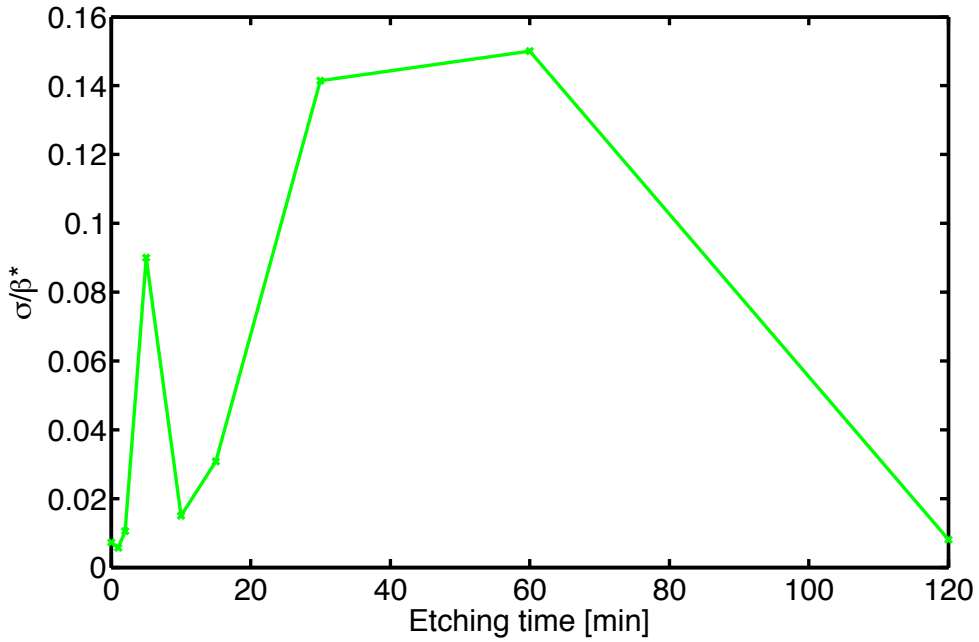

Figure 5.1: The ratio of σ/β^* plotted as a function of etching time, for copper plates etched with 20 wt% HCl and 20 wt% $CuCl_2$.

minutes, when using 20 wt% of HCl and 20 wt% of $CuCl_2$, and that the roughness variations after this is a result of differences between individual samples. Also the value of R_q increase with decreasing concentration of HCl and $CuCl_2$. Looking at the correlation lengths β^* does not reveal any trends as mentioned earlier, and the results seem to be largely affected by uncertainties.

As mentioned in section 2.2.2, the contact angle on a surface has shown to increase by increasing the value of σ/β^* [31]. Figure 5.1 shows this ratio plotted as a function of etching time. The value is highest when etching for 30 and 60 minutes, but does not otherwise show any correlation with etching time. This may be due to the combined uncertainties in both σ and β^*.

The results suggests that there are no simple correlation between etching time, concentration and roughness. Since the roughness is based on the grain structures of the copper plates, there may be large individual variations between each sample, which cause larger differences in the measurements than the different process parameters. To reduce the uncertainties, multiple samples have to be made for each etching condition.

Roughness is composed of many wavelengths superimposed upon each other [39]. However, roughness wavelengths smaller than the sampling intervals for the line scans, or larger than the scan size does not contribute to the calculated roughness parameters [71]. From figure 4.12b, it is evident that there are now large-scale

roughness present on the copper surface, other than what is produced by the use of an etching mask. Thus, nano-scale roughness does not effect the measured values of β^* and σ, and new AFM scans with a lower scan size have to be conducted to examine the effect at a lower scale.

Looking at the etching mechanism presented in section 2.4.1, etching of Cu with $CuCl_2$ produces CuCl. This means that if the solution is not changed between each time a copper plate is etched, the concentration of Cu^{2+} ions will decrease because it is reduced to Cu^+. As explained earlier, CuCl reacts with HCl and forms $CuCl_2$, which keep the etching going. However, not all Cu^+ ions form CuCl, as they also form different complexes such as $[CuCl_2]^-$ and $[CuCl_3]^{2-}$ [46]. To oxidize all the Cu^+ ions, an oxidizing agent must be present. One such agent is atmospheric oxygen, however the process may take a long time considering accessibility (solution was kept in a sealed glass bottle), volume of etchant (1 liter) and recovery rate (slow at room temperature). Increasing the concentration of Cu^{2+} ions in the solution, leads to higher etching rates [46]. Thus, the reduction of the Cu^{2+} ions in favour of Cu^+ ions, causes a slower etch rate for the etchant.

If the concentration of the etchant is very high, it may cause the etch rate to be saturated for some of the grains. If this is true, increasing the etchant concentration will lead to a lower differences in the amount of etching between the grains. This may cause the surface roughness to be low at length scales similar to the grain size, but high at smaller scales due to etching on the grain itself. As mentioned, the roughness seems to decrease with both the increasing concentration of HCl and $CuCl_2$. Thus, a possible explanation for why the measured micro-roughness was low is that the etching rate is too high. At lower concentrations, it may be that only a few grains are saturated, leading to a larger difference in etch rate. However, further experiments examining the effect with different concentrations of Cu^+ ions and Cu^{2+} ions on the surface roughness should be conducted before any conclusion can be drawn.

5.1.2 Oxidation

As stated earlier, the CuO layer grown on copper substrates tended to flake off when it was oxidized for a prolonged time. The flaking has previously been attributed to the large surface mismatch between metallic copper and Cu_2O [72, 73]. A new strategy for growing non-flaking CuO nanowires was based on using 25 μm thin copper foils [26]. With this setup, the thickness of the oxide layer

was found to exceed the foil thickness, so that the misfit stress would deform the thinner copper substrate rather than deforming the oxide layer, which is the case for thick substrates. In this project, copper plates were preferred instead of foils, mainly because of the larger grain size of the foils, which would affect the surface roughness after etching. In addition, the copper plates are planar and more mechanically stable due to their thickness, which would make the replica moulding process with PDMS easier.

The oxidation of the copper plates for 30 minutes lead to growth of nanowires, while it was not formed at shorter times, as shown in figure 4.6b. It seems that the density are lower and the length of the nanowires shorter compared to previous work, which reports nanowire lengths up to 15 μm [47]. The nanowire length are mainly controlled by the oxidation time, with a growth rate of about 3 μm/h. The nanowires has been reported to have diameters ranging from 30 to 100 nm, which is dependent on the oxidation temperature. Most nanowires oxidized at 500° C will have a diameter between 50 and 100 nm. The nanowire density is controlled by the O_2 partial pressure [48].

The nanowires in this project were oxidized in ambient air without any pressure control. The low density may be due to this, or the fact that the nanowire length is not homogeneous, so that the shortest wires are difficult to image in the SEM. The nanoscale roughness of the oxidized copper is higher than the etched copper due to the high-aspect ratio dimensions of the nanowires. Increased density and wire length would further increase the roughness, but will lead to more flaking. As will be discussed later, due to the elasticity of PDMS, it is very unlikely that it is possible to replicate the nanowire structures. Thus, the oxidation parameters were not examined further in this study.

5.1.3 Electrodeposition

The image in figure 4.7 shows the surface of electrodeposited copper, which was produced using the formation of hydrogen bubbles due to the electrolytic reduction of H^+ as a template. Compared to etching or oxidation, this process yields a different type of surface roughness. One should be aware that the image is obtained using a higher tilt angle than 24°, which was used for the other samples. Thus, the image appears to be more 3-dimensional. The electrodeposited copper seems to give high aspect ratio structures, though not as much as the CuO nanowires in figure 4.6b, since the size of the electrodeposited particles are larger than the nanowire diameter. The copper particles appear to be smooth

on their surface. Also, the large-scale roughness seems to be lower than for the etched copper in figure 4.2b, but possibly higher than that for oxidizied copper. As stated earlier, the surface roughness could not be studied quantitatively with the current AFM setup, due to the problem with tip convolution and scanning of high-aspect ratio structures.

Previous work achieved seemingly higher surface roughness than the results presented here, for instance in the work by Li et al [51]. The surface roughness depends on the amount of electrodeposition and the size and stability against coalescence of the hydrogen bubbles in the electrolyte solution. The amount of electrodeposited copper was limited to the surface area of the copper anode. The larger the copper anode surface was, the higher amount of copper was electrodeposited. The electrodeposition stops after a few seconds because the electrode is passivated. The mechanisms behind the passivation are still under debate, though there are three possible theories. Since the solubility of $CuSO_4$ is low, it is possible that copper sulphate crystals deposit at the copper anode and act as a insulation layer [74]. Another explanation may be that high current densities cause the oxidation of copper to Cu^+, which may react with water in the electrolyte and form a Cu_2O passivating layer [75]. A third explanation is that the prescence of nickel ions in the electrolyte may facilitate the passivation as discussed by Jarjoura et al [76].

The thickness of the porous electrodeposited layer may thus be increased by using an anode with a larger surface area, and thus produce a surface with more roughness. However, similar to the discussion on CuO nanowires, it is not realistic to replicate high-aspect ratio structures that would be mechanically stable in PDMS.

5.2 SU-8 processing

The SU-8 replicas of copper templates that were etched, oxidized or electrodeposited produced a different kind of surface roughness, as expected. Not all the samples were replicated to the same degree however. As shown for the PDMS replica of etched copper in figure 4.8, not all parts of the surface have been replicated from the template, since some areas appear to be very planar. Other areas with a low surface roughness were found on several SU-8 replicas, which are not presented in this report. Despite this, most of the replicas seemed to follow the surface roughness of the template quite well.

A likely explanation why some areas of the SU-8 replicas had a low surface

roughness, may be due to trapped air at the interface between SU-8 and copper before cross-linking. During deposition of SU-8 on the copper templates, it was observed that it did not wet the copper surface as easy as water did. To wet the whole surface, cocktail pins were used to spread the solution. SU-8 is known to wet surfaces poorly, due to the high surface tension of its solvents, especially those based on gamma butyrolactone, such as the SU-8 2 and SU-8 5 [77]. Superhydrophobic surfaces are not wetted by water since the surface tension of water is too high to form a completely homogeneous interface with the underlying solid. It may also be true for SU-8, that it is not able to wet the smallest and most narrow grooves in the copper templates.

This explanation was the reason why some samples were degassed in a desiccator before the soft baking step. If air bubbles were trapped at the copper - SU-8 interface due to insufficient wetting, they could be removed due to the large pressure difference caused by the vacuum. Indeed, bubbles emerged readily to the surface of the resist after only a few minutes of degassing. However, it is known that evaporation of the resist solvent can cause bubbles to appear at the surface, and that the evaporation rate may increase under vacuum [78]. Thus, it is not possible to conclude whether the emerged bubbles were caused by diffusion of trapped air or due to solvent evaporation. The bubbles may well be a combination of both, as degassing is regularly used to remove bubbles in other liquids such as PDMS, which is discussed later.

Another obstacle in achieving high-quality replica moulds of the copper templates in SU-8, is the low adhesion between the resist and the copper surfaces. A stated earlier, wrinkling of the resist occurred during post-exposure bake and caused insufficient replication as shown in figure 4.9. Additionally, some of the unexposed SU-8 resist popped out from the resist surface. The wrinkling and the deformation of unexposed SU-8 is likely due to the generation of internal stress in the resist, a known problem caused by volume expansion during heating. While baking, both the copper and SU-8 expand at the interface. The two materials have a mismatch in the coefficient of thermal expansion, which is $17.1 \cdot 10^{-6}$ K^{-1} for copper and $52 \pm 5.1 \cdot 10^{-6}$ K^{-1} for SU-8 [79]. The difference in expansion cause stress in the SU-8, which is released by deforming the SU-8 film or through the detachment from the interface [80]. Since the copper templates have a high surface roughness and therefore a large surface area, the generation of stress may be a larger problem than for flat substrates.

Non-crosslinked SU-8 is softer than crosslinked resist, thus it is likely that internal stresses due to volume expansion are released by pushing the unexposed

resist upwards away from the substrate. It is also a reasonable explanation for why one could observe rings of smooth SU-8 surrounding the patterned squares in figure 4.9. Since the unexposed SU-8 is softer than the rest of the resist, it is likely that the surrounding areas detach from the surface. The glass-transition temperature of non-crosslinked SU-8 has been reported to be 55° [81]. Around this temperature, it is possible that the exposed polymer is able to re-flow and smoothen out to a certain degree before crosslinking is completed, where the resist is freestanding. This may be the reason why the area surrounding the patterned squares has a very low surface roughness.

Internal stresses can be reduced by carefully controlling the temperature ramping rate both during heating and cooling, so that the resist have time to relax the stress without loosing contact with the substrate. Indeed, some samples were soft and post-exposure baked for several hours without solving the wrinkling problem. Since the internal stress is largest for resists with thickness above 100 μm, thinner resist layers could be used. However, this can also cause the resist surface to be uneven due to the large template surface roughness, as stated earlier.

Another solution to reduce detachment problems, could be to sputter coat the copper surface with a thin layer of another metal with better adhesive properties than copper. Dai et al investigated the adhesive strength of cured SU-8 on various metallic surfaces [79]. They found that SU-8 had considerably stronger adhesion on titanium, gold or chromium, than on copper. Only nickel showed a lower adhesion. Thus, sputter coating the copper templates with a 50 nm layer of for instance titanium, should improve the adhesive strength.

In addition to the generation of internal stress, it is known that oxidation of metal surfaces as well as the presence of any moisture, have a negative effect on the adhesive properties [82]. Exposing copper to air leads to the formation of a thin oxide surface layer. This effect may further aggravate the adhesive strength between the substrate and SU-8. Thus, adhesion between the copper and SU-8 resist can be improved by removing the oxide layer immediately before spin-on, by washing the sample with HCl.

If these methods prevent SU-8 detaching from the copper surface during post-exposure bake, PDMS pillars could be made instead of wells. As previously mentioned, submerging the PDMS replicas in water led to non-wetted wells due to the trapping of air bubbles. If pillars were used instead, this problem would be avoided. Additionally, it is believed that droplets will attach more readily when encountering a pillar instead of a well.

Looking at the SU-8 surfaces replicated from oxidized copper in figure 4.10, one can see small bumps protruding the surface. Since the SU-8 is the negative replica, the bumps are replicas of the pores in the CuO layer. The aspect-ratio of the bumps is however low. The thickness of the CuO is usually around a few microns [26]. Thus, the maximum dimple height is limited by this. It may also be limited by inhomogeneous wetting of the surface as discussed earlier, where the CuO layer is not completely wetted.

The inhomogeneous wetting may also limit the roughness of the electrodeposited copper replica, shown in figure 4.11. From the image, it seems that some parts of the porous electrodeposited copper layer is wetted, and thus replicated in SU-8. These kind of structures seem to be very smooth at small length scales however, and may suggest that the mould is not filled accurately at the nanoscale. The small-scale roughness may also be caused by local adhesion problems, as discussed previously. In other parts of the surface, the micro-scale roughness is relatively low compared to etched copper. However, the SU-8 seem to replicate the shape of the electrodeposited Cu particles well, with dimples of varying size, with the largest dimples being about 1 μm in diameter.

Figure 4.12 shows copper etched using patterned SU-8 as a mask. Although the micro-roughness is increased with this method, it is probably a better strategy to use the initial copper etchant solution, which gives a very high surface roughness. The copper pillar top surface was measured to be 16x16 μm, which is smaller than the top SU-8 pattern, measured to be 28x28 μm. Etching for 8 minutes produce a pillar height of 6.5 μm, which is the about the same as the underetch on the SU-8 patterns. This means that the etchant is isotropic, as expected. After the SU-8 is removed from the surface, the surface will consist of copper pillars with rounded edges, due to a higher exposure to the etchant solution there. The pillar separation at the base will be 73 μm, the same as the distance between the SU-8 patterned squares. At the top however, the distance is 85 μm. The high inter-pillar separation distance relative to the pillar dimensions will hardly increase the surface roughness at all. Assuming for simplicity that the etched pillars have a cubic shape, the roughness factor used in equation 2.10 after etching will be increased by a factor of only 1.04. Thus, only a 4 % increase in surface area will be achieved with this method. The hydrophobocity of PDMS replicas will therefore only be increased by a very small amount. It is possible to improve the roughness by using a different mask where the square patterns are packed more densely. In addition, physical etching methods can be used instead of the wet chemical etchant to give anisotropic etching, which gives

high aspect-ratio structures. However, this requires more advanced laboratory equipment and makes the fabrication process more complex, which would not be suitable for industrial production with today's existing technology. Optimizing the surface roughness on SU-8 resist replicated from copper templates with the methods described previously, seems like a better strategy.

5.3 PDMS replica moulding

The PDMS surface in figure 4.14 replicated from etched copper, shows similar structures as the copper template in figure 4.2. However, the edges seem to be more smooth than the surface features of the etched copper and the negative SU-8 replica shown in figure 4.8. The same smoothness can also be observed for PDMS replicas from oxidized and electrodeposited copper in figure 4.15 and 4.16 respectively. This illustrates one of the main problems associated with PDMS replica moulding of nanosized objects, which is the low Young's modulus of the cured polymer, which means that the material is quite elastic. This material property makes it difficult to replicate high-aspect ratio structures. Another problem is the strong adhesive forces between PDMS structures, causing pillars to collapse into each other or to the ground surface [83]. The stability of microfabricated, high aspect ratio structures in PDMS was investigated by Roca-Cusachs et al [84]. Pillars with a given aspect ratio value became increasingly unstable as their diameter decreased, due to buckling and adhesion towards the surface. They found that the critical aspect-ratio before collapse of the pillars was about 5 for posts with a diameter of 2.29 μm, while it was reduced to about 2 when the pillar diameter was reduced to 0.36 μm. Since the ground collapse is partly due to adhesion towards the surface, the critical aspect ratio also depend on the separation distance between pillars. The low elastic modulus of PDMS would make it impossible to replicate the CuO nanowires, which have an aspect-ratio of at least 20. It would also not likely replicate the surface of electrodeposited copper completely, as can be seen in figure 4.16, where only the topmost copper particles have been replicated. It was mentioned earlier, that increasing the curing temperature from 80 to 120°, lead to better replicas. The reason may be that the mechanical stability is improved, and that the high aspect-ratio structures become more stable.

As with SU-8, the replica moulding may be inaccurate due to inhomogeneous wetting, since the SU-8 mould was coated with a hydrophobic SAM. However, Sun et al replicated a superhydrophobic lotus leaf, with a contact angle of 162°,

with features as small as 20 nm being replicated [23]. Thus, it is likely that the stability of high-aspect ratio structures is a greater problem than wetting of the mould. It could also be that small surface features were replicated, but destroyed mechanically when the replicas were peeled off from the template mould.

As previously stated, PDMS has to be degassed in a desiccator to remove air bubbles caused by mixing the base and curing agent to the prepolymer. This is because the prepolymer is quite viscous, so that air is easily trapped. It is possible that air is trapped during the filling and can't escape because of the high viscosity of PDMS. After pouring over the prepolymer, the template was thus placed in vacuum again. This process step increased the replica quality of electrodeposited copper. Thus, the degassing of the prepolymer deposited on the template should be used for further work.

5.4 Wettability of PDMS replicas

5.4.1 Contact angle measurements

The measured contact angles for the different samples presented in table 4.6, confirm that surface roughness increases the hydrophobicity for an intrinsic hydrophobic surface, as discussed in section 2.1.3. The difference in the observed contact angles is due to the differences in surface roughness of the replica moulded surfaces. Overall, the replica moulded surfaces from etched copper have the highest contact angles. Some of the replicas from oxidized copper are also quite hydrophobic. It seems like the replicas from the electrodeposited copper surfaces is the least hydrophobic.

Comparing the measured contact angles and the roughness parameters shows that the highest observed contact angle, which was 154.7 $\pm$ 5.3°, is replicated from the sample with the highest RMS-roughness R_q, as expected. However, it can be seen that the replica from the copper plate that was etched for 10 minutes shows a higher contact angle than the surface etched for 20 minutes. Also, the PDMS replica from copper etched with known concentrations for 120 minutes, which have a much lower surface roughness at the micro-scale as discussed earlier, have a comparable hydrophobicity. This shows that one cannot simply rely on high values of R_q. The values of skewness and kurtosis are also listed. As discussed earlier, a positive skewness means that the surface is composed of mainly peaks, while a surface with a negative skewness will be dominated by valleys. The kurtosis is the measure of "spikiness" of the surface, i. e. the sharpness of

the surface features. For instance, a surface covered with CuO nanowires will likely have a high kurtosis and a positive skewness.

One has to remember that the polarity of the skewness change when replicating the template mould, as demonstrated in figure 5.2. The blue curve is the surface profile from one of the profilometer scans, while the red curve uses the same height data, only that the polarity is changed (assuming perfect replication). The negative skewness of the template surface leads to a positive skewness of the replica surface, keeping the magnitude constant. The value of the kurtosis is not changed. The value of R_q is also the same for both surfaces.

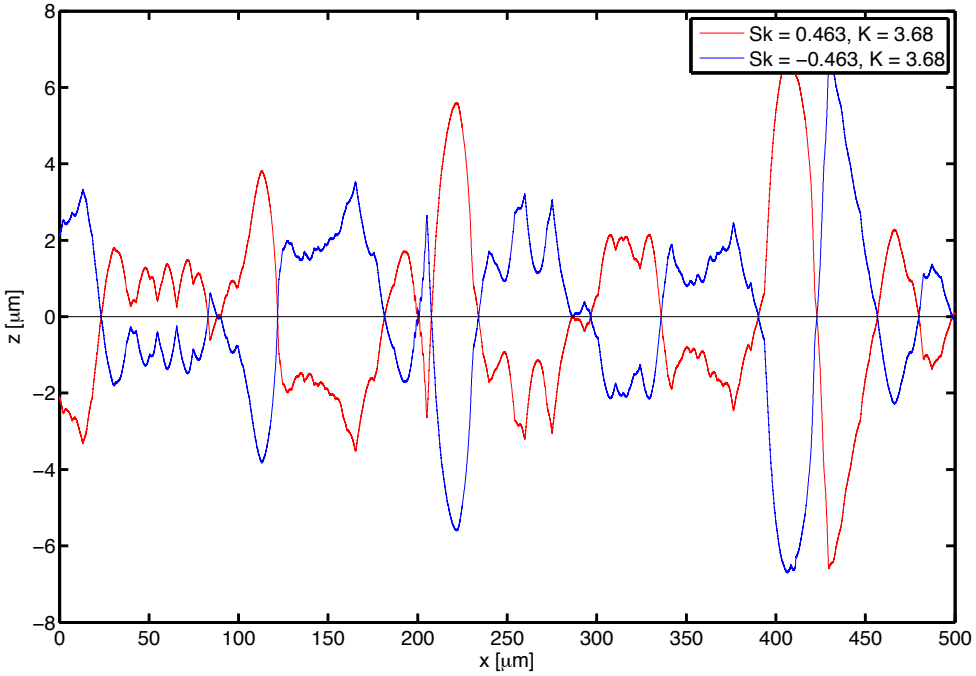

Figure 5.2: The polarity of the skewness is switched, while the kurtosis is constant for the replica (red curve) of the template surface (blue curve). The surface profile of the replica was simulated in Matlab by changing the polarity of the height data.

Bhushan et al [85] measured the skewness and kurtosis of the surface of the Lotus leaf to be 2.0 and 6.7 respectively (scan length of 50 μm). Furthermore, Sun et al made both a negative and positive replica of the Lotus leaf in PDMS. The negative replica had a contact angle of only 110°, while for the positive replica it was 160° [23]. This suggests that the positive replica surface with a large positive skewness were able to maintain a composite wetting state, while the negative replica with negative skewness was not. Although the connection between wetting physics and surface structure is not fully understood, it is evident that the skewness plays a critical role.

The PDMS surfaces were replicated directly from the copper surface without

using SU-8 moulding as an intermediate step, and they are therefore negative replicas. Thus, the skewness of the replicated samples in table 4.6 have the opposite surface polarity with respect to the displayed value. This means that the PDMS surface replicated from copper etched for 20 minutes, will have a negative skewness, and is thus less suited for maintaining a heterogeneous interface. Based on the former discussion, this may support the claim that surfaces with a large number of peaks, together with a low surface energy are required to produce superhydrophobic surfaces. The etching of the copper plates with 20 wt% HCl and $CuCl_2$ produced a low surface roughness, as shown in the table. However, the contact angle and skewness is comparable to the former discussed sample, and the kurtosis is much lower, suggesting that there are very few spikes on the surface. This is not straightforward to understand. A possible explanation may be that there are considerable roughness, only at a much smaller scale than the AFM scanning length, supported by figure 4.12b. The measurements are not able to detect roughness at all scales using only a single scan, as discussed earlier.

It is difficult to explain the lower contact angles measured for replicas of oxidized and electrodeposited samples when no quantitative roughness data could be obtained. However, a likely cause is the lower surface roughness for the replicas of these templates, as explained in the previous section. Since PDMS is such a soft material, it is difficult to replicate the nano-scale roughness. Without any micro-scale roughness present, the replicated surface will appear very smooth. Thus, it seems a better strategy to replicate from etched copper plates, which produce roughness at multiple length scales.

However, Nosonovsky et al [31] showed through modelling that surfaces with sharp edges have a large contact angle hysteresis, due to pinning of the triple line (the line where the three phases of liquid, gas and solid meet) of the droplets. This means that a surface with a sawtooth pattern will have a larger hysteresis than surfaces with hemispherically shaped asperities, with all other roughness parameters being equal. It was observed that etched copper plates have very sharp edges. Although the surface features in PDMS are more smooth, the contact angle hysteresis could be lower for PDMS replicas of electrodeposited copper, if the roughness was high enough so that the surfaces followed the Cassie-Baxter wetting state. Thus, for further work, it would be interesting to carry out a small amount of electrodeposition on the etched copper surfaces with highest micro-scale roughness. Based on this discussion, it could be that PDMS replicas from such a surface will display a high contact angle and a low hysteresis at the

same time.

A source of uncertainty in the measured contact angle is contamination on the surface, altering the surface chemistry of PDMS. In addition, the surface roughness is not homogeneous throughout the samples, so the contact angle could be depending on where the water droplets are deposited.

The highest observed contact angle, which was $154.7 \pm 5.3°$, would be characterized as superhydrophobic by some sources [17]. This is an increase of 52.9° with respect to flat PDMS. Table 5.1 gives an overview of some reported contact angles for replica moulded PDMS surfaces.

Table 5.1: An overview of reported water contact angles for rough PDMS surfaces prepared by replica moulding

Template	**Contact angle [°]**	**Ref.**
Surface of the Lotus leaf (*Nelumbo nucifera*)	160	[23]
Microfabricated wells in SU-8 with side-lengths 25 μm and periodicity of 80 μm	152.5	[86]
Microfabricated wells with period and diameter of 10 μm in SU-8	155	[24]

Superhydrophobic PDMS has been fabricated in other cases than those shown here, however the superhydrophobicity stems from altering the surface chemistry through fluorination with CF_4 plasma [87], SF_6 plasma [88] or covalent grafting of perfluorinated SAMs [89]. The plasma treatment requires advanced laboratory facilities and equipment, and have to be applied to every fabricated PDMS device. In addition, surface treatment of PDMS tends to be temporary. For instance, PDMS can be rendered hydrophilic by treating it with oxygen plasma, a method commonly used in microfluidics. However, the hydrophobicity is retained after less than an hour due to diffusion of low molecular weight polymer chains from the bulk to the surface [90].

The measured contact angle depends on how the droplet is deposited. For instance, He et. al. [86] reported a contact angle on microfabricated PDMS pillars of 152.5° when the droplet was gently deposited on the surface, while the resulting contact angle of a similar droplet deposited from some height was found to be 123.4° on the same surface. This is thought to be due to a transition from the Cassie-Baxter state to the Wenzel state caused by an external stimuli [91], in this case by applying a pressure on the water-air interface. Through the sessile drop method used to obtain the contact angles in table 4.6, the droplets

were deposited from a low height. This height is thus an uncertainty in the measurements.

However, despite the high contact angles, the droplets are likely to be in a Wenzel wetted state, or a combined Cassie-Baxter/Wenzel state with a high contact angle hysteresis, since they tended to stick very well to the replicated PDMS surfaces. In the work by He et. al. [92], the contact angle of flat and rough PDMS was investigated. The intrinsic advancing and receding contact angles for PDMS was reported as 115° and 88° respectively (contact angle hysteresis = 27°). Fabrication of micropillars in PDMS with sidelengths 22.7 μm and 28.7 μm, and a height of 30 μm were done by photolithography and replica moulding. The advancing and receding contact angle for a drop in the Cassie state was found to be 152° and 142° respectively, while in the Wenzel state, the receding contact angle could not be determined. This suggests a very high hysteresis for a droplet on PDMS in a Wenzel state, while it is significantly reduced in the Cassie-Baxter state.

Based on these results, it is likely to believe that the replicated PDMS surfaces does not follow the Cassie-Baxter wetting regime completely. This is probably the reason why water does not stick selectively to the patterned area, but distributes in a more random manner. For capturing water droplets, one would need the water droplet to stick to the patterned areas only, while the background is highly repellent, following a Cassie-Baxter regime. In order for the device to work, it will be necessary to be able to make templates with sufficient surface roughness and geometries, so that the contact angle hysteresis on the replicated PDMS surface is lowered.

5.4.2 Spatial wetting contrast

Wetting contrast of the PDMS replicas was obtained from etched copper plates patterned with SU-8 pillars, as shown in figure 4.19 and 4.20. The largest average difference measured between the rough and smooth PDMS was 52.9°. Droplets wetted preferably the patterned areas of flat PDMS, where the adhesion to water was stronger. In the surrounding rough areas, the water rolled off more easily.

However, the selective wetting of water on the surface has not been optimized yet. In an ideal system, the rough PDMS would be superhydrophobic, displaying a contact angle above 160°. The partial water capturing of water droplets in some patterned regions, and the wetting of some of the rough areas shows that there is a non-homogeneity of the hydrophobicity in the rough regions. In other

words, it is likely that some of the rough PDMS is superhydrophobic, while other regions are not. Droplets rolling over the surface in a composite Cassie-Baxter state will get stuck once it encounters regions following the Wenzel wetting regime, similar to the patterned regions.

The water-capturing worked better for the surface functionalized copper plates with SU-8 pillars. Previously, the water contact angle of fluorinated copper etched with a similar procedure has been reported to be as high as 171° [25]. The contact angle on the gold coated SU-8 pillars would be around 116°, the value of a flat surface coated with perfluorodecanethiol [63], which gives a contact angle contrast of 55°. The contrast is similar to what was obtained with surface structuring of the PDMS. However, the copper surrounding the SU-8 pillars is much more hydrophobic than the highest measured values of PDMS. Water droplets deposited on these surfaces were very unstable and rolled off the surface by tilting the sample only by a few degrees. The lower hydrophobicity is the reason why droplets do not deposit that selectively on the PDMS surfaces as for the copper-SU-8 system. To be able to make a surface where droplets only deposit on the patterned spots of PDMS, sufficient surface roughness have to be achieved so that the contact angle is at least 160° throughout the surface.

The water-capturing of the PDMS surfaces can likely be improved by optimizing the photolithography-pattern. The currently patterned PDMS have wells with a diameter of 750 μm, separated by a distance of 1200 μm. Since droplets tended to bridge across several PDMS wells, the separation distance could be increased, so that large droplets already attached to one well would split or detach instead of attaching to a new well.

Once the wetting of the surface have a sufficient selectivity, the wetting contrast can be further improved through chemically modifying the patterned PDMS wells to render them hydrophilic. Since only the patterned spots are wetted, the surface linking will only occur there. Thus, the wetting contrast can be significantly increased. Usually, PDMS is treated with oxygen plasma, which creates hydrophilic silanol surface groups. However, this method is not suitable for this purpose, since the whole surface will be exposed to the plasma. Due to the surface roughness, the PDMS will then become superhydrophilic as discussed in section 2.1.3. A method developed by Hu et al [93] involved grafting acrylic acid (AA) monomer in an aqueous solution containing $NaIO_4$ and benzyl alcohol. The reaction required continous exposure by UV-light under a mercury lamp, to create radicals on the PDMS surface. The generation of surface radicals then initiates attachment of monomers and polymerization. The lowest measured

contact angle through this method was 45°. Since the contact angles for the PDMS surfaces produced in this report were measured using de-ionized water, it is not clear how droplets of aqueous solutions will wet the surface. Assuming that the solution used by Hu et al have equal wetting properties as water, the wetting contrast could be improved to be larger than 110° in terms of contact angle.

Chapter 6

Conclusion

In this study, PDMS surfaces with patterned wettability were made through surface structuring, without any modifications of the surface chemistry. PDMS replicas were made from copper surfaces, using etching, oxidation or electrodeposition as methods to produce surface roughness. Characterization of the surfaces in SEM showed that etching copper with a solution of $CuCl_2$ and HCl, produced roughness on both the microscale, due to different etch rates on differently oriented grains, and the nanoscale due to etching on the grains themselves. Oxidation and electrodeposition also produced nanoscale roughness, however the microscale roughness was significantly lower with these methods.

By surface structuring, the water contact angle of PDMS was increased from $101.8 \pm 3.6°$ to $154.7 \pm 5.3°$, which is similar to other reported values in the scientific literature. The PDMS surfaces with the highest observed contact angles, were those replicated from etched copper plates. This shows that superhydrophobicity is more easily achieved when replicating from templates with a large micro-scale roughness, since high aspect-ratio structures in PDMS becomes increasingly unstable at smaller length scales, due to the low intrinsic stiffness. In addition, it was found that the surface polarity of the replicas influenced the wetting behaviour, with surfaces having a large, positive skewness being most hydrophobic. Using SU-8 as an intermediate replica step to produce positive replicas of the copper templates in PDMS, can be a way to achieve the optimum surface polarity.

Water droplets deposited on the PDMS surfaces with the highest contact angle contrast adhered strongly to the flat regions, relative to the rough regions. This enabled selective deposition following the surface pattern, by using a pipette. Other methods of deposition showed less selectivity of wetting, as droplets were transformed from the Cassie-Baxter to the Wenzel wetting state. For the droplet-capturing to be fully functional, the hydrophobicity of the rough PDMS regions have to be increased, while the contact angle hysteresis have to be decreased, so that pinning of water on the non-patterned surface is avoided.

Further work

To further improve the device developed in this study, some points should be adressed. First of all, a better understanding of how the concentration of Cu^+ ions in the etchant solution impacts the surface roughness, would make it easier to optimize the creation of templates. This could be carried out by adding CuCl in various concentrations. Furthermore, more large-scale roughness could be produced by etching the copper foils, which have a larger grain size. This could then be combined with electrodeposition to produce roughness at multiple length scales.

It would also be beneficial to quantify the surface roughness further of the PDMS replicas with AFM, as a way to assess the replication accuracy. To reduce the problems associated with making thick, mechanically stable negative replicas in SU-8, the copper template could be sputter coated with a thin metal layer of for instance titanium, to improve the adhesion. Furthermore, other photolithography masks could be used, to produce wells or pillars with a larger spacing distance. In this way, the problem of droplets bridging across several flat regions could be avoided.

Appendix A

Appendix

A.1 AFM surface analysis

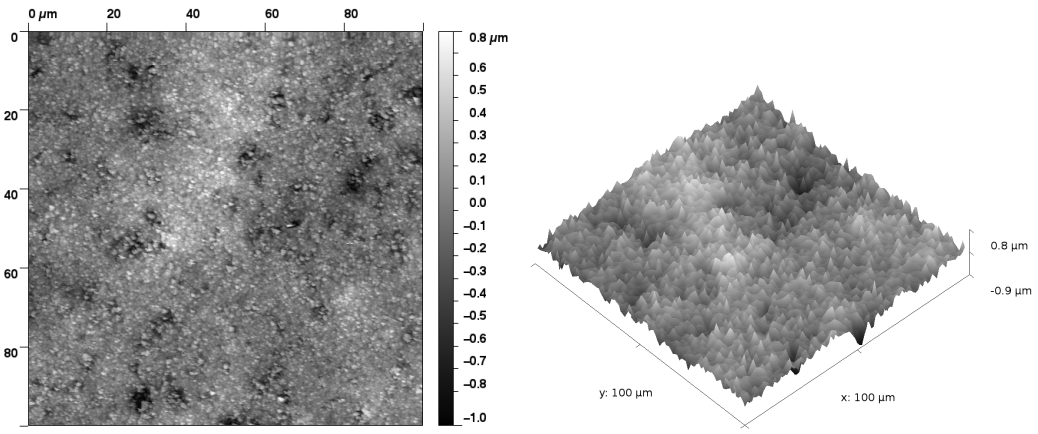

(a) 2D surface profile (b) 3D topographical surface map

Figure A.1: 2D surface profile and 3D topographic map of polycrystalline Cu etched for 15 minutes with a etching solution containing 5 wt% HCl and 5 wt% $CuCl_2$. AFM scans obtained using tapping mode, with a scan speed of 0.5 Hz.

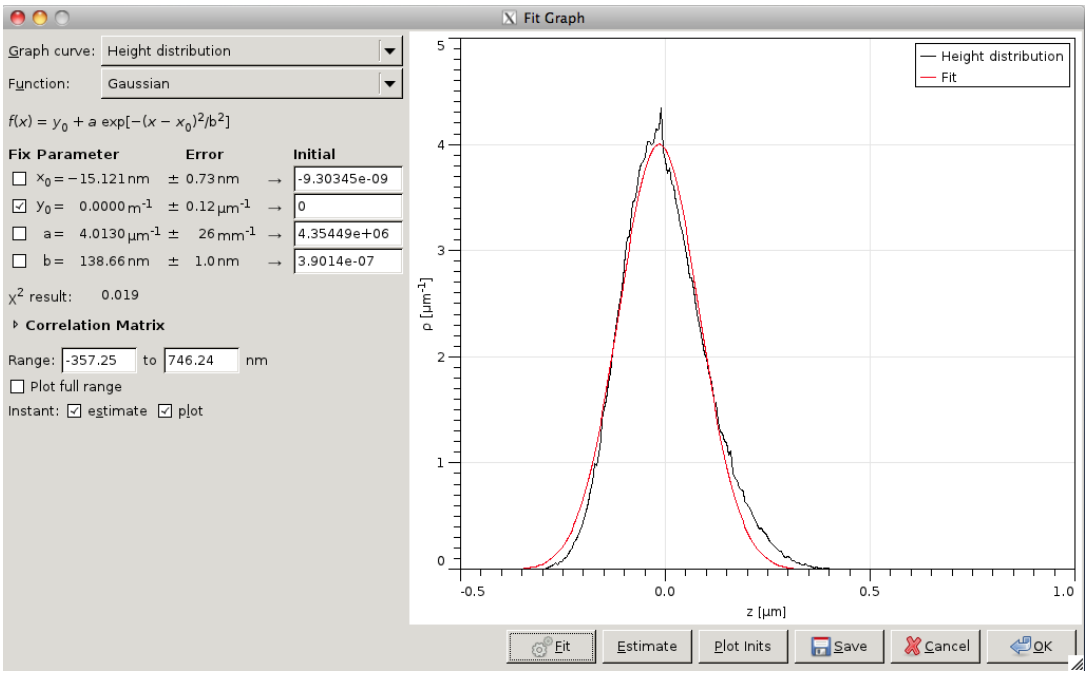

Figure A.2: The height distribution were obtained from the AFM scans in the Gwyddion software. The figure shows the fitting procedure of the Gaussian distribution model, to estimate the standard deviation, shown by the parameter b, of the different samples.

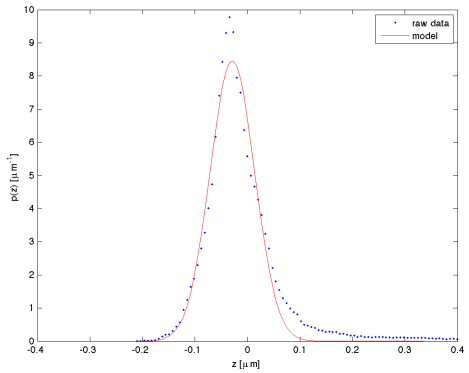

(a) 0 min (Sk = 4.11, K = 25.4)

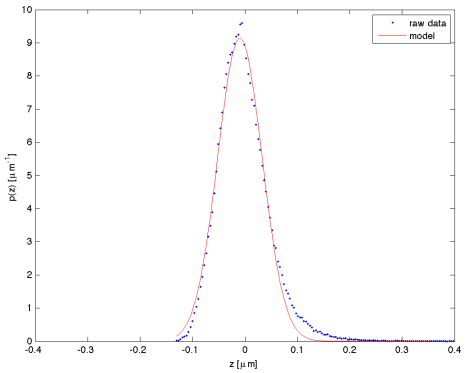

(b) 1 min (Sk = 1.54, K = 9.71)

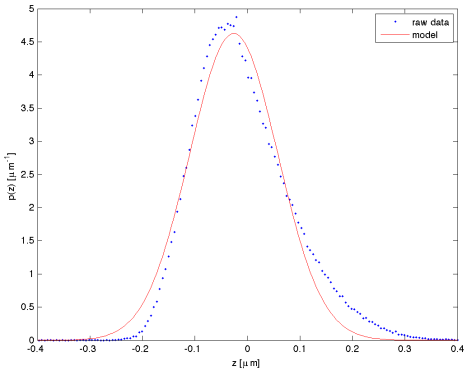

(c) 2 min (Sk = 0.673, K = 0.663)

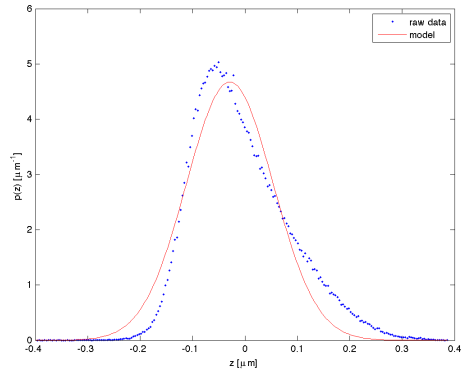

(d) 5 min (Sk = 0.853, K = 1.92)

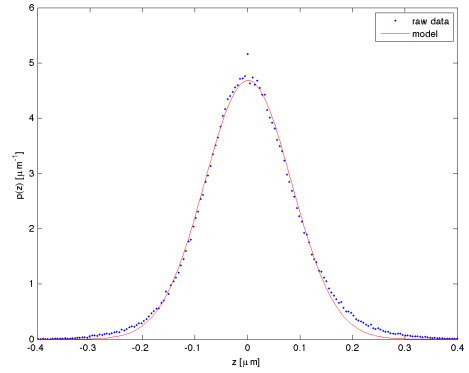

(e) 10 min (Sk = 0.164, K = 0.932)

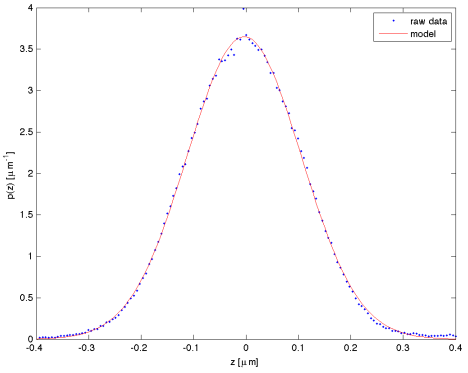

(f) 15 min (Sk = 0.127, K = 1.26)

Figure A.3

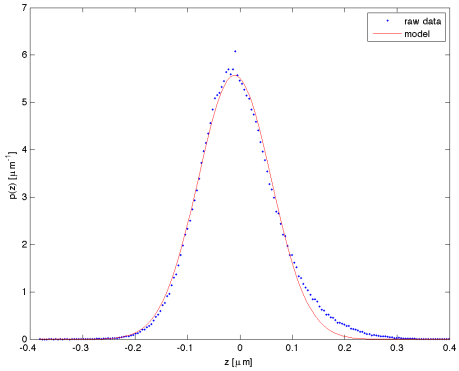

(g) 30 min (Sk = 0.454, K = 0.845)

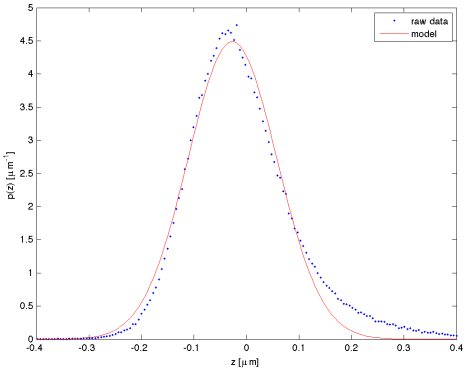

(h) 60 min (Sk = 0.775, K = 2.21)

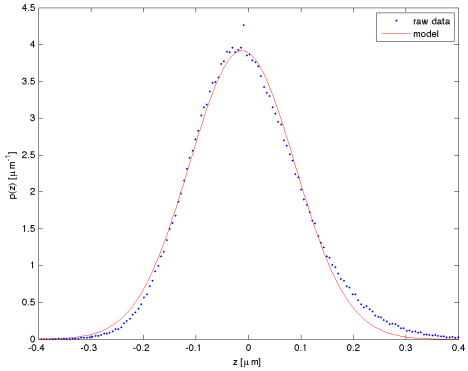

(i) 120 min (Sk = 0.396, K = 0.514)

Figure A.3: Height distribution raw data were fitted to a Gaussian function, and plotted in Matlab.

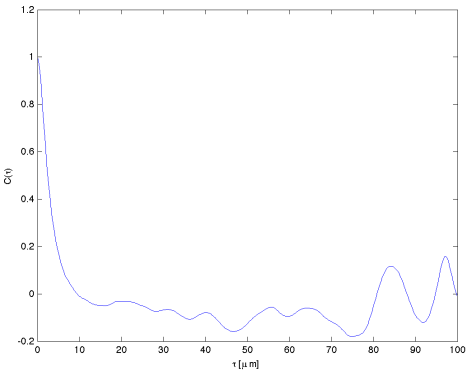

(a) 0 min ($\beta^* = 6.2\ \mu$m)

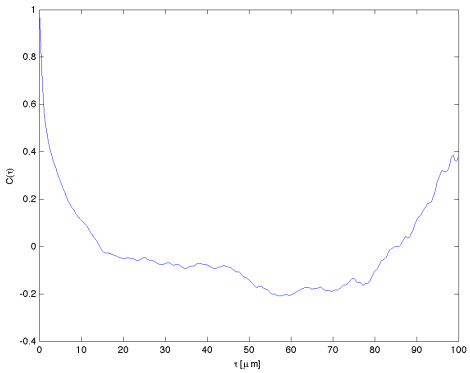

(b) 1 min ($\beta^* = 10.6\ \mu$m)

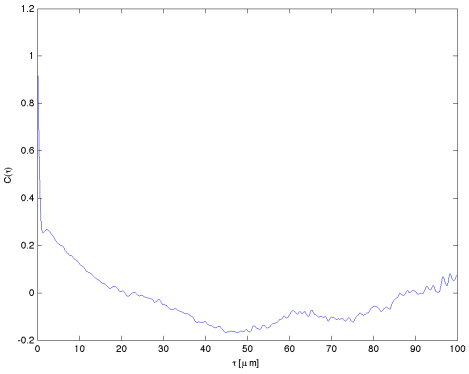

(c) 2 min ($\beta^* = 11.3\ \mu$m)

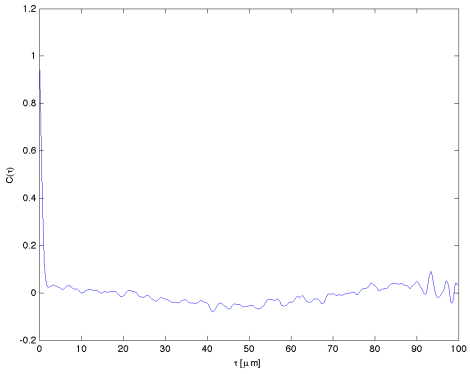

(d) 5 min ($\beta^* = 1.3\ \mu$m)

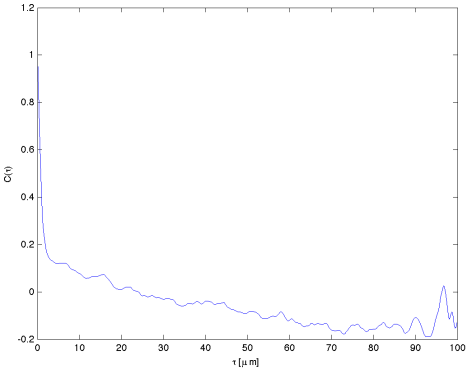

(e) 10 min ($\beta^* = 7.8\ \mu$m)

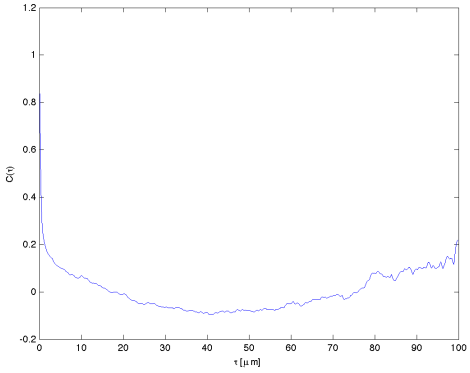

(f) 15 min ($\beta^* = 5.0\ \mu$m)

Figure A.4

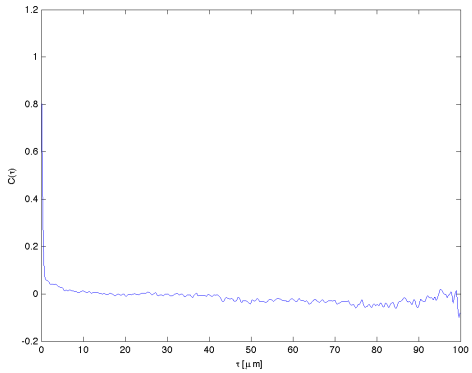

(g) 30 min ($\beta^* = 0.7$ μm)

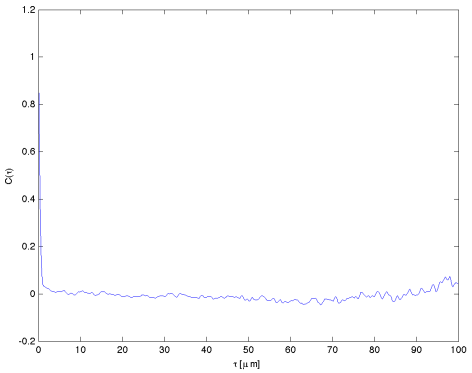

(h) 60 min ($\beta^* = 0.8$ μm)

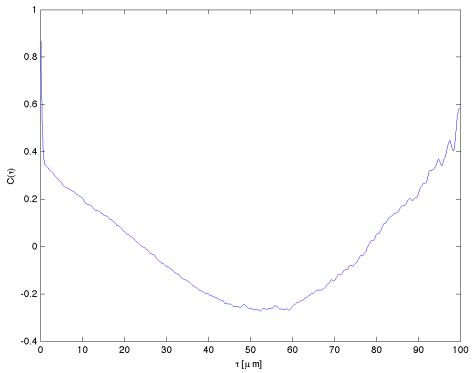

(i) 120 min ($\beta^* = 17.7$ μm)

Figure A.4: Normalized autocorrelation functions from AFM scans of Cu etched with 20 wt% $CuCl_2$ and 20 wt% HCl for different amount of time, prepared with Gwyddion.

A.2 Profilometer scans

Table A.1: Stamp 2: Cu etched for 1 min. Roughness parameters calculated by analysing 500 μm line profile scans by a profilometer in Matlab. All line profiles were corrected for linear surface tilt.

No.	R_a [nm]	R_q [nm]	Sk	K
1	133	175	0.655	3.91
2	178	221	0.221	2.74
3	148	182	0.021	2.55
4	192	229	0.266	2.37
5	207	250	0.157	2.37
6	151	188	0.294	2.75
Average	**168**	**208**	**0.269**	**2.78**
Std. dev.	**29**	**30**	**0.213**	**0.58**

Table A.2: Stamp 3: Cu etched for 5 min. Roughness parameters calculated by analysing 500 μm line profile scans by a profilometer in Matlab. All line profiles were corrected for linear surface tilt.

No.	R_a [nm]	R_q [nm]	Sk	K
1	871	1096	-0.509	3.06
2	616	753	-0.256	2.66
3	821	1031	0.192	2.87
4	770	943	0.320	2.76
5	626	801	-0.031	3.06
6	734	932	-0.274	2.65
7	941	1154	-0.439	2.76
8	890	1065	0.139	2.39
9	799	1020	-0.029	3.27
Average	**785**	**977**	**-0.099**	**2.83**
Std. dev.	**112**	**133**	**0.288**	**0.27**

Table A.3: Stamp 4: Cu etched for 30 min. Roughness parameters calculated by analysing 500 μm line profile scans by a profilometer in Matlab. All line profiles were corrected for linear surface tilt.

No.	R_a [nm]	R_q [nm]	Sk	K
1	1632	2082	0.425	3.03
2	2368	2958	0.465	3.11
3	2095	2585	0.129	2.38
4	2013	2611	0.514	3.16
5	1859	2383	0.463	3.68
6	1553	1887	0.201	2.47
7	2350	3114	1.065	3.86
8	1195	1460	0.277	2.70
Average	**1883**	**2385**	**0.442**	**3.05**
Std. dev.	**407**	**554**	**0.287**	**0.53**

Table A.4: Stamp 5: Cu etched for 10 min. Roughness parameters calculated by analysing 500 μm line profile scans by a profilometer in Matlab. All line profiles were corrected for linear surface tilt.

No.	R_a [nm]	R_q [nm]	Sk	K
1	1038	1315	-0.577	3.04
2	888	1118	-0.120	2.90
3	1125	1396	-0.163	2.67
4	1130	1439	-0.035	3.10
5	922	1142	-0.172	2.88
6	1145	1493	-0.636	3.60
7	1129	1459	-0.382	3.32
8	987	1247	-0.423	2.85
9	1131	1417	0.213	3.41
Average	**1055**	**1336**	**-0.255**	**3.09**
Std. dev.	**100**	**139**	**0.273**	**0.30**

Table A.5: Stamp 6: Cu etched for 20 min. Roughness parameters calculated by analysing 500 μm line profile scans by a profilometer in Matlab. All line profiles were corrected for linear surface tilt.

No.	R_a [nm]	R_q [nm]	Sk	K
1	1310	1802	1.044	5.59
2	1544	2057	1.096	4.16
3	1394	1782	0.004	2.92
4	1469	1994	1.126	4.34
5	1530	1918	0.733	2.95
6	994	1293	0.618	3.48
7	1226	1519	0.521	2.93
8	1827	2260	0.507	2.64
9	1410	1725	-0.324	2.41
Average	**1412**	**1817**	**0.592**	**3.49**
Std. dev.	**231**	**289**	**0.495**	**1.02**

Table A.6: Stamp 15: Cu etched for 30 min with 20 wt% HCl and 20 wt% $CuCl_2$ etching solution. Roughness parameters calculated by analysing 500 μm line profile scans by a profilometer in Matlab. All line profiles were corrected for linear surface tilt.

No.	R_a [nm]	R_q [nm]	Sk	K
1	173	219	0.254	3.30
2	202	255	0.202	3.06
3	181	225	0.106	2.90
4	166	220	0.603	4.40
5	172	220	0.479	3.30
Average	**179**	**228**	**0.329**	**3.39**
Std. dev.	**14**	**15**	**0.206**	**0.59**

Table A.7: Cu_10: Cu etched for 10 min with used copper etchant. Roughness parameters calculated by analysing 500 μm line profile scans by a profilometer in Matlab. All line profiles were corrected for linear surface tilt.

No.	R_a [nm]	R_q [nm]	Sk	K
1	658	825	-0.064	2.91
2	748	948	-0.700	3.08
3	827	1014	-0.326	2.33
4	796	943	-0.170	2.16
5	782	977	-0.193	3.26
6	993	1266	-1.013	4.11
7	975	1186	-0.210	2.41
8	941	1130	0.124	2.47
9	1018	1324	-0.063	3.14
Average	**860**	**1068**	**-0.291**	**2.87**
Std. dev.	**126**	**167**	**0.353**	**0.61**

Table A.8: Cu_11: Cu etched for 60 min with used copper etchant. Roughness parameters calculated by analysing 500 μm line profile scans by a profilometer in Matlab. All line profiles were corrected for linear surface tilt.

No.	R_a [nm]	R_q [nm]	Sk	K
1	2151	2860	0.639	3.87
2	2835	3530	1.170	3.79
3	1426	1878	0.269	3.59
4	1657	2183	0.581	3.73
5	1205	1472	-0.298	2.59
6	2569	3151	0.446	2.87
7	2217	2652	0.375	2.35
8	1563	1883	-0.216	2.35
9	1476	1921	0.170	3.39
Average	**1900**	**2392**	**0.348**	**3.17**
Std. dev.	**564**	**689**	**0.447**	**0.63**

A.3 Contact angle measurements

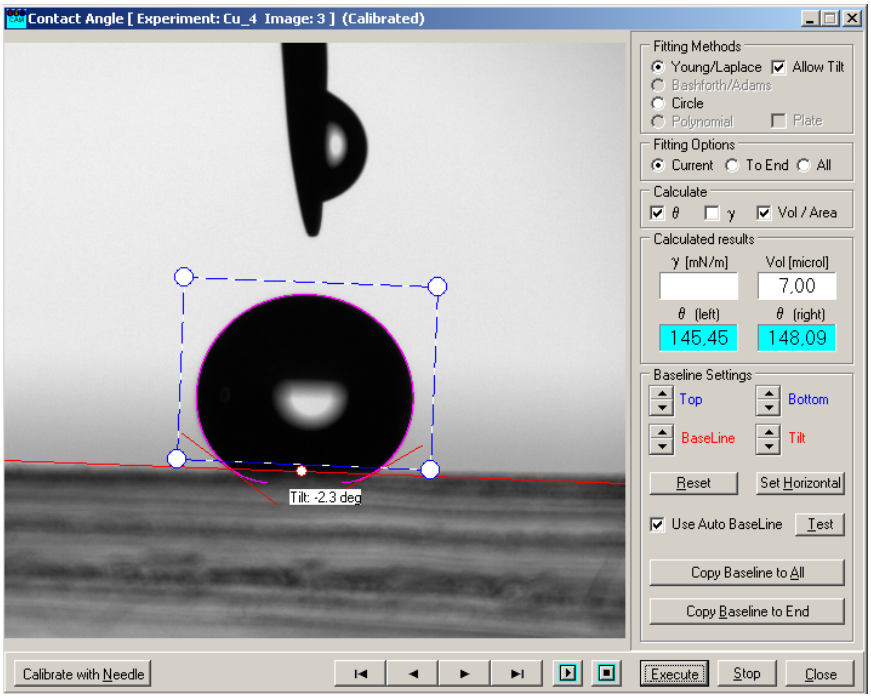

Figure A.5: Curve fitting of the droplet shapes in the computer software CAM2008 by KSV Instruments, gives an estimate of the left and right contact angle and droplet volume. The software also adjusts for surface tilt, as shown in the figure.

Table A.9: Contact angle measurements of flat PDMS.

No.	θ_l [°]	θ_r [°]
1	104.44	104.31
2	101.16	101.79
3	96.32	96.23
4	101.81	100.94
5	105.84	105.10
Average	**101.8**	
Std. dev.	**3.4**	

Table A.10: Contact angle measurements of stamp 14.

No.	θ_l [°]	θ_r [°]
1	134.04	136.74
2	140.73	140.20
3	133.73	134.63
4	133.27	133.22
5	128.90	127.88
Average	**134.3**	
Std. dev.	**4.3**	

Table A.11: Contact angle measurements of Cu_2.

No.	θ_l [°]	θ_r [°]
1	104.96	103.01
2	106.55	101.64
3	105.72	103.46
4	103.18	100.65
5	105.32	103.90
Average	**103.8**	
Std. dev.	**1.8**	

Table A.12: Contact angle measurements of Cu_3.

No.	θ_l [°]	θ_r [°]
1	117.15	118.72
2	116.54	118.32
3	120.57	121.92
4	119.03	116.94
5	107.62	106.69
Average	**116.4**	
Std. dev.	**5.1**	

Table A.13: Contact angle measurements of Cu_4.

No.	θ_l [°]	θ_r [°]
1	118.48	114.43
2	129.51	130.00
3	117.69	116.91
4	125.97	124.29
Average	**122.2**	
Std. dev.	**6.0**	

Table A.14: Contact angle measurements of Cu_16.

No.	θ_l [°]	θ_r [°]
1	165.84	160.00
2	156.10	151.92
3	152.16	154.75
4	149.01	147.96
5	154.64	152.74
Average	**154.7**	
Std. dev.	**5.3**	

Table A.15: Contact angle measurements of Stamp 5.

No.	θ_l [°]	θ_r [°]
1	154.30	151.25
2	153.19	149.60
3	154.67	151.66
4	145.45	148.09
5	154.05	144.07
Average	**150.6**	
Std. dev.	**3.8**	

Table A.16: Contact angle measurements of Stamp 6.

No.	θ_l [°]	θ_r [°]
1	130.71	134.49
2	149.08	142.53
3	137.26	138.69
4	136.85	139.18
5	131.65	134.09
Average	**137.5**	
Std. dev.	**5.4**	

A.4 Replica moulding

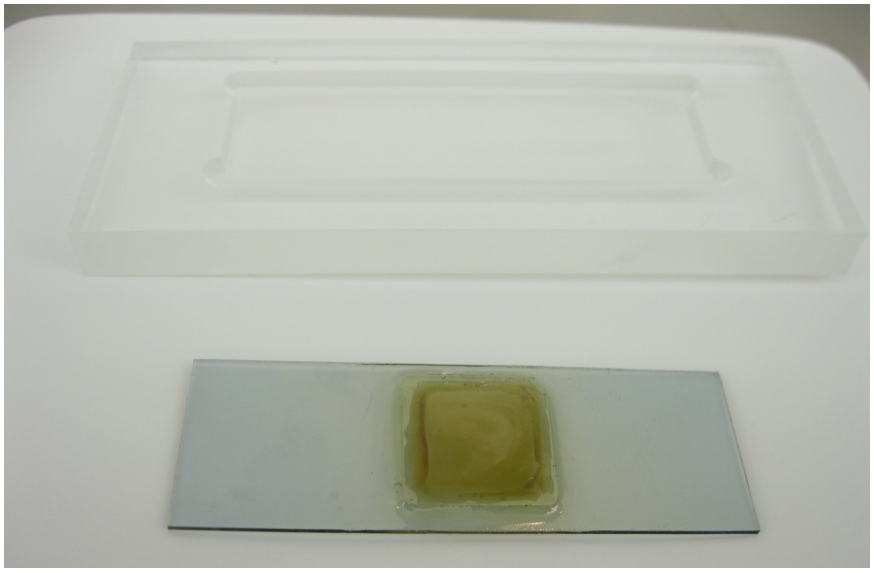

Figure A.6: SU-8 template and the PMMA mould for PDMS replica. After the copper has been removed by etching, the SU-8 is glued onto a glass slide with epoxy. The template is then sputter coated with 5 nm gold and surface functionalized in order to ease the separation of the replicated PDMS piece. The glass slide is fitted in the PMMA mould, PDMS prepolymer is poured over and put to curing in an oven.

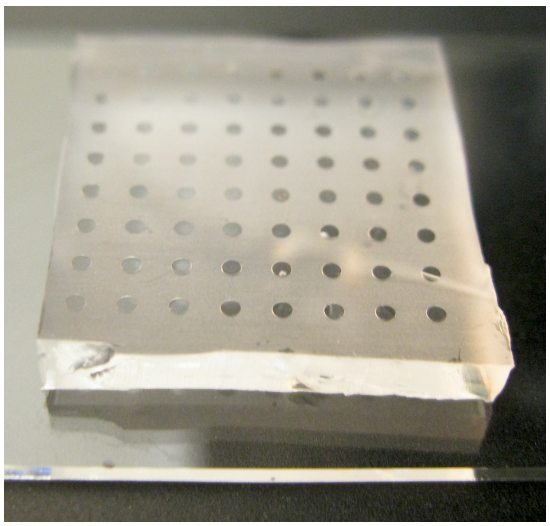

Figure A.7: PDMS replica of sample Cu_10, etched for 10 minutes. The transparent circles are flat PDMS wells about 150 μm deep. The surrounding PDMS appears opaque due to scattering of incident light because of the surface roughness. The PDMS replicas were bonded to a microscopic glass slide through plasma cleaning with oxygen.

A.5 Water capturing

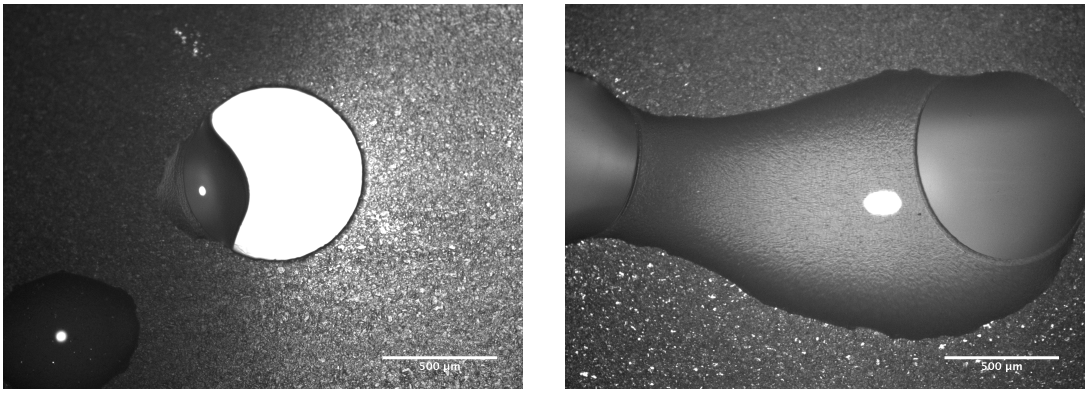

(a) (b)

Figure A.8: Partial water capturing observed by a reflective optical microscope (Sample Cu_10). In a), water wets only a small part of the well in addition to the lower left region of the rough PDMS, while in b) the water bridges across two PDMS wells. The diameter and depth of the wells were measured to be about 782 μm and 150 μm respectively.

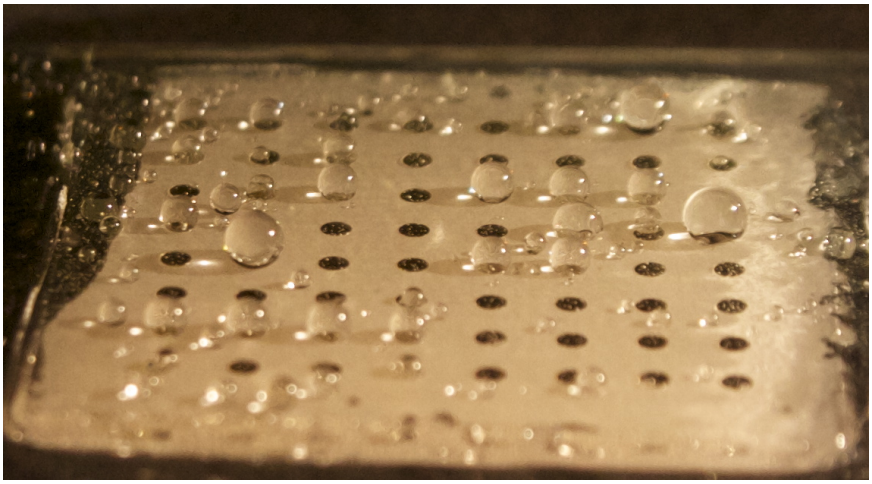

Figure A.9: Photograph showing the capturing of water on the SU-8 replicated after water is sprayed on the surface (sample Cu_10). Most of the droplets are captured on the SU-8 pillars.

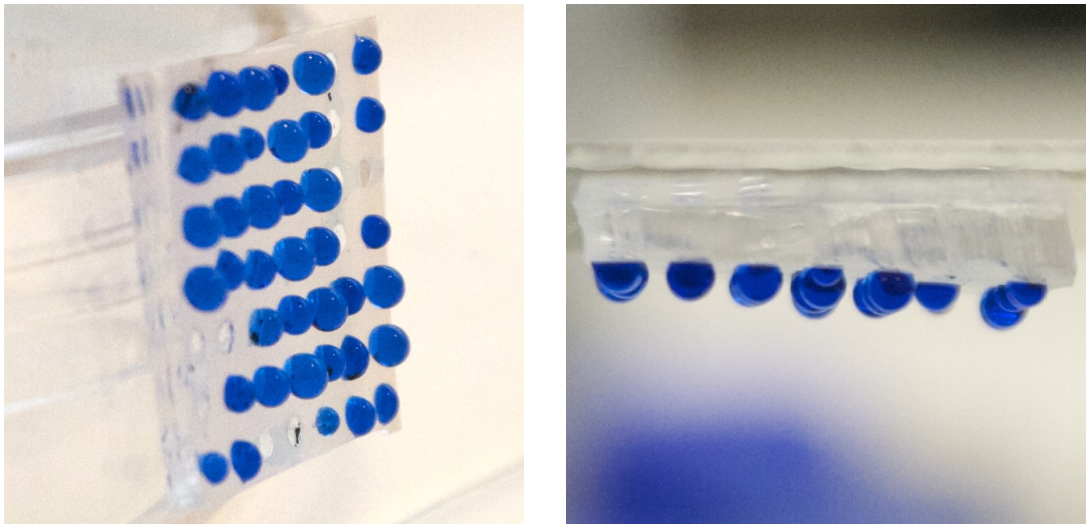

(a) (b)

Figure A.10: Water droplets deposited on PDMS adhere well to the patterned regions (Sample Cu_16). Tilting the sample to an angle close to 90°in a) or turning the sample upside down in b) does not change the droplet distribution on the surface.

Bibliography

[1] Strauss, S. D. (2002) *The big idea: how business innovators get great ideas to market*. Dearborn Trade Publishing.

[2] Buehler, M. J. (2010) Tu(r)ning weakness to strength. *Nano Today*, **5**, 379 – 383.

[3] Buehler, M. J. (2010) Nanomaterials: Strength in numbers. *Nature Nanotechnology*, **5**, 172–174.

[4] Barthlott, W. and Neinhuis, C. (1997) Purity of the sacred lotus, or escape from contamination in biological surfaces. *Planta*, **202**, 1–8.

[5] Neinhuis, C. and Barthlott, W. (1997) Characterization and distribution of water-repellent, self-cleaning plant surfaces. *Annals of Botany*, **79**, 667–677.

[6] Feng, X.-Q., Gao, X., Wu, Z., Jiang, L., and Zheng, Q.-S. (2007) Superior water repellency of water strider legs with hierarchical structures: Experiments and analysis. *Langmuir*, **23**, 4892–4896.

[7] Gao, X. and Jiang, L. (2004) Biophysics: Water-repellent legs of water striders. *Nature*, **432**, 36–36.

[8] Barthlott, W., et al. (2010) The salvinia paradox: Superhydrophobic surfaces with hydrophilic pins for air retention under water. *Advanced Materials*, **22**, 2325–2328.

[9] Cerman, Z., Striffler, B. F., and Barthlott, W. (2009) Dry in the water: The superhydrophobic water fern salvinia - a model for biomimetic surfaces. Gorb, S. N. (ed.), *Functional Surfaces in Biology*, pp. 97–111, Springer Netherlands.

[10] Autumn, K. and Gravish, N. (2008) Gecko adhesion: evolutionary nanotechnology. *Philosophical Transactions of The Royal Society A - Mathematical, Physical & Engineering Sciences*, **366**, 1575–1590.

[11] Parker, A. R. and Lawrence, C. R. (2001) Water capture by a desert beetle. *Nature*, **414**, 33–34.

[12] Woodward, I., Schofield, W., Roucoules, V., Bradley, T., and Badyal, J. (2006) Micropatterning of plasma fluorinated superydrophobic surfaces. *Plasma Chemistry and Plasma Processing*, **26**, 507–516, 10.1007/s11090-006-9032-4.

[13] Kobayashi, T., Shimizu, K., Kaizuma, Y., and Konishi, S. (2011) Novel combination of hydrophilic/hydrophobic surface for large wettability difference and its application to liquid manipulation. *Lab Chip*, **11**, 639–644.

[14] Lam, P., Wynne, K. J., and Wnek, G. E. (2002) Surface-tension-confined microfluidics. *Langmuir*, **18**, 948–951.

[15] Pirrung, M. C. (2002) How to make a dna chip. *Angewandte Chemie-International Edition*, **41**, 1276–1289.

[16] Ito, Y. and Nogawa, M. (2003) Preparation of a protein micro-array using a photo-reactive polymer for a cell-adhesion assay. *Biomaterials*, **24**, 3021–3026.

[17] Roach, P., Shirtcliffe, N. J., and Newton, M. I. (2008) Progress in superhydrophobic surface development. *Soft Matter*, **4**, 224–240.

[18] Zhai, L., Berg, M. C., Cebeci, F. C., Kim, Y., Milwid, J. M., Rubner, M. F., and Cohen, R. E. (2006) Patterned superhydrophobic surfaces: Toward a synthetic mimic of the namib desert beetle. *Nano Letters*, **6**, 1213–1217.

[19] Tadanaga, K., Morinaga, J., Matsuda, A., and Minami, T. (2000) Superhydrophobic-superhydrophilic micropatterning on flowerlike alumina coating film by the sol-gel method. *Chemistry of Materials*, **12**, 590–592.

[20] Kim, H.-C., Kreller, C. R., Tran, K. A., Sisodiya, V., Angelos, S., Wallraff, G., Swanson, S., and Miller, R. D. (2004) Nanoporous thin films with hydrophilicity-contrasted patterns. *Chemistry of Materials*, **16**, 4267–4272.

[21] Khorasani, M. T. and Mirzadeh, H. (2004) In vitro blood compatibility of modified pdms surfaces as superhydrophobic and superhydrophilic materials. *Journal of Applied Polymer Science*, **91**, 2042–2047.

[22] Xia, Y. and Whitesides, G. M. (1998) Soft lithography. *Angewandte Chemie-International Edition*, **37**, 551–575.

[23] Sun, M., Luo, C., Xu, L., Ji, H., Ouyang, Q., Yu, D., and Chen, Y. (2005) Artificial lotus leaf by nanocasting. *Langmuir*, **21**, 8978–8981.

[24] Guo, S., Sun, M., Shi, J., Liu, Y., Huang, W., Combellas, C., and Chen, Y. (2007) Patterning of hydrophilic micro arrays with superhydrophobic surrounding zones. *Microelectronic Engineering*, **84**, 1673 – 1676.

[25] Mumm, F., van Helvoort, A. T. J., and Sikorski, P. (2009) Easy route to superhydrophobic copper-based wire-guided droplet microfluidic systems. *ACS Nano*, **3**, 2647–2652.

[26] Mumm, F. and Sikorski, P. (2011) Oxidative fabrication of patterned, large, non-flaking CuO nanowire arrays. *Nanotechnology*, **22**, 105605.

[27] Mukhopadhyay, R. (2006) Diving into droplets. *Analytical Chemistry*, **78**, 1401–1404.

[28] Hiemenz, P. C. and Rajagopalan, R. (1997) *Principles of colloid and surface chemistry*. Marcel Dekker, 3rd edn.

[29] Whyman, G., Bormashenko, E., and Stein, T. (2008) The rigorous derivation of young, cassie-baxter and wenzel equations and the analysis of the contact angle hysteresis phenomenon. *Chemical Physics Letters*, **450**, 355 – 359.

[30] Wenzel, R. N. (1936) Resistance of solid surfaces to wetting by water. *Industrial & Engineering Chemistry*, **28**, 988–994.

[31] Nosonovsky, M. and Bhushan, B. (2005) Roughness optimization for biomimetic superhydrophobic surfaces. *Microsystem Technologies*, **11**, 535–549.

[32] Cassie, A. B. D. (1948) Contact angles. *Discussions of the Faraday Society*, **3**, 11–16.

[33] Quéré, D., Lafuma, A., and Bico, J. (2003) Slippy and sticky microtextured solids. *Nanote*, **14**, 1109–1112.

[34] Miwa, M., Nakajima, A., Fujishima, A., Hashimoto, K., and Watanabe, T. (2000) Effects of the surface roughness on sliding angles of water droplets on superhydrophobic surfaces. *Langmuir*, **16**, 5754–5760.

[35] Bhushan, B., Nosonovsky, M., and Jung, Y. C. (2007) Towards optimization of patterned superhydrophobic surfaces. *Journal of the Royal Society - Interface*, **4**, 643–648.

[36] Bhushan, B. (2002) *Introduction to Tribology*. Wiley.

[37] Chilamakuri, S. K. and Bhushan, B. (1998) Contact analysis of non-gaussian random surfaces. *Proceedings Institution of Mechanical Engineers*, **212**, 19–32.

[38] Nosonovsky, M. and Bhushan, B. (2008) *Multiscale dissipative mechanisms and hierarchical surfaces: friction, superhydrophobicity, and biomimetics*. Springer.

[39] Nosonovsky, M. and Bhushan, B. (2008) Biologically inspired surfaces: Broadening the scope of roughness. *Advanced Functional Materials*, **18**, 843–855.

[40] Inc., V. I. (2007) *Dektak 150 Profiler User's Manual*.

[41] Brandon, D. and Kaplan, W. D. (2008) *Microstructural Characterization of Materials*. John Wiley & Sons.

[42] de Lange Davies, C. and Stokke, B. T. (2008) *Biophysical Nanotechnologies - Lecture notes TFY 4265 Biophysical Microtechniques*, chap. 10. Biophysics and Medical Technology, Dept. of Physics, NTNU.

[43] Wong, S. S., Harper, J. D., Peter T. Lansbury, J., and Lieber, C. M. (1998) Carbon nanotube tips: High-resolution probes for imaging biological systems. *Journal of American Chemical Society*, **120**, 603–604.

[44] Cakir, O. (2006) Copper etching with cupric chloride and regeneration of waste etchant. *Journal of Materials Processing Technology*, **175**, 63–68.

[45] Cotton, F. A., Murillo, C. A., Bochmann, M., and Grimes, R. N. (1999) *Advanced Inorganic Chemistry*. John Wiley & Sons, Inc., 6th edn.

[46] Barbieri, L., Giovanardi, R., Lancellotti, I., and Michelazzi, M. (2010) A new environmentally friendly process for the recovery of gold from electronic waste. *Environmental Chemistry Letters*, **8**, 171–178.

[47] Jiang, X., Herricks, T., and Xia, Y. (2002) Cuo nanowires can be synthesized by heating copper substrates in air. *Nano Letters*, **2**, 1333–1338.

[48] Hansen, B. J., Lu, G., and Chen, J. (2008) Direct oxidation growth of cuo nanowires from copper-containing substrates. *Journal of Nanomaterials*, **2008**, 7.

[49] Yuan, L., Wang, Y., Mema, R., and Zhou, G. (2011) Driving force and growth mechanism for spontaneous oxide nanowire formation during the thermal oxidation of metals. *Acta Materialia*, **59**, 2491–2500.

[50] Zumdahl, S. S. (2010) *Chemical Principles*. Brooks Cole, 6th edn.

[51] Li, Y., Jia, W.-Z., Song, Y.-Y., and Xia, X.-H. (2007) Superhydrophobicity of 3d porous copper films prepared using the hydrogen bubble dynamic template. *Chemistry of Materials*, **19**, 5758–5764.

[52] Shin, H.-C., Dong, J., and Liu, M. (2003) Nanoporous structures prepared by an electrochemical deposition process. *Advanced Materials*, **15**, 1610–1614.

[53] Quirk, M. and Serda, J. (2001) *Semiconductor manufacturing technology*. Prentice Hall.

[54] Sanders, D. P. (2010) Advances in patterning materials for 193 nm immersion lithography. *Chemical Reviews*, **110**, 321–360.

[55] Kumar, A. and George (1993) Features of gold having micrometer to centimeter dimensions can be formed through a combination of stamping with an elastomeric stamp and an alkanethiol "ink" followed by chemical etching. *Applied Physics Letters*, **63**, 2002–2004.

[56] Xia, Y., Kim, E., Zhao, X.-M., Rogers, J. A., Prentiss, M., and Whitesides, G. M. (1996) Complex optical surfaces formed by replica molding against elastomeric masters. *Science*, **273**, 347–349.

[57] Zhao, X.-M., Xia, Y., and Whitesides, G. M. (1996) Fabrication of three-dimensional micro-structures: Microtransfer molding. *Advanced Materials*, **8**, 837–840.

[58] Kim, E., Xia, Y., and Whitesides, G. M. (1995) Polymer microstructures formed by moulding in capillaries. *Nature*, **376**, 581–584.

[59] Kim, E., Xia, Y., Zhao, X.-M., and Whitesides, G. M. (1997) Solvent-assisted microcontact molding: A convenient method for fabricating three-dimensional structures on surfaces of polymers. *Advanced Materials*, **9**, 651–654.

[60] Åsberg, P. (2007) My little guide to soft lithography. Linköping University.

[61] Govindaraju, A., Chakraborty, A., and Luo, C. (2005) Reinforcement of pdms masters using su-8 truss structures. *Journal of Micromechanics and Microengineering*, **15**, 1303–1309.

[62] Bhattacharya, S., Datta, A., Berg, J. M., and Gangopadhyay, S. (2005) Studies on surface wettability of poly(dimethyl) siloxane (pdms) and glass under oxygen-plasma treatment and correlation with bond strength. *Journal of Microelectromechanical Systems*, **14**, 590–597.

[63] Patois, T., Taouil, A. E., Lallemand, F., Carpentier, L., Roizard, X., Hihn, J.-Y., Bondeau-Patissier, V., and Mekhalif, Z. (2010) Microtribological and corrosion behaviors of 1H,1H,2H,2H-perfluorodecanethiol self-assembled films on copper surfaces. *Surface and Coatings Technology*, **205**, 2511–2517.

[64] Mansfield, M. and O'Sullivan, C. (1998) *Understanding Physics*, chap. 16, p. 501. John Wiley & Sons.

[65] Goldstein, G. I., Newbury, D. E., Echlin, P., Joy, D. C., Fiori, C., and Lifshin, E. (1981) *Scanning electron microscopy and x-ray microanalysis*. Plenum Press.

[66] MicroChem Corp. (2011), SU-8 Resists, SU-8 2000 & SU-8 3000 Resists. `http://www.microchem.com/products/su_eight.htm`, (Accessed on 8 May, 2011).

[67] Lee, K. Y., LaBianca, N., Rishton, S. A., Zolgharnain, S., Gelorme, J. D., Shaw, J., and Chang, T. H.-P. (1995) Micromachining applications of a high resolution ultrathick photoresist. *Journal of Vacuum Science & Technology B*, **13**, 3012–3016.

[68] Nanosensors ™ (2011), PPP-NCH. `http://www.nanosensors.com/PPP-NCH`, (Accessed on 8 May, 2011).

[69] Gwyddion (2011), Free SPM (AFM, SNOM/NSOM, STM, MFM) data analysis software. `http://gwyddion.net/`, (Accessed on 8 May, 2011).

[70] William D. Callister, J. (2007) *Materials Science and Engineering - An Introduction*. John Wiley & Sons.

[71] Poon, C. Y. and Bhushan, B. (1995) Comparison of surface roughness measurements by stylus profiler, afm and non-contact optical profiler. *Wear*, **190**, 76–88.

[72] Wang, R.-C. and Li, C.-H. (2009) Improved morphologies and enhanced field emissions of cuo nanoneedle arrays by heating zno coated copper foils. *Crystal Growth & Design*, **9**, 2229–2234.

[73] Zhang, K., Rossi, C., Tenailleau, C., Alphonse, P., and Chane-Ching, J.-Y. (2007) Synthesis of large-area and aligned copper oxide nanowires from copper thin film on silicon substrate. *Nanotechnology*, **18**, 275607.

[74] Abe, S., Burrows, B., and Ettel, V. A. (1980) Anode passivation in copper refining. *Canadian Metallurgical Quarterly*, **19**, 289–296.

[75] Jin, S., Ghali, E., and Adnot, A. (1991), Aes study on the passivation mechanism of copper anodes electrolyzed in H_2SO_4-$CuSO_4$ solution. Report AES, laval University.

[76] Jarjoura, G. and Kipouros, G. J. (2006) Electrochemical studies on the effect of nickel on copper anode passivation in a copper sulphate solution. *Canadian Metallurgical Quarterly*, **45**, 283–294.

[77] Shaw, M., Nawrocki, D., Hurditch, R., and Johnson, D. (2003) Improving the process capability of su-8. *Microsys*, **10**, 1–6.

[78] Ceyssens, F. and Puers, R. (2006) Creating multi-layered structures with freestanding parts in su-8. *Journal of Micromechanics and Microengineering*, **16**, S19–S23.

[79] Dai, W., Lian, K., and Wang, W. (2005) A quantitative study on the adhesion property of cured su-8 on various metallic surfaces. *Microsystem Technologies*, **11**, 526–534.

[80] Williams, J. D. and Wang, W. (2004) Using megasonic development of su-8 to yield ultra-high aspect ratio microstructures with uv lithography. *Microsystem Technologies*, **10**, 694–698.

[81] Lin, C.-H., Lee, G.-B., Chang, B.-W., and Chang, G.-L. (2002) A new fabrication process for ultra-thick microfluidic microstructures utilizing su-8 photoresist. *Journal of Micromechanics and Microengineering*, **12**, 590.

[82] Bhushan, B. (2003) Adhesion and stiction: Mechanisms, measurement techniques, and methods for reduction. *Journal of Vacuum Science & Technology B*, **21**, 2262.

[83] Hui, C. Y., Jagota, A., Lin, Y. Y., and Kramer, E. J. (2002) Constraints on microcontact printing imposed by stamp deformation. *Langmuir*, **18**, 1394–1407.

[84] Roca-Cusachs, P., Rico, F., Martinéz, E., Toset, J., Farré, R., and Navajas, D. (2005) Stability of microfabricated high aspect ratio structures in poly(dimethylsiloxane). *Langmuir*, **21**, 5542–5548.

[85] Bhushan, B. and Jung, Y. C. (2006) Micro- and nanoscale characterization of hydrophobic and hydrophilic leaf surfaces. *Nanotechnology*, **17**, 2758–2772.

[86] He, B., Patankar, N. A., and Jungh (2003) Multiple equilibrium droplet shapes and design criterion for rough hydrophobic surfaces. *Langmuir*, **19**, 4999–5003.

[87] Cortese, B., D'Amone, S., Manca, M., Viola, I., Cingolani, R., and Gigli, G. (2008) Superhydrophobicity due to the hierarchical scale roughness of pdms surfaces. *Langmuir*, **24**, 2712–2718.

[88] Tserepi, A. D., Vlachopoulou, M.-E., and Gogolides, E. (2006) Nanotexturing of poly(dimethylsiloxane) in plasmas for creating robust superhydrophobic surfaces. *Nanotechnology*, **17**, 3977.

[89] de Givenchy, E. P. T., Amigoni, S., Martin, C., Andrada, G., Caillier, L., Géribaldi, S., and Guittard, F. (2009) Fabrication of superhydrophobic pdms surfaces by combining acidic treatment and perfluorinated monolayers. *Langmuir*, **25**, 6448–6453.

[90] Eddington, D. T., Puccinelli, J. P., and Beebe, D. J. (2006) Thermal aging and reduced hydrophobic recovery of polydimethylsiloxane. *Sensors and Actuators B: Chemical*, **114**, 170 – 172.

[91] Bormashenko, E., Pogreb, R., Whyman, G., and Erlich, M. (2007) Cassie-wenzel wetting transition in vibrating drops deposited on rough surfaces: Is the dynamic cassie-wenzel wetting transition a 2d or 1d affair? *Langmuir*, **23**, 6501–6503.

[92] He, B., Lee, J., and Patankar, N. A. (2004) Contact angle hysteresis on rough hydrophobic surfaces. *Colloids and Surfaces A: Physicochemical and Engineering Aspects*, **248**, 101–104.

[93] Hu, S., Ren, X., Bachman, M., Sims, C. E., Li, G. P., and Allbritton, N. (2002) Surface modification of poly(dimethylsiloxane) microfluidic devices by ultraviolet polymer grafting. *Analytical Chemistry*, **74**, 4117–4123.